Studies of Foam Drainage and Stability

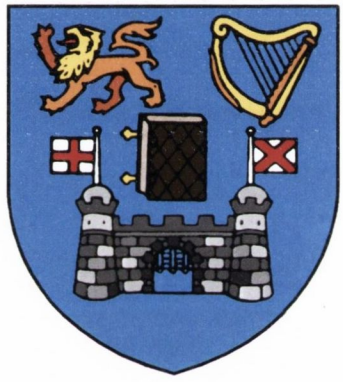

Steven T. Tobin

School of Physics

Trinity College Dublin

A thesis submitted for the degree of

Doctor of Philosophy

November, 2013

Declaration

I declare that this thesis has not been submitted as an exercise for a degree at this or any other university. Except where otherwise stated, the work described herein has been carried out by the author alone.

I agree to deposit this thesis in the University's open access institutional repository or allow the library to do so on my behalf, subject to Irish Copyright Legislation and Trinity College Library conditions of use and acknowledgement.

Steven Tobin 

Acknowledgements

I've heard that the Acknowledgements section of a thesis is the only part most people read. The added pressure of that statement has been incredibly helpful as deadlines loom ominously, suddenly close after years of being far over the horizon. While completing a PhD sometimes feels like a lonely path, it is never one you walk alone. Throughout the years — through the good times and bad — I have always been fortunate to have friends and family willing to listen, advise, and support. So, without further ado, the very necessary act of acknowledgements.

I consider myself supremely lucky to have had Stefan Hutzler as my PhD supervisor. Always helpful and ready to give advice and support, while being trusting of my progress and never micro-managing my research, I cannot give him enough credit in my journey from a slightly lost undergraduate to a researcher.

I must also thank Denis Weaire for always reminding me of what a researcher should aim to be and pushing me towards that ideal, and Matthias Möbius for advice throughout the sometimes-arduous process of completing my PhD. I have always been amazed at how willing researchers are to take time from their busy work to advise and assist. The interactions, advice, and discussions I have been fortunate enough to have with people from all over the world made a big impact on me.

I have also been lucky in my co-workers (and in how many of them I can call friends) and compatriots in postgraduate research. Every one of them has helped me in some way, and even the smallest things mean a great deal in difficult moments. So — to Aaron, Mike, Cathal, Barry, Tom, Other Steve, Joe, Ruggero, Ho-Kei, Rob, David, Gav — thank you all for everything you did, knowingly or not.

Thanks to my sister who used her amazing copy-editor skills to help me put commas in the right places and spell 'tetrakaidecahedron' correctly, and showed me the proper use of '—'. Thanks to my Mom and Dad, who always supported me on this crazy journey.

Megan — I could fill this entire thesis thanking you for everything you have done for me. You have been by my side at every step of this crazy journey. I could not ask for a better friend, wife, partner or confidant. I love you — let's go have adventures.

The present work could not have been completed without the financial support of the Science Foundation Ireland (08/RFP/MTR1083), the European Space Agency (MAP AO-99-108:C14914/02/NL/SH and AO-99-075:C14308/00/NL/SH), the Irish Research Council for Science, Engineering & Technology (IRCSET), the SFI SURE Summer Undergraduate Research Experience programme, and COST Actions P21 (Physics of Droplets) and MP1106 (Smart and Green Interfaces).

Many of the numerical calculations in this thesis were performed on the Lonsdale cluster maintained by the Trinity Centre for High Performance Computing. This cluster was funded through grants from Science Foundation Ireland.

Summary

While the static nature of foams has been well studied, the dynamic nature of a foam — how it evolves and responds to external forces and changing environments — is less well understood. We will present results from the analysis of two such aspects of foam physics: the drainage of liquid through the foam, and the stability of foam.

Drainage, or the flow of the liquid phase through the network of channels and films that constitutes the foam, is usually one of the most influential processes affecting a foam. Foam drainage can be modelled using the Foam Drainage Equation (FDE), which describes the variation of the liquid content of the foam as a function of space and time.

We will present a complete treatment — analytical, numerical, and experimental — of the process of foam fractionation, which uses a flowing foam to separate solutions based on surface activities. It has widespread use in industries such as mining and biochemistry (for examples, recovering more material from tailings and extracting proteins, respectively). Our analysis was carried out on a model system — an inverted U-tube — and is based on modifications to the elementary FDE. We successfully predicted the flow behaviour of our model fractionation set-up, and showed that our model can be generalised to other fractionation set-ups.

We will also present analysis of the efficiency of such set-ups, based on the necessarily finite size of column components in experimental and industrial settings. The model represents both a useful tool for analysing and studying the physics of fractionation, and a platform to build more extensive analyses upon.

We also carried out the first *in-situ* analysis of the chemical and physical parameters of liquid metal foams, again using a modified form of the FDE. While previous methods required the solidification and destruction of the molten foam samples, our method used X-ray radioscopy (to measure the time- and space-dependent liquid content of the foam), coupled with fits of numerical solutions of the FDE. We will present, for the first time, direct measurements of the surface tension and viscosity of the liquid metal in these advanced foams. We will also comment on the effects of particle additions in these foams, and how the viscosity may be dramatically influenced by their presence.

The stability of foams is also of great interest in many processes, whether one wishes to maintain foams or destroy them. We carried out the first large-scale study of the stability and lifetime of individual soap films, finding the lifetimes well described by the Weibull distribution. Environmental exposure was found to be of large importance to the longevity of the soap films, with drastic reductions in lifespan found in a secondary laboratory experiment. This result has contact with research on environmental effects in fractionation experiments.

List of publications

1. **S.T. Tobin**, J.D. Barry, A.J. Meagher, B. Bulfin, C.E. O'Rathaille, S. Hutzler. Ordered polyhedral foams in tubes with circular, triangular and square cross-section. *Colloids and Surfaces A*, 382(1–3):24–31, 2011.

2. S.J. Hardiman, **S.T. Tobin**, P.J. Richmond. Distributions of certain market observables in an online betting exchange. *Journal of Dynamics of Socio-Economic Systems*, 2(1):127–137, 2011.

3. **S.T. Tobin**, A.J. Meagher, B. Bulfin, M. Möbius, S. Hutzler. A public study of the lifetime distribution of soap films. *American Journal of Physics*, 79(8):819, 2011.

4. D. Weaire, **S.T. Tobin**, A.J. Meagher, S. Hutzler. Chap. 2: Foam Morphology (pages 7–26) in *Foam Engineering: Fundamentals and Applications (Paul Stevenson Ed.)*, Wiley-Blackwell 2012.

5. S. Hutzler, **S.T. Tobin**, A.J. Meagher, A. Marguerite, D. Weaire. A model system for foam fractionation. *Proceedings of the Royal Society A*, 469(2154):2012072 2013.

6. **S.T. Tobin**, D. Weaire, and S. Hutzler. Theoretical analysis of the performance of a foam fractionation column. *Submitted for publication*, 2013.

Publications in preparation

1. F. Garcia-Moreno, **S.T. Tobin**, M. Mukherjee, C. Jiménez, G.S. Vinod Kumar, E. Solórzano, S. Hutzler and J. Banhart. Determination of surface tension and viscosity in liquid aluminium alloy foams. *In preparation*, 2013.

2. R.P. Murtagh, **S.T. Tobin**, D. Weaire, and S. Hutzler. The Z-Cone Model for the Energy of a Foam. *In preparation*, 2013.

List of presentations

1. S. Hutzler, J.D. Barry, **S.T. Tobin**, B. Bulfin, D. Weaire. Ordered dry foams in tubes with circular, triangular and square cross-section. *EUFoam 2010, Poster* (presenting author)

2. **S.T. Tobin**, A. Meagher, B. Bulfin, M.E. Möbius, D. Weaire, S. Hutzler. An interactive study of the lifetime distribution of soap films. *EUFoam 2010, Poster* (first and presenting author)

3. S. Hutzler, D. Weaire, **S.T. Tobin**, A.J. Meagher, V. Poulichet, A. Marguerite. A model system for foam fractionation: the analysis of an overflowing foam. *EUFoam 2012, presentation* (contributing author)

4. **S.T. Tobin**, S. Hutzler, A.J. Meagher, A. Marguerite, D. Weaire. A model system for foam fractionation. *COST MP1106 2013, presentation* (first and presenting author)

Contents

List of Tables xix

List of Figures xxi

1 Introduction to foams 1

1.1 What is a foam? 1

1.2 Processes that shape foams 2

1.3 Classifying foams by liquid fraction: wet to dry 5

1.3.1 The dry limit 7

1.3.2 The wet limit 11

1.3.3 Between the two limits 13

1.4 Foam structure for finite values of liquid fraction 14

1.5 Summary 20

I Foam Drainage 23

2 Introduction to foam drainage theory 25

2.1 Modelling foam drainage 26

2.2 The Foam Drainage Equation 28

2.3 Example solutions of the FDE 30
2.3.1 A foam in equilibrium 31
2.3.2 Forced drainage — solitary wave solution 32
2.3.3 Linear approximation to the FDE 34
2.4 Example of analysis using the FDE — a linear case 34

3 Foam Fractionation **41**
3.1 Introduction to foam fractionation 41
3.2 A model system for foam fractionation 43
3.2.1 Basis of the theory 46
3.2.2 Analysis of the limiting case: $L \to \infty$ 49
3.2.3 Generalisation of the infinite leg power law 54
3.2.4 Numerical illustration 57
3.2.5 Experiments 63
3.3 Performance metrics for the U-tube fractionation column 67
3.3.1 Limiting behaviour of liquid fraction in the right leg 69
3.3.2 Finite size effects of the left leg 71
3.3.3 Results for performance metrics 76
3.4 Alternate fractionation columns 78
3.4.1 Fractionation column components — the skimmer 78
3.4.2 Analysing fractionation modes using forced drainage 83
3.5 Conclusions and Outlook 86

4 Drainage of liquid metal foams **89**
4.1 Introduction to metal foams 89
4.2 Experiments on metal foams 91

4.2.1 Experimental apparatus and procedures 91
4.2.2 Liquid fraction analysis 92
4.3 Determining melt parameters from numerical solutions 97
4.3.1 Numerical analysis of radioscopic images 97
4.3.2 Results from numerical solutions 103
4.3.3 Discussion of numerical results 106
4.4 Conclusions and Outlook 109

II Foam Stability **111**

5 Statistical analysis of soap film lifetimes **113**
5.1 Introduction to foam stability 113
5.2 Experimental set-up 115
5.3 Data analysis and results 120
5.4 Effects of exposure to atmosphere 126
5.5 Possible mechanisms of rupture 128
5.6 Conclusions and outlook 130

6 Coda **133**

III Appendices **141**

A Full derivation of the Foam Drainage Equation **143**

B Analytic solutions for U-tube with infinite leg lengths **151**

C Finite size effects in the U-tube model **155**

C.1 The effect of finite bend radius 155

C.2 The effect of finite leg length 156

C.3 Generality of the limiting case 162

D Overview of software used **165**

D.1 The Surface Evolver 165

D.2 Modelling wet foams using the Surface Evolver 167

D.3 The MIGRAD minimiser 170

E Statistical analysis of lifetime data **173**

E.1 Maximum likelihood estimation 174

E.2 Two-sample Kolmogorov-Smirnov test 175

E.3 The Weibull distribution 177

References **179**

List of Tables

4.1 Results for surface tension and viscosity for AlSi6Cu4, AlSi11, and AlSi9 + 5, 10 and 20 vol.% SiC foams obtained from fitting numerical solutions of the foam drainage equation to experimental liquid density profiles. Bulk values for aluminium and aluminium alloys from literature are listed for comparison. PM indicates an alloy formed using the 'powder-melt' technique. 105

4.2 Experimentally determined values for the particle factor P (the increase in viscosity of bulk alloy by the addition of particles) allow us to calculate S (the contribution of the altered foam structure) from our numerically-calculated values generated from the fits to experimental data. 107

List of Figures

1.1 Examples of foams from both day-to-day and more esoteric contexts. 3
1.2 A comparison between wet and dry 3D foams, showing simulation and experimental images. 6
1.3 Some example polyhedral cells as found by Matzke in a disordered foam. 7
1.4 Plateau's rules of equilibrium shown by graphical example. 9
1.5 A Plateau border in schematic form, showing the cross-sectional shape of the border. 9
1.6 A photograph of the surface of a foam, with the complex curvature of the surface made visible by reflections. 10
1.7 A tomographic reconstruction of a 3D monodisperse foam (courtesy of A. Meagher). 12
1.8 The design of the Beijing Olympics Water Cube is based on the Weaire-Phelan foam. 15
1.9 Experimental and simulated images of the Kelvin and Weaire-Phelan foams. 17

1.10 Increasing the liquid fraction significantly affects the structure of a foam. 18
1.11 Calculations of the energy per bubble as liquid fraction is changed for Kelvin and Weaire-Phelan foams. 19
1.12 Increasing liquid fraction past some point will lead to increases in the surface energy per bubble, coinciding with stability loss. 20

2.1 The flow of liquid through the network of Plateau borders. 27
2.2 A plot of a numerical solution of the full foam drainage equation, including space and time dependence. 31
2.3 Analytical solutions of the FDE for a dry foam undergoing forced drainage. 33
2.4 Regions where the linear approximation to the FDE is valid can be found by visual inspection. 35
2.5 Experimental data from free drainage of aqueous foams 37
2.6 An example of a fit to the slopes of linear FDE profiles 38
2.7 We see excellent agreement between our recreation and the original data. 39
2.8 Zooming out slightly shows the full recreation, including x_a 40

3.1 A schematic illustration of the inverted U-tube set-up used as the model for our study of foam fractionation. 44
3.2 As $\epsilon \to 0$, the length of the left leg of the U-tube $L_l \to \infty$. The predicted asymptotic behaviour is clear. 53
3.3 The slope of the dependence of liquid velocity v on the gas velocity V is given by $k(n)$. 56

3.4 A numerical calculation of a liquid profile for a U-tube system with a similar geometry to the tubes used in our experiments. 60
3.5 The analytic prediction for the relationship between liquid flux and gas velocity shows excellent agreement with values calculated from numerical solutions. 61
3.6 Our simulations match the predicted linear dependence of liquid velocity v on gas velocity V predicted by Equation 3.16. 62
3.7 Experimentally determined variation of liquid flux J as a function of gas velocity V. 66
3.8 Experimentally determined variation of liquid velocity v as a function of gas velocity V. 67
3.9 A comparison between a numerical solution of the right-leg liquid fraction and the exponential decay model. 72
3.10 Liquid flux J increases as the left-leg length L_l is decreased (as predicted by theory), thus decreasing the efficiency of the fractionation process. 74
3.11 As $\epsilon \to 0$, the length of the left leg $L_l \to \infty$. 75
3.12 Our metric of efficiency is inversely proportional to gas velocity V and proportional to leg length L_l. 76
3.13 Fixing V lets us see the dramatic effect varying L_l can have on performance. 77
3.14 A schematic diagram showing the skimmer variant column. 79
3.15 A numerical solution for a fractionation column including a skimmer. 81
3.16 Analytic and numerical results for the skimmer system show good agreement over a wide range of leg lengths. 83

3.17 A schematic diagram showing the extra flux terms required to model other fractionation modes. 84
3.18 The effects of forced drainage on liquid fraction can be clearly seen by comparison to columns without the extra terms. 86

4.1 The X-ray radioscopy set-up used during the parabolic flights. . . . 93
4.2 The progression of a typical parabolic flight, showing gravity, temperature and sample evolution. 95
4.3 X-ray radioscopic images of an AlSi6Cu4 liquid metal foam (with 0.6 wt.% TiH_2 blowing agent). 96
4.4 Observed drainage in AlSi9 foams varies dramatically with concentration of SiC particles, shown in these comparison images. 97
4.5 Experimentally obtained 3D liquid fraction profiles of an AlSi6Cu4 foam recorded over a parabolic flight. 98
4.6 Conducting fits over subsets of the same drainage data allows us to minimise the effect of noise or bursting bubbles. 100
4.7 An example of a final fit for an AlSi9 + 5 vol.% SiC liquid metal foam. 102
4.8 A plot of the residuals between experimental data and fitted simulations shown in Figure 4.7. 103
4.9 A schematic of a typical foam film, showing some structural effects that contribute to S. 108

5.1 A schematic representation of apparatus used for the creation of parallel and equally-spaced soap films in a tube. 117
5.2 A close-up of a single sample, created by a member of the public. . 118

5.3 A snapshot of the public display of tubes containing soap films in the Science Gallery. 119

5.4 Distribution of initial film counts (normalised) with a fitted normal distribution. 121

5.5 We observed very few large bursting events (over 1000 single-film events compared to two 11-film events). 122

5.6 The distribution of lifetimes of individual films is given by a fitted Weibull probability distribution. 123

5.7 By integrating the data we can see more clearly how well it is described by the Weibull distribution. 124

5.8 The average film lifetime appears to be independent of the initial number of films in the sample. 126

5.9 A comparison of both corked and uncorked tubes shows a dramatic decrease in lifetime from atmospheric exposure. 128

5.10 An illustration of thermally-excited capillary wave rupture of a thin film. 130

A.1 A Plateau border in schematic form, showing the cross-sectional shape of the border. 145

B.1 Examples of numerical solutions for the liquid fraction of the left and right legs of the U-tube model system. 153

C.1 The contour used to integrate Equation C.11. 159

D.1 Increasing the tessellation in the Surface Evolver increases the accuracy of the simulations. 166

D.2 Careful observation of a Weaire-Phelan foam allows us to observe the impending contact loss. 168

Chapter 1

Introduction to foams

1.1 What is a foam?

From getting in the shower first thing in the morning to drinking a cold beer at the end of a long working day, foams are commonplace in almost every aspect of our lives. And yet we hardly ever give them any serious thought, overlooking a rich and deep research area which links many fields, from pure mathematics and crystal formation through chemical engineering and materials engineering (touching almost everything in between). Foams can be used as a model for other complex systems [1], and have even been proposed as a model for the fundamental structure of spacetime [2].

Foams have therefore found many important uses in industry and materials research. As the scope of foam applications grows, the need to create strong interdisciplinary links between novel research and the existing body of foams research becomes ever greater. In this work, we will present results from research under-

taken to forge such links between theoretical models of draining foams and real-world uses of foams — an industrial process of foam fractionation and experiments aiming to create foams from liquid metal.

So, then, what is a foam? Foams are dynamic collections of bubbles, arranged in fascinating structures that change and evolve steadily in time. The most commonly encountered foams are disordered, as bubbles of many sizes (polydisperse) are mixed together. However, through careful preparation, they can be made to form into complex and elegant ordered structures [3]. They are multi-phase systems, with a gaseous phase dispersed through a liquid phase. The most commonly encountered foams have air as the gaseous phase, with the liquid phase consisting of water mixed with a surfactant such as soap (think of washing the dishes).

While, at first glance, foams often appear quite static, there is a constant and complex dance of several interacting and competing processes. We will examine our foams in terms of this dynamic nature, specifically focusing on the movement of liquid through the foam. We shall do this by building on foam drainage theory, linking it intimately with experimental observations and computer modelling. We will also briefly look at the stability and lifetimes of bubbles, as the deterioration of foams has significant effects in many industrial and experimental systems.

1.2 Processes that shape foams

As we have mentioned, foams are complicated and dynamic systems shaped by various processes. Each could be the subject of a lifetime's work and, thus, it becomes important to understand where and when we may focus our attention on a single process.

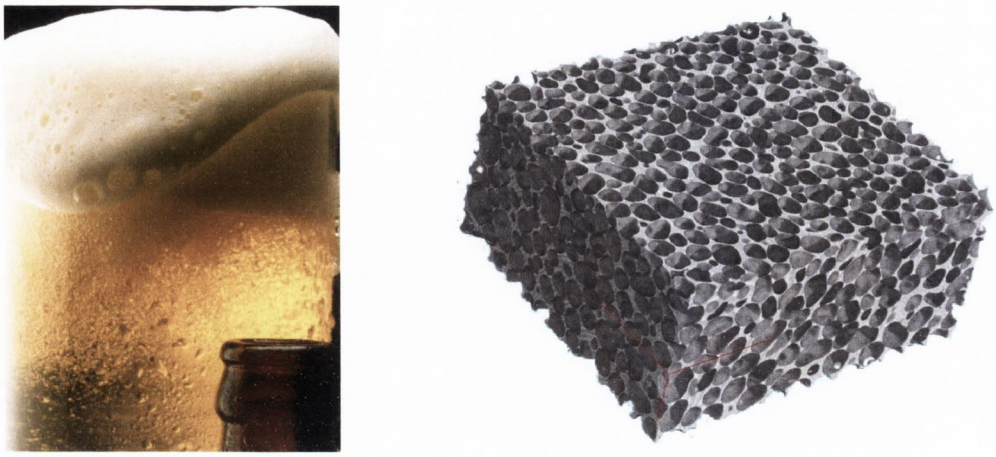

(a) (b)

Figure 1.1: Foams take diverse forms, and can be found in both day-to-day and more advanced contexts. (*a*) The foamy head of a beer is one of the most familiar (and welcome) foams. (*b*) A tomographic reconstruction of an AlMgCu metal foam, based on X-ray radioscopy (courtesy of Manas Mukherjee, Helmholtz-Zentrum Berlin).

There are several major processes which affect the evolution of a foam over time.

1. **Drainage.** The liquid in the channels — and, to a lesser extent, the films — that make up the foam flows under the influence of an external force. This force is most often gravity, although centrifuges have been used to increase drainage. Due to the ubiquitous presence of gravity on Earth, removing or reducing drainage requires special measures, including parabolic flights, sounding rockets and space flight. Drainage will be discussed in greater detail in Part I.

2. **Rupture.** As foams age, the films that make up the bubbles age and thin. As the film thickness progresses to a critical value, bubbles may rupture,

causing rearrangements and redistribution of liquid throughout the foam. The ageing of films and bubbles, and the associated rupturing, may have a strong influence on industrial scale processes such as fractionation. As such, we will discuss it in Part II

3. **Coarsening.** As the pressure of the gas in a bubble is dependent on size (with smaller bubbles having a higher internal pressure than larger ones), in a polydisperse foam there will necessarily be pressure differences between bubbles of different sizes. This leads to a phenomenon analogous to Ostwald ripening, with larger bubbles getting larger and smaller bubbles getting smaller. We will comment on coarsening where relevant, although it plays a very limited role in the experimental systems we will consider in this work (see, for example, Section 4.2).

4. **Rheology.** When a foam is subjected to an applied shear, it may flow. Foam flow is a rich topic for research, but as rheology plays a minor role in our research we will not take it into account.

In this thesis, we will consider drainage in detail. The theory behind drainage — as well as the drainage process itself — will also be considered through the triple-pronged (or 'Trinity') method: mathematical analysis, numerical simulations and modelling, and experimental verification. The effect of varying liquid fraction on the stability of individual bubbles and ensemble foams will also be examined. As all the results presented in the current work hinge on the variation of the liquid content of foams, we shall now explain foams through the lens of 'liquid fraction'.

1.3 Classifying foams by liquid fraction: wet to dry

One of the most direct ways of classifying a foam is by its liquid content. The liquid content is usually represented by the liquid fraction ϕ, where a liquid fraction of $\phi = 0.1$ means that 10% of the volume that the foam occupies consists of liquid. The gas fraction — which is simply $1 - \phi$ — is sometimes used. Liquid fraction is generally not uniform, varying under the influence of processes such as drainage. As such, it is more accurately considered as a function of position x and time t, $\phi(x, t)$. In Chapter 2, we will introduce mathematical models which describe this variation.

The values of ϕ range from less than one percent for a 'dry' foam to over twenty percent for a 'wet' foam. At each of these extremes — the wet and dry limits — foams take on the form of different interesting (and important) structures. In the dry limit, foams approximate the division of space into cells, while, in the wet limit, they approach the close-packing of spheres. This variation is shown in Figure 1.2.

An important factor in determining whether a foam in equilibrium under gravity will be wet or dry is the average size of its constituent bubbles. If a bubble is within the capillary length l_0 from the liquid surface, it will be wet (i.e., have a liquid fraction larger than about 20%). l_0 is defined as

$$l_0 = \sqrt{\frac{\gamma}{\Delta\rho g}}, \tag{1.1}$$

where γ is the surface tension of the liquid, g is acceleration due to gravity and $\Delta\rho$ is the density difference of the gas and liquid. l_0 is the length over which

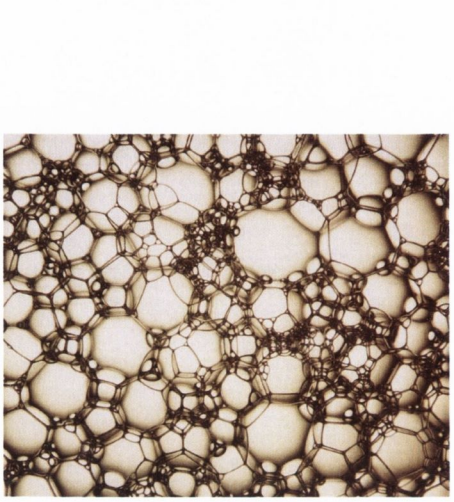

(a)

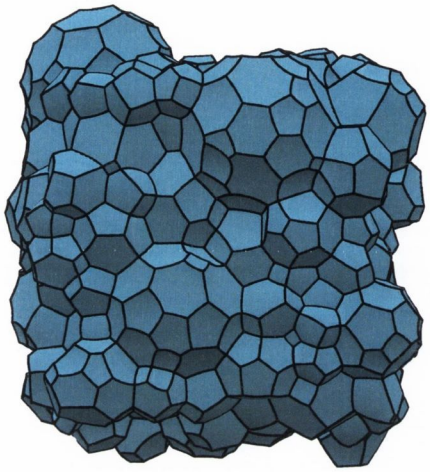

(b)

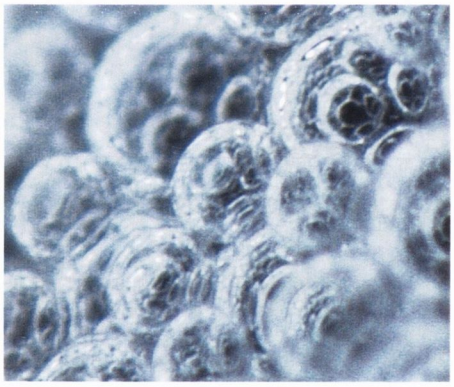

(c)

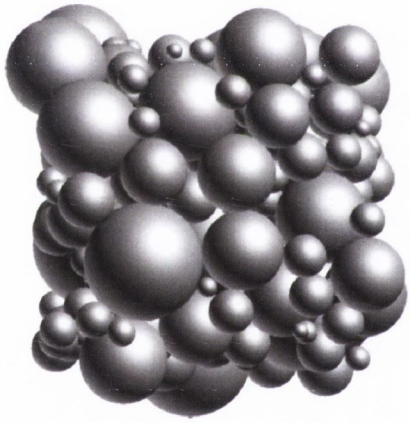

(d)

Figure 1.2: The differences between wet and dry foams are readily apparent. Typically, 3D foams are polydisperse, consisting of bubbles of many different sizes. Dry foams are shown on top and wet foams on bottom. (*a*) and (*c*) are obtained from experiments, while (*b*) and (*d*) are from computer simulations. (*a*) courtesy of M. Boran. (*c*) courtesy of A. Meagher. (*b*) and (*d*) are taken from simulations carried out by Kraynik et al. [4].

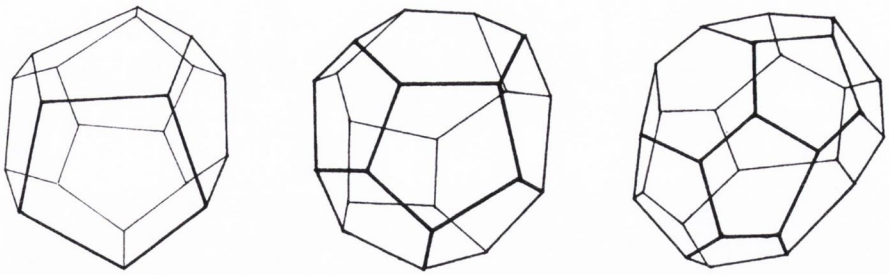

Figure 1.3: Some example polyhedral cells (with 12, 13, and 16 faces from left to right), as found by Matzke [6] in a painstaking experimental study of disordered foam. This study was recently revisited computationally by Kraynik et al. [7], who found all 36 polyhedra identified by Matzke in simulations. Image courtesy of R. Gabbrielli.

capillary forces balance drainage over gravity. The capillary length is therefore of great importance when designing experiments that require a wet foam. If the bubble diameter is d, then we can determine the number of layers of bubbles that will be wet l_0/d (the so-called Princen number [5]). Larger bubbles in equilibrium under gravity form a dry foam (although those parts of the foam within l_0 of the liquid surface may still be wetted by capillary action).

1.3.1 The dry limit

In the dry limit, commonly taken to be $\phi < 0.01$ [5], the individual soap films may be thought of as infinitesimally thin, curved surfaces. These surfaces constitute the faces of polyhedral cells. Many different polyhedral cells have been observed experimentally (a thorough list was compiled by Matzke [6]) and in simulations of random foams [7]. Some examples of Matzke's polyhedra can be seen in Figure 1.3.

The shape of these polyhedral cells of dry foams is governed by geometrical and topological restrictions, first stated by Plateau [8] in the 19$^{\text{th}}$ century[1]. Plateau's rules are as follows (a graphical explanation can be seen in Figure 1.4):

- **Faces (films) must meet three at a time.** Three cells meet symmetrically at every edge (more precisely, three films, each shared between two of the three cells). The angles at which the films meet must, therefore, be **120** degrees everywhere.

- **Edges must meet four at a time.** Six cells meet symmetrically at every corner (four edges meet, each shared by three cells as described in the first rule). The angle between edges is, therefore, $\mathbf{\arccos(-1/3) \approx 109.43}$ degrees.

Despite the seemingly intuitive nature of the rules (arising from local surface tension equilibrium at the points in question), it was not until 1976 that Taylor [10] proved rigorously that they held for minimal surfaces (i.e., surfaces that minimise their area), of which foams are an example.

Finally, the Young-Laplace equation must be taken into account when considering the surfaces that constitute the cell faces. This equation describes the capillary pressure (or pressure difference) across the interface between two fluids (water and air in an aqueous foam, for example). It expresses the balance of forces on some small element of the film in terms of the pressure difference Δp, where

$$\Delta p = \gamma \left(\frac{1}{R_1} + \frac{1}{R_2} \right). \tag{1.2}$$

[1]Both the original text and an English translation of the work may be found at http://www.susqu.edu/brakke/PlateauBook/PlateauBook.html

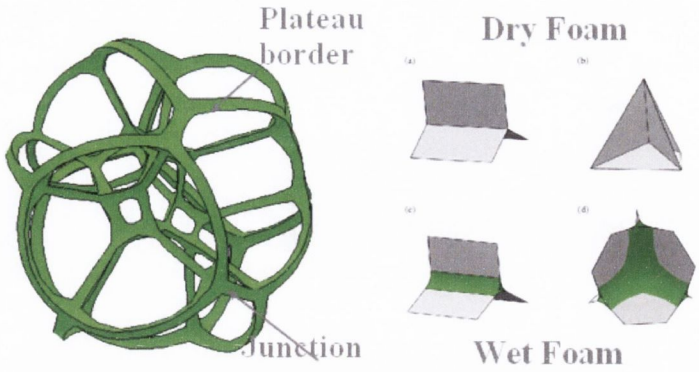

Figure 1.4: Plateau's rules of equilibrium require three films to meet to make an edge, and four edges to meet in a tetrahedral junction. The rules hold for dry foams and for foams with small values of liquid fraction, but foams containing large amounts of liquid ('wet' foams) can contain junctions of more than four edges (or six cells) [9].

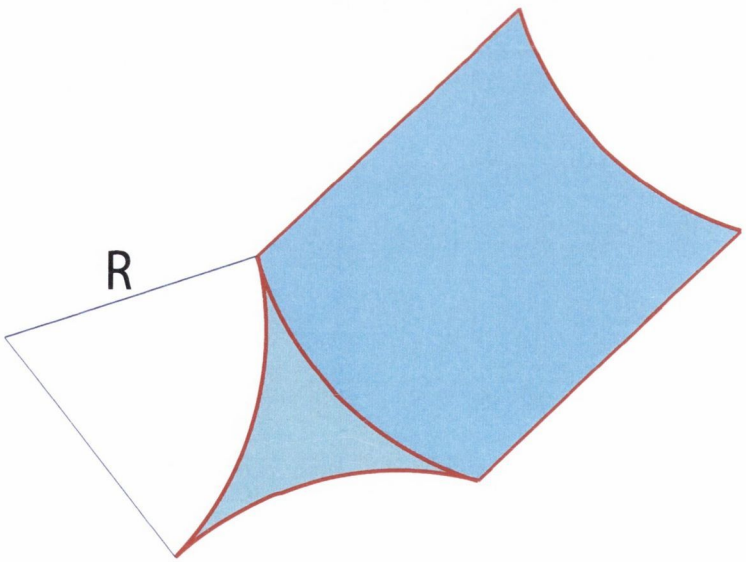

Figure 1.5: A Plateau border in schematic form, showing the cross-sectional shape of the border. The curved shape of the Plateau border results from the Young-Laplace equation.

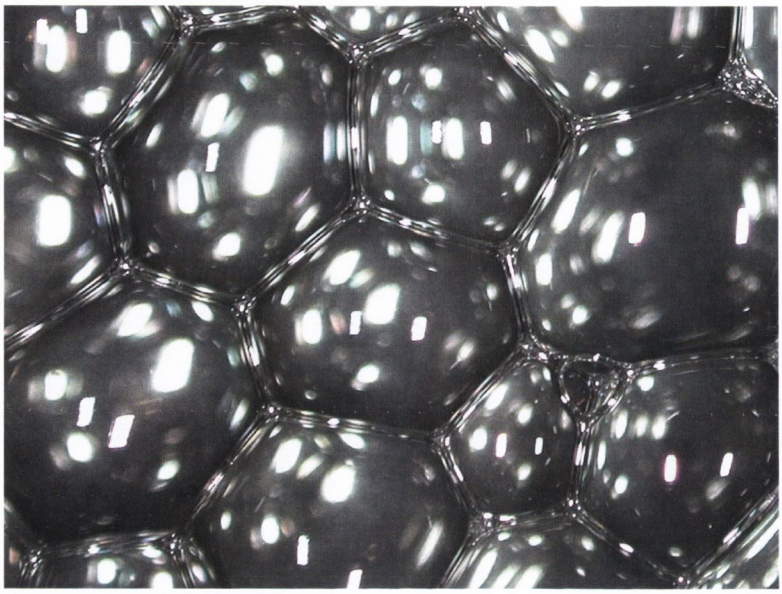

Figure 1.6: A photograph of the surface of a foam. The curvatures of the films are made visible by the reflections of light on the surface. Note the complex nature of the surfaces. Accurately describing foams often requires the use of computer modelling due to this complexity. As a result, full numerical descriptions of foams have only been possible in recent years as computing power has increased.

Here, γ is surface tension and R_1 and R_2 are the two principal radii of curvature. In the general case, R_1 differs from R_2. For the case of a sphere or spherical surface, $R_1 = R_2$.

The surface may therefore have a complicated form which can be difficult to describe mathematically, depending on local topology and forces. (An example can be seen in Figure 1.6.) Therefore, it is necessary to use numerical simulations for almost all detailed analysis and study of foam structures. A more in-depth look at software used in these simulations may be found in Section D.1.

1.3.2 The wet limit

In the wet limit, the bubbles become spherical (see Figures 1.2c and 1.2d). As such, the foam begins to share features with sphere packings [11]. Note that the actual sphericity of the bubbles will depend on their size (as larger bubbles are 'softer', or more compressible). It is important to note that a distinction exists between a foam in the wet limit and a 'bubbly liquid'. Increasing the liquid fraction past the wet limit leads to loss of contact between neighbouring bubbles, and the resulting system (while still of scientific interest) is no longer considered a foam. As such, we will not elaborate on it further. The wet limit defines a maximum liquid fraction — $\phi_c = 0.36$ [5] — which corresponds to a random close packing of spheres [11].

As observed with dry foams, there are some restrictions on the possible structures that such 'sphere packings' may take (restrictions that also arise in the idealised models used in granular media research [1]). Firstly, each sphere must be in contact with at least three of its neighbours. Spheres that do not meet this criterion are termed 'rattlers', as they can 'rattle around' in cages made of other spheres. Secondly, despite the minimum contact number being three, the average number of sphere contacts in a disordered packing should be at least six for a mechanically stable packing [11]. This arises from simple consideration of degrees of freedom, with two confining forces needed for each of the three x, y, z spatial axes. (This is not an exact result, nor mathematically proven, but is approximately valid in practice and widely used in sphere packing research. It is, however, possible to design stable, ordered structures with fewer contacts.)

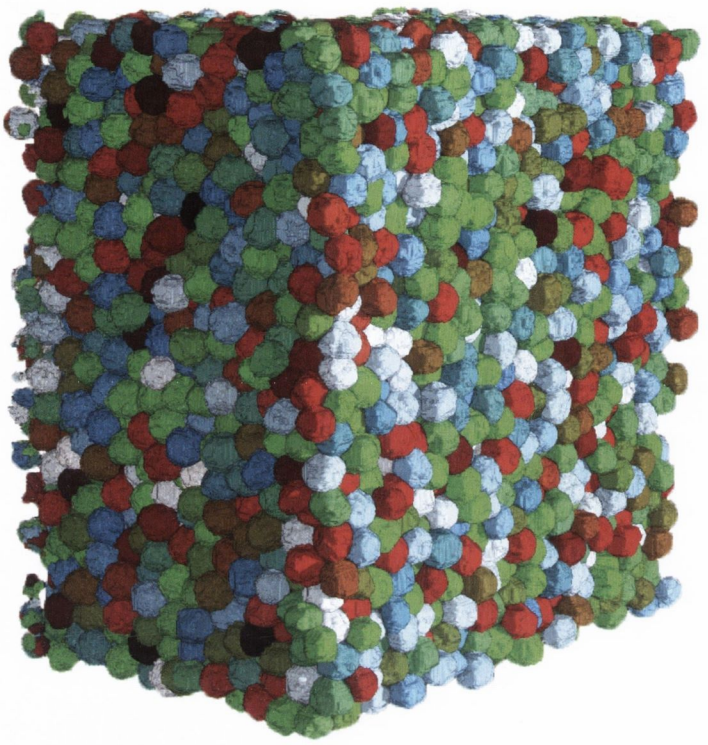

Figure 1.7: A tomographic reconstruction of a 3D monodisperse foam (courtesy of A. Meagher). Tomography of this type allows the internal structure of foams to be examined and visualised. Previous techniques involved visually identifying crystal structures by refraction in the surface layers, limiting examination of the internal sections of foams.

Bragg and Nye [12] were the first to observe that wet foams consisting of small bubbles readily form crystalline structures, driven solely by surface tension. Recent experiments [13] suggest that the face-centred cubic (fcc) structure predominates. Ongoing experiments by Meagher et al. [14] using X-ray tomography to explore the internal structure of monodisperse foams (i.e., all bubbles have equal volume) may shed some light on this phenomenon. An example of a tomographic reconstruction of a 3D foam can be seen in Figure 1.7.

1.3.3 Between the two limits

Neither the dry nor the wet limit fully describes a real foam, with experimental and real-world foams tending to fall somewhere between the two. It is therefore necessary to consider liquid fractions in the intermediate regime.

As we start to add liquid (in infinitesimal amounts) to a foam in the dry limit, the first changes occur in the edges where the films meet. These cell edges swell to form the so-called Plateau Borders (see Figure 1.4 and Figure 1.5 for an illustration of what these borders look like). Initially, we may still treat the films as infinitesimally thick (i.e., we may neglect the liquid content of the films), provided we are close to the dry limit.

For small enough liquid fractions, Plateau's rules are still approximately correct. Further liquid fraction increases lead to violations of the rules, and our ability to mathematically describe the foam surface precisely becomes more and more limited.

As we continue towards the wet limit, the cells of the foam become deformed spheres, with the nature of the deformation dependent on how the foam is confined. Foams in this regime are not easy to describe and, outside of the wet and dry limits, we must rely on numerical simulations to describe and analyse foams. Some idealised models may also be employed, such as the representation of bubbles by overlapping spheres [15].

The region of intermediate liquid fraction also contains a lot of the interesting physics of foam drainage. Liquid fraction in this range is too large to be ignored, and yet still small enough to be handled by analytical drainage models. The approach taken in our theoretical analysis (as outlined in Chapter 2 and discussed

in detail in Appendix 2.2) involves treating the foam as a continuous medium (i.e., a macroscopic model of drainage), building upwards from the drainage through a single Plateau border. The model is simple enough to be explorable numerically in reasonable amounts of computing time, while still retaining enough of the inherent physics to make meaningful comparisons with experiments and real-world systems of interest.

1.4 Foam structure for finite values of liquid fraction

The variation of liquid fraction has a significant effect on many different foam characteristics. In later chapters, we will examine drainage — how liquid fraction changes in space and time under gravity, outlined in Part I — and the lifetime of ageing foams (Part II).

We will outline here a simple example of the effects changing liquid fractions can have on a foam: the problem of identifying minimum-energy structures. Although the most commonly encountered foams are disordered, one can generate *ordered* foams using monodisperse bubbles. Such ordered foams are often used in research on minimal-energy surfaces [3].

The problem of how best to partition space is a long-standing one. While often considered a purely mathematical concern, there are several real-world applications of solutions to this problem, such as in the design of buildings and applications where packing efficiency is at a premium.

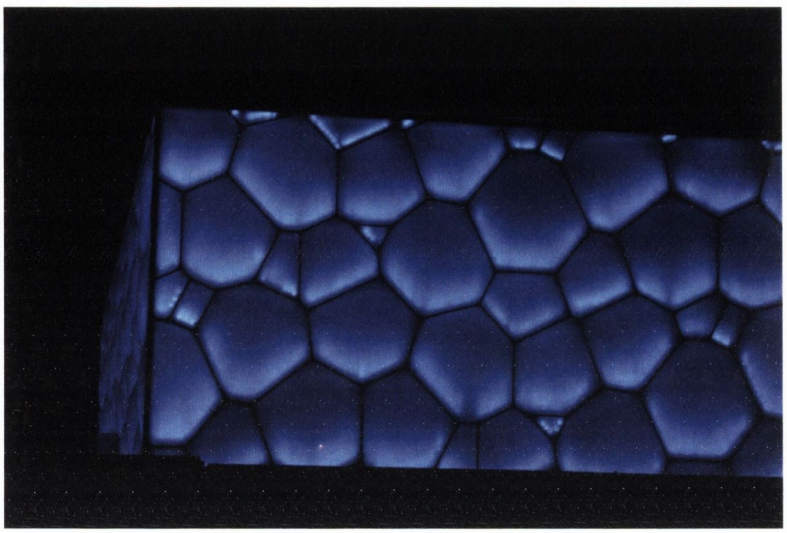

Figure 1.8: The Water Cube, built for the Beijing Olympics. The design of this building is based around the Weaire-Phelan foam structure, the current best space-partitioning foam structure. Image courtesy of Chris Suderman (Creative Commons).

The variation of liquid fraction between the wet and dry limits also has a significant effect on the structures of lowest energy and on the mechanical stability of these structures.

The humble honeybee long ago solved the problem of partitioning 2D space into equal-area cells while minimising the amount of material used to build the walls (or surface length). Hexagonal honeycomb structures have been mathematically proven to be the most efficient structure for 2D. But what is the counterpart in 3D? How can we partition space into cells of equal *volume* while minimising *surface area*?

Various foams have been put forward as the structure of lowest energy. Lord Kelvin proposed the first such solution in 1887 [16]. The Kelvin structure consists of a body-centred cubic (bcc) space-filling arrangement of truncated octahedrons

(a 14-sided polyhedron with six square faces and eight hexagonal faces). This structure was long thought to be the most efficient 3D structure. However, more than a century later, Weaire and Phelan computed a structure with a lower surface area [16, 17], beating Kelvin's structure by 0.3% (a substantial reduction in this context). The Weaire-Phelan structure is shown in Figure 1.9, alongside the Kelvin structure.

The Weaire-Phelan structure differs from the Kelvin structure in that it consists of two different cells (an irregular dodecahedron with pentagonal faces and a tetrakaidecahedron with two hexagonal and twelve pentagonal faces), albeit with the same volume. As of publication of this work, it is still the most efficient structure known for the partition of 3D space. It has, however, not been mathematically proven to be optimal. Recent experimental work has lead to the first laboratory realisation of a Weaire-Phelan foam [18].

Previous simulations of minimal energy surfaces have used dry foams (zero liquid fraction simulations) [3, 7]. However, foams in experiments always have a finite liquid fraction ϕ and, as such, we need to include this in our simulations. This liquid fraction can have significant effects on the stability of foam structures, with certain structures only experimentally accessible below specific threshold values of ϕ. While dry foams have been extensively studied, wet foams have not, largely due to the large increase in computer power required to accurately model the Plateau border network. Examples of dry (i.e., starting simulation) and wet foam simulations can be seen in Figure 1.10. It is apparent by visual inspection that the wet foam is more representative of a real Weaire-Phelan foam than the starting simulation.

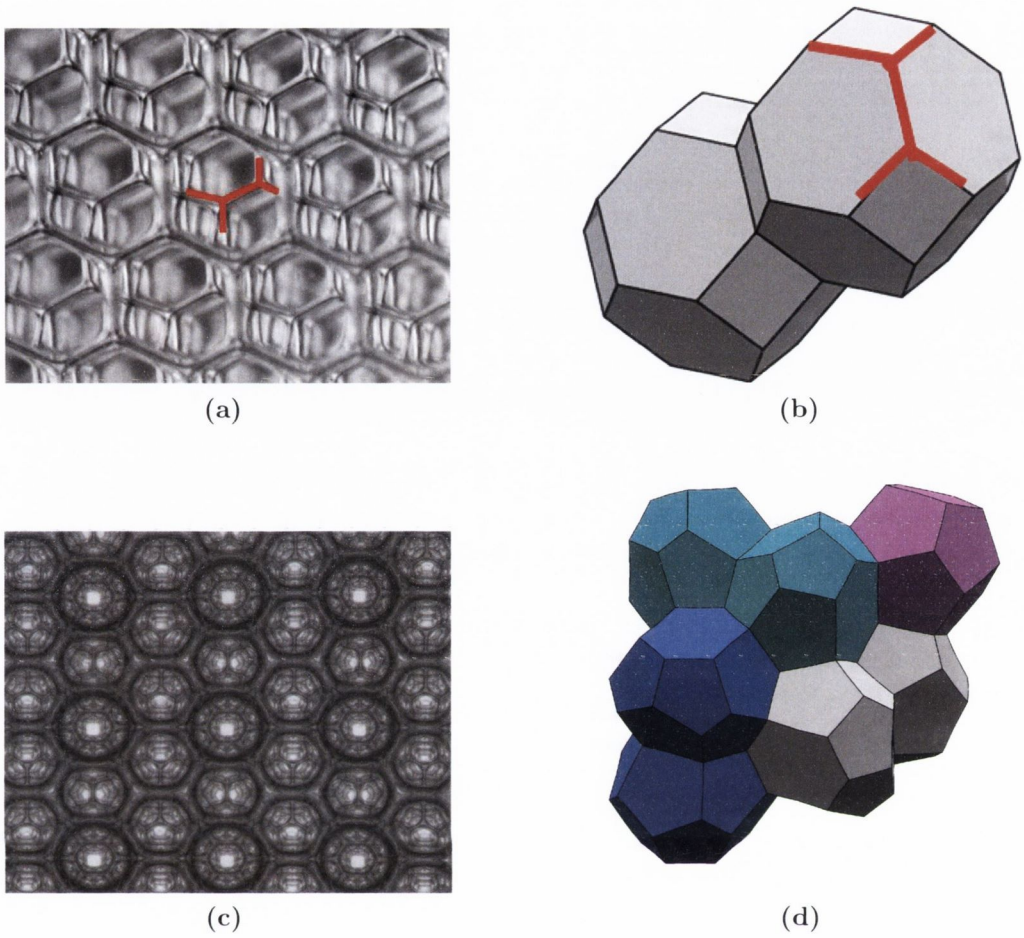

Figure 1.9: The top row ((*a*) and (*b*)) shows the Kelvin foam, while the bottom ((*c*) and (*d*)) shows a Weaire-Phelan foam. In both cases, the left image is experimental, while the right is from simulation. It is readily apparent that the Weaire-Phelan is a more complex structure, consisting of two different (but equal-volume) bubble types.

We conducted Surface Evolver simulations to find the limits of stability of the Kelvin and Weaire-Phelan foam structures as liquid fraction is increased. (A detailed introduction to the Surface Evolver software may be found in Appendix D.1.) We tracked the surface energy per bubble E as ϕ is varied, which points to instabilities in the foam structure. The per-bubble energy is most useful for comparing different ordered structures, as it is independent of foam structure (e.g., the num-

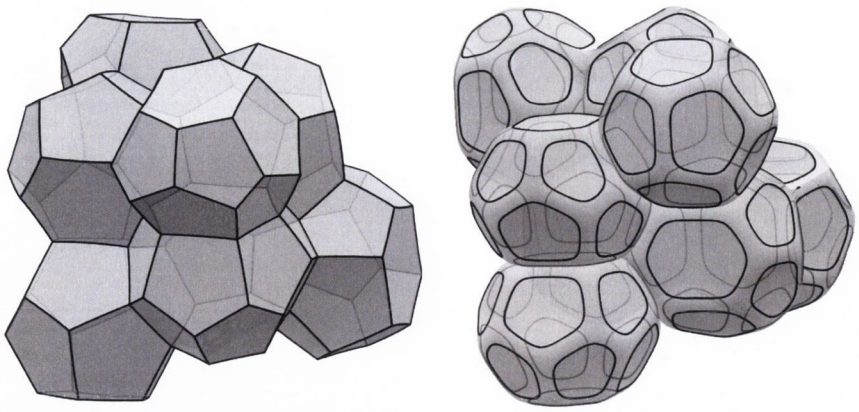

Figure 1.10: The difference in the structure of a foam with increasing liquid fraction is shown here. (a) shows a dry foam with zero liquid fraction, (b) shows a foam with a liquid fraction of 1%. Note the curved faces in the foam (most apparent in (b), which show how real foams differ from simple Voronoi tessellations of space [15]). The structures were calculated using the Surface Evolver.

ber of bubbles in a unit cell). A plot of energy per bubble is shown in Figure 1.11. Note that the value of the surface energy per bubble (equivalent to the surface area in these simulations) for a Kelvin foam in the dry limit — $E \approx 5.35$ — plays a role in the derivation of models of foam drainage, which will be outlined in Chapter 2.

Taking the derivative of this curve, we may define a stability threshold as

$$\frac{\partial E}{\partial \phi} = 0. \tag{1.3}$$

Below this threshold, increasing liquid fraction reduces the average energy of the bubbles in the foam, as reported by the Surface Evolver. Increasing ϕ past this point increases the surface energy of the simulated foam. The real foam would resist such energy increases and would change structure (e.g., by losing contacts or by rearranging bubbles) to reduce energy again.

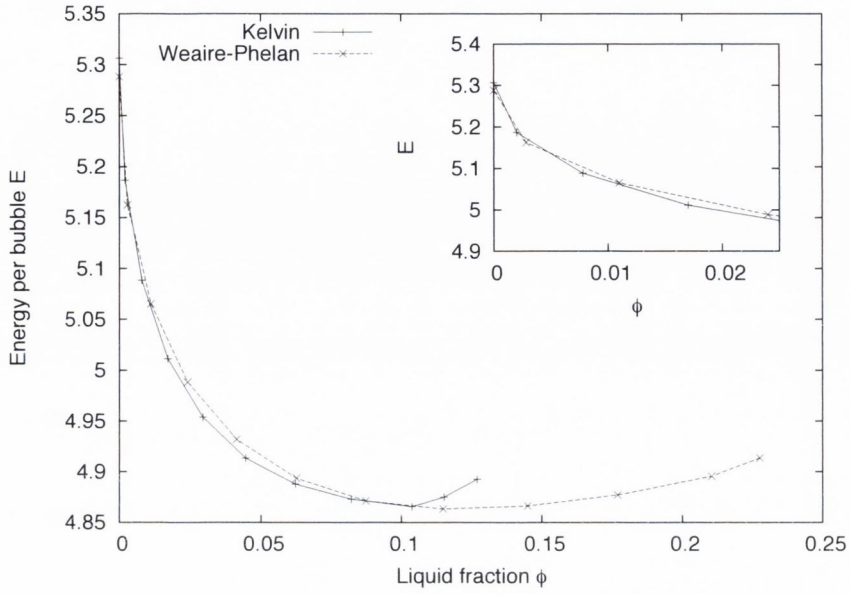

Figure 1.11: As liquid fraction is increased, the surface energy per bubble initially increases. However, after a certain point (dependent on the foam structure), further increases in liquid fraction lead to increased energy. The inset shows that, while the Weaire-Phelan is the lowest-energy dry foam, by $\phi = 0.01$ the Kelvin foam is clearly the structure of lowest energy.

A plot of $\partial E/\partial\phi$ for both Kelvin and Weaire-Phelan foams is shown in Figure 1.12. The Kelvin foam crosses the threshold at $\phi = 0.11 \pm 0.01$, while the Weaire-Phelan crosses at $\phi = 0.14 \pm 0.01$. These values agree well with published results for the stability of these structures by Phelan et al. [19]

We may also predict which structure is preferred for a specific liquid fraction from our energy calculations. While the Weaire-Phelan foam is the lowest energy structure for perfectly dry foams, this is not the case as liquid fraction changes. We find that by $\phi = 0.01$ the Kelvin foam has become the structure of lowest energy.

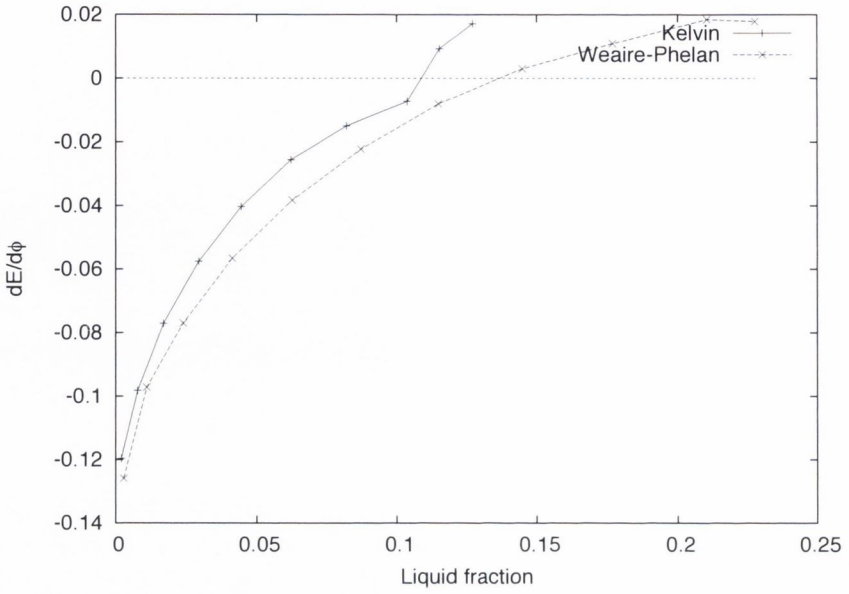

Figure 1.12: As liquid fraction is increased, the surface energy per bubble initially decreases. However, at some point, further increases in ϕ increase the energy per bubble. For the Kelvin foam, this transition occurs at $\phi = 0.11 \pm 0.01$, and, for Weaire-Phelan, it occurs at $\phi = 0.14 \pm 0.01$.

1.5 Summary

Despite their familiar nature and deceptively simple appearance, foams are integral to many industries and avenues of research. In this work, we will necessarily neglect some of this ubiquity and instead focus on a handful of examples which cover a range of the applications of foams — from modelling industrial processes, through advanced materials research, and on to use as a tool in teaching statistics.

Our work focused on the flow of liquid through the channels that make up foams, and how that drainage affects the physics and overarching behaviour of the systems we study. We will show how such mathematical analysis can be explored

by numerical simulation and probed via experiment, and will provide thorough analyses of the steps required to move from these foundations to full models of real systems of interest.

We will introduce elementary foam drainage theory, and show how it can be used for modelling and analysis of experimental and industrial set-ups used in the industrial process of fractionation. Our analysis will then be extended to provide guidelines for the design and operation of industrial fractionation processes. We will also compare drainage theory to experimental data, and use such comparisons to show how important foam characteristics can be determined in a novel way. In a world where the finite nature of our resources is becoming painfully obvious to all, this 'Trinity' approach has the potential to provide real improvements to processes of enormous importance.

The liquid fraction of a foam has significant effects on the lifetime and stability of foams. We shall present experiments and statistical analysis of the lifetimes of ageing soap films. This stability has important implications for the design and operation of experiments in which the deterioration of foam plays a role.

A note on style

One of the first choices one must make when preparing a document like this is the writing style. I find the personal or active voice — using 'I' and 'we' — both more pleasant to read and easier to follow (from a narrative standpoint).

Even though I have been the primary driver of the research contained within this Thesis, I would be doing a great disservice to many people — my supervisor, co-workers, colleagues and even friends — if I did not acknowledge their interac-

tions, inputs and assistance. Research is seldom a purely individual effort. For those reasons, and for clarity of language, I will therefore use 'we' throughout this Thesis.

Part I

Foam Drainage

Chapter 2

Introduction to foam drainage theory

The mathematical modelling of foam drainage (including the case of fractionation, which will be discussed in a later section) goes back to the 1960s[1]. Leonard and Lemlich [21] had all the elements of the model that prevails today, but did not conduct the mathematical analyses that would have exposed its rich variety of non-uniform and time-dependent solutions. Only uniform profiles of steady drainage were considered. The later contributions of Gol'dfarb et al. [22], Verbist et al. [23], Koehler and Hilgenfeldt [24], Cox et al. [25], and Saint-Jalmes and Langevin [26] developed the field in its full generality. Models of foam drainage have previously been applied with qualitative and semi-quantitative success to a range of experiments — including "free drainage" and "forced drainage" [27, 28]

[1] Although brief theoretical discussions of the process of drainage had been presented by Bikerman [20] in 1953, no serious modelling was attempted.

and foamability tests [29] in a single column. (For a more thorough summary of early foam drainage theory, see the work of Weaire et al. [28].)

In this Chapter, we will introduce the basic ideas behind foam drainage theory and present a theoretical model for the drainage process. We will also discuss some mathematical solutions of the resulting foam drainage equation and show (using a simple example) how drainage theory may be used to understand experimental results.

2.1 Modelling foam drainage

Under the action of gravity, liquid will flow through a foam — specifically through a network of Plateau borders (PBs) — as sketched in Figure 2.1. The viscosity, surface tension and pressure differences within the foam will affect the flow.

While liquid flowing through a pipe cannot affect the geometry of the pipe, the PB network will change and swell to accommodate additional liquid and, thus, change the value of the local liquid fraction in time and space $\phi(x, t)$. We therefore need a model that can describe the liquid fraction of the foam — the amount of the foam volume consisting of liquid — as a function of both time and position.

As the liquid drains through the foam under the influence of gravity, it is countered by viscous drag forces. Dissipation occurs in both the PBs and the nodes (or junctions) where the PBs meet. Different flow characteristics will be observed depending on the nature of the dissipation, which, in turn, depends on the surface characteristics of the foam.

Which dissipative model is more applicable to a given foam is largely dependent on the surfactant type used. In the case of a foam stabilised by a surfactant

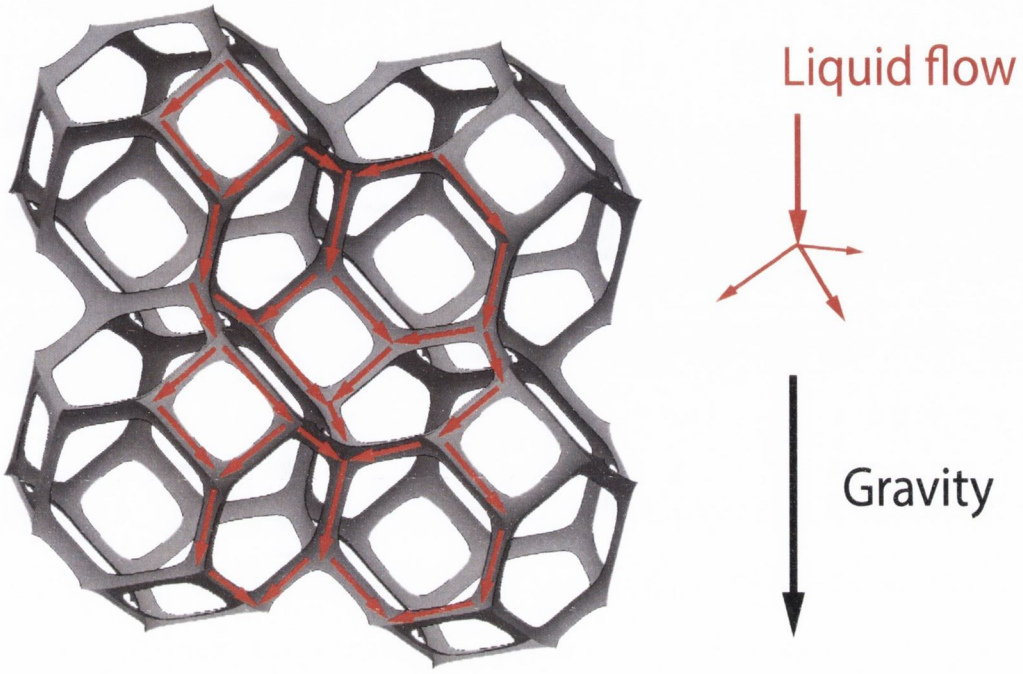

Figure 2.1: When a foam is subject to an external force, such as gravity, the liquid in that foam flows through the network of channels and nodes (the Plateau border network). The figure shows this process in a wet Kelvin foam, with the red arrows indicating the flow of liquid.

with mobile interfaces, liquid draining through the PBs will undergo plug flow. The main source of dissipation will thus be in the nodes [24], where the liquid is redistributed — **node-dominated** drainage. Conversely, a foam with immobile interfaces (such as those discussed in Section 2.4) will experience Poiseuille-type flow in the PBs, leading to dissipation forces mainly in the channels [23] — **channel-dominated** drainage.

This difference may be understood intuitively by considering the liquid flow as laminar. If the interfaces are immobile or rigid, there will be no flow on the walls

and a maximum flow in the centre of the PB (Poiseuille flow), resulting in a large velocity gradient that, in turn, leads to dissipative shear forces acting against the flow. As the PBs contain more wall area than the nodes, the large majority of this type of dissipation will occur in the PBs, and the contribution of the nodes may be neglected. This is channel-dominated drainage. Conversely, if the interfaces are mobile, then we can expect plug flow in the PBs and the majority of the dissipative forces will be due to shear in the nodes (as the liquid flows out into multiple PBs, as shown in Figure 2.1). We may, therefore, neglect the contribution of the PBs, resulting in node-dominated drainage.

Recently, work has been undertaken to explore the regions between these two extremes [30] to derive models that can include contributions from both dissipation mechanisms (applicable to surfactant mixtures in real foams, for example). In this work, we will present theoretical models based on channel-dominated drainage theories, as outlined in Section 2.2. Channel-dominated drainage has the great benefit of being easily explored analytically.

2.2 The Foam Drainage Equation

The channel-dominated Foam Drainage Equation (FDE), first presented by Verbist et al. [23], describes how the liquid fraction $\phi(x,t)$ changes as a function of position x and time t. The full form of the FDE is given by

$$\frac{\partial \phi}{\partial t} + \frac{1}{\eta^*}\frac{\partial}{\partial x}\left(\frac{\rho g}{l_V}\phi^2 - \frac{C\gamma}{2}\sqrt{\frac{\phi}{l_V}}\frac{\partial \phi}{\partial x}\right) = 0, \tag{2.1}$$

where

- γ is the surface tension, ρ is the density of the liquid phase, and g is acceleration due to gravity,
- $\eta^* = 3 \times 50 \times \eta$, where 3 is a geometric factor arising from averaging over the PB network, 50 is a 'drag coefficient' valid for Poiseuille-type flow in a PB, and η is the bulk liquid viscosity,
- C is a geometrical constant relating to the cross-sectional shape of the PBs, and is given by $C = \sqrt{\sqrt{3} - \frac{\pi}{2}}$,
- and $l_V \simeq 5.35 V_b^{-2/3}$ is the total length of PBs per unit volume of foam. Here, V_b is the average volume of a bubble in the foam and the constant 5.35 arises from geometric consideration of a Kelvin foam. Similar values are found for a large variety of different foam structures (to within 2%) [7].

We may estimate the bubble volume V_b from measured PB lengths by again approximating the bubbles in the foam as Kelvin cells. A Kelvin cell with edge length L has volume $V_b = 8\sqrt{\pi}L^3$.

A full derivation of the FDE may be found in Appendix A. As the full equation is quite unwieldy, we will gather the assorted constants into two constants — c_1 and c_2 — leading to a final FDE:

$$\frac{\partial \phi}{\partial t} + \frac{\partial}{\partial x}\left(c_1 \phi^2 - c_2 \phi^{\frac{1}{2}} \frac{\partial \phi}{\partial x}\right) = 0, \tag{2.2}$$

where c_1 and c_2 are given by

$$c_1 = \frac{\rho g}{l_V \eta^*}, \tag{2.3}$$

$$c_2 = \frac{1}{2} \frac{C\gamma}{l_V^{1/2} \eta^*}. \tag{2.4}$$

c_1 has dimensions of velocity and c_2/c_1 dimensions of length. c_2/c_1 is (to within a constant of order unity) equal to the Princen or capillary length, i.e., the height of that section of wet foam that exists due to capillarity when a foam is in contact with underlying liquid [5] under acceleration due to gravity. c_1 is (again, to within a constant of order unity) equal to an important constant in elementary drainage theory [5]: in steady uniform drainage, the liquid fraction is proportional to the flow velocity with the constant of proportionality given by $1/c_1$ (as can be seen in Equation 2.3.2).

Numerically solving the FDE results in a description of how the liquid fraction $\phi(x,t)$ evolves over time from some given starting conditions (liquid fraction profiles). An example of such a solution for the case of an aqueous foam with a standard surfactant (sodium dodecyl sulfate, or SDS) in contact with a liquid reservoir is shown in Figure 2.2.

2.3 Example solutions of the FDE

Here we will present some solutions of the FDE and use one to conduct a simple analysis of real-world experimental data (shown in Section 2.4). While many boundary conditions for the FDE require numerical integration or other approximations to be made, in several cases analytic solutions exist. Note that all of the examples given here are derived from the channel-dominated FDE described in the previous Section.

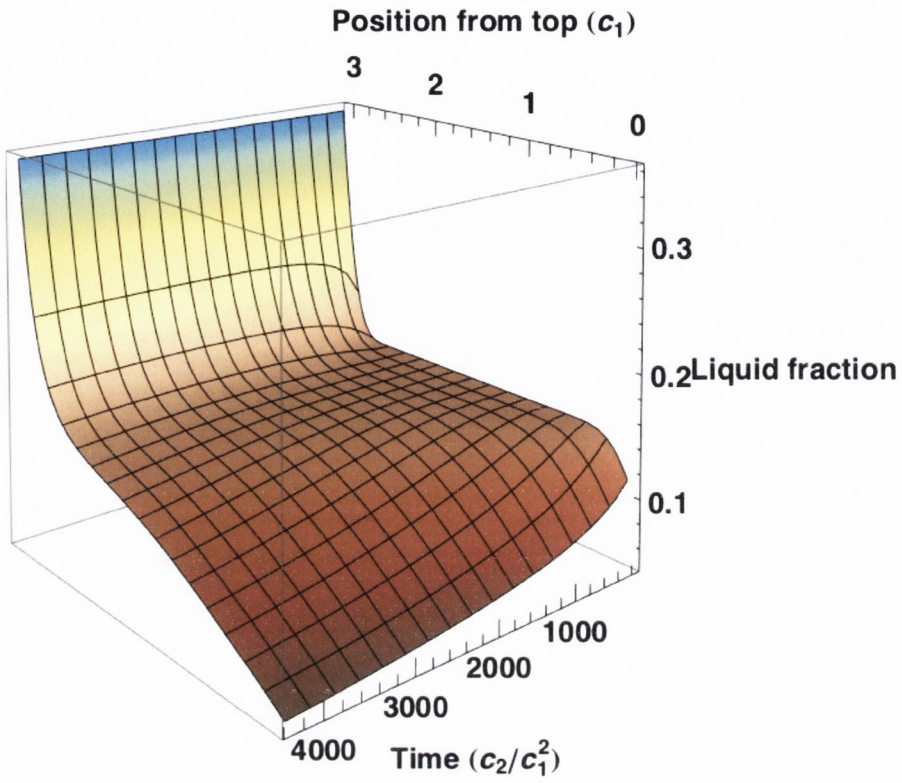

Figure 2.2: Numerically integrating the full FDE allows us to visualise and explore foam systems which have no analytical solution available. The figure shows an example numerical solution for a freely draining aqueous foam stabilised with a standard surfactant (sodium dodecyl sulfate, or SDS). The foam is in contact with a liquid and starts from an initially uniform liquid fraction profile (except where in contact with the pool). The axes are scaled in terms of our parameters c_1 and c_2.

2.3.1 A foam in equilibrium

When the foam is in equilibrium (i.e., when $\partial\phi/\partial t = 0$), a liquid fraction profile can be analytically found. Looking at Equation 2.2, we note that the term inside

the parentheses is simply a flow rate. If the foam is in equilibrium, then we can set this flow to zero, such that

$$c_1\phi^2 - c_2\phi^{1/2}\frac{\partial\phi}{\partial x} = 0 \tag{2.5}$$

throughout the entire foam. This gives the following solution for the liquid fraction profile:

$$\phi(x) = \frac{4\,\phi_1\,c_2^2}{(2\,c_2 + c_1\sqrt{\phi_1}\,(x + x_1))^2}, \tag{2.6}$$

where $\phi_1 = \phi(x_1)$ is the value of liquid fraction at some position in the foam. If the foam is floating on liquid, we can set $\phi(x_1 = 0) = \phi_c = 0.36$, as discussed in Section 1.3.2. In Chapter 3, we will look at draining foams where the local flow rate has a finite value.

2.3.2 Forced drainage — solitary wave solution

A common process in experiment and industry is forced drainage, where liquid is added to a foam and propagates through the PB network, wetting the foam in the process. We will comment on this process in an industrial context when discussing foam fractionation in Chapter 3, specifically in Section 3.4.2.

Verbist et al. [23] suggested solutions of the FDE for the case of forced drainage on a dry foam, where the propagating wetting front is a solitary wave moving with some constant velocity v. The solution is (in our notation):

$$\phi(x,t) = \begin{cases} \frac{v}{c_1}\tanh^2\left(\sqrt{\frac{v}{c_1}}\left(\frac{c_1}{c_2}(x - vt)\right)\right) & x \leq vt \\ 0 & x > vt. \end{cases}$$

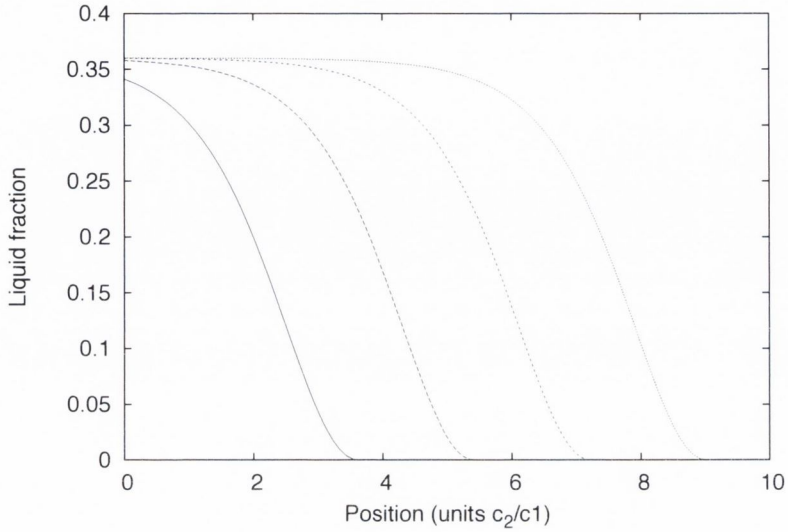

Figure 2.3: Analytical solutions of the FDE (Equation 2.3.2) for a dry foam undergoing forced drainage show the shape of the solitary wave moving through the foam. Note the propagation of the wave front from left to right (i.e., from the top of the foam downwards) with increasing time, and the constant wave shape.

Figure 2.3 shows numerical solutions of the FDE for a dry foam undergoing forced drainage. The wave front propagates from from left to right (i.e., from the top of the foam downwards) as time progresses, with a constant velocity.

In the case where the liquid is added to an already wet foam, the analytic solution becomes implicit (see [23]). However, numerical solutions may still be calculated as before, which will be discussed in Section 3.4.2.

2.3.3 Linear approximation to the FDE

It is possible to reduce the FDE to a first-order equation in x by neglecting any contribution from surface tension (which causes pressure variations in the foam). This approximation is more valid in the dryer regions of the foam (farther above the liquid surface than the capillary length given by Equation 1.1), as can be seen in Figure 2.4.

Starting from Equation 2.2, and setting surface tension γ to zero (which sets c_2 to zero), we have

$$\frac{\partial \phi}{\partial t} + c_1 \frac{\partial \phi^2}{\partial x} = 0. \tag{2.7}$$

Kraynik [31] presented a solution for the linear approximation of the FDE, reproduced here in our notation:

$$\phi(x,t) = \frac{1}{2c_1} \frac{x - x_a}{t - t_a}, \tag{2.8}$$

where x_a is an offset in space (the point where all linear profiles converge) and t_a is an offset in time. In the next Section, we will use Equation 2.8 to show how foam drainage theory may be used to analyse free drainage experiments.

2.4 Example of analysis using the FDE — a linear case

(We would like to thank C. Stubenrauch for kindly providing the experimental data we use throughout this section.)

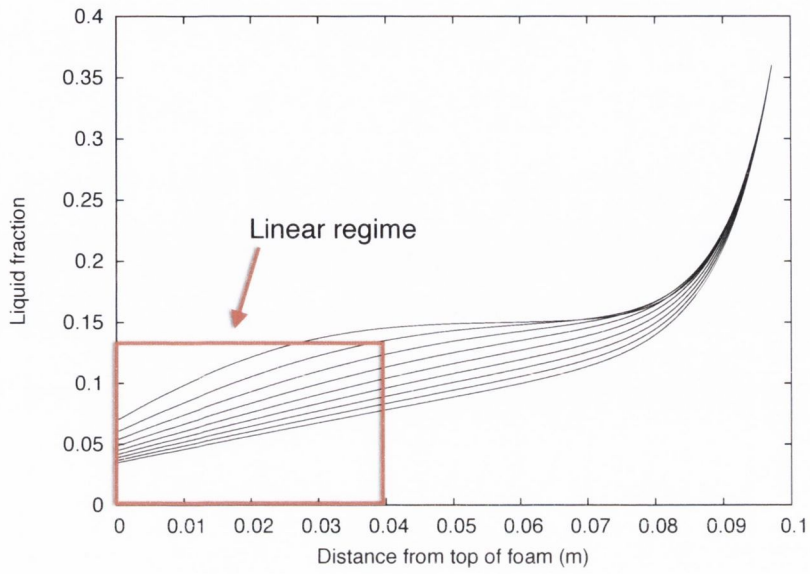

Figure 2.4: Plotting numerical solutions of the full foam drainage equation (i.e., liquid fraction as a function of position and time, with the base of the foam on the right) clearly shows that the dryer top parts of the foam are reasonably linear at all times. Here, the first-order approximation of the FDE is sufficient.

We will now look at how one can apply a linear approximation of the FDE to experimental data and extract useful information about the foam (a dry run, so to speak, for the analysis of drainage experiments presented in Chapter 4).

Carey and Stubenrauch [32] recently presented work analysing free drainage of aqueous foams using mixtures of various surfactants (one non-ionic, C_{12}DMPO, and one ionic, C_{12}TAB). They found that all surfactant mixtures tested showed Poiseuille-type flow and, as such, we would expect solid agreement between their experimental data and solutions of the channel-dominated FDE.

The experimental data consists of measurements of liquid fraction (at different heights throughout the foam sample) taken at regular time intervals using a mea-

surement technique based on electrical conductivity. As such, we have a full set of liquid fraction profiles $\phi(x,t)$ for multiple foams, each with a different surfactant mix. We will present results based on one such set of profiles — a foam generated with 1:1 mix of C_{12}DMPO and C_{12}TAB surfactants.

We start our analysis by noting that the data appears to be linear (as shown in Figure 2.5) and that the linear approximation to the FDE discussed in Section 2.3.3 should be valid. The linear FDE has a known analytical solution [31], presented in Equation 2.8.

This equation allows us to quickly compute a full liquid fraction profile, provided we know c_1, x_a and t_a. Recall that $c_1 = \frac{\rho g}{l_V \eta^*} = \frac{\rho g}{5.35 V_b^{-2/3} \times 150 \eta}$. For the experimental data under examination here, the density and viscosity of the solution will be effectively equivalent to that of pure water at the surfactant concentrations used (twice the critical micelle concentration). Therefore, the only unknown value in c_1 is the bubble volume V_b.

We now set out to determine these values from the experimental data. First, we differentiate Equation 2.8 with respect to x:

$$\frac{\partial \phi(x,t)}{\partial x} = \frac{1}{2c_1} \frac{1}{t - t_a}. \tag{2.9}$$

Note that the spatial offset x_a is no longer present. Equation 2.9 allows us to calculate the slope of the linear profile at some time t, provided we know t_a and the bubble volume V_b. We can also calculate the slopes directly from the data and fit Equation 2.9 to those slopes, treating t_a and V_b as fitting parameters. This is shown in Figure 2.6.

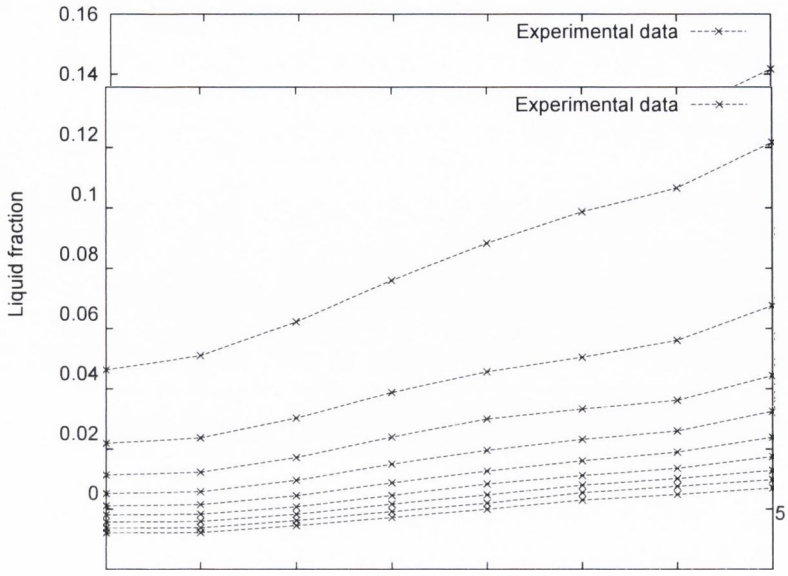

Figure 2.5: Liquid fraction profiles showing the evolution of $\phi(x,t)$ for a foam stabilised using a 1:1 mix of C_{12}DMPO and C_{12}TAB surfactants. Note the linear nature of the profiles.

With best-fit values for t_a and V_b known, we can return to Equation 2.8 to work out x_a. We fit this equation to the experimental data for every available time t, which provides a series of estimates of x_a. These can be averaged to arrive at a final value.

With x_a, t_a, and V_b now known (taking values $x_a = -0.12 \pm 0.01\,\text{cm}$, $t_a = -20 \pm 2\,\text{s}$, and $V_b = 8.4 \pm 0.7\,\text{mm}^{-3}$ for this experimental data), we can use Equation 2.8 to directly calculate liquid fraction profiles for our foam (as there are no free parameters). Figure 2.7 shows such a recreation plotted together with the original data, with excellent agreement observed. Figure 2.8 shows the same data, but zoomed out slightly to show x_a (the convergence point or spatial offset).

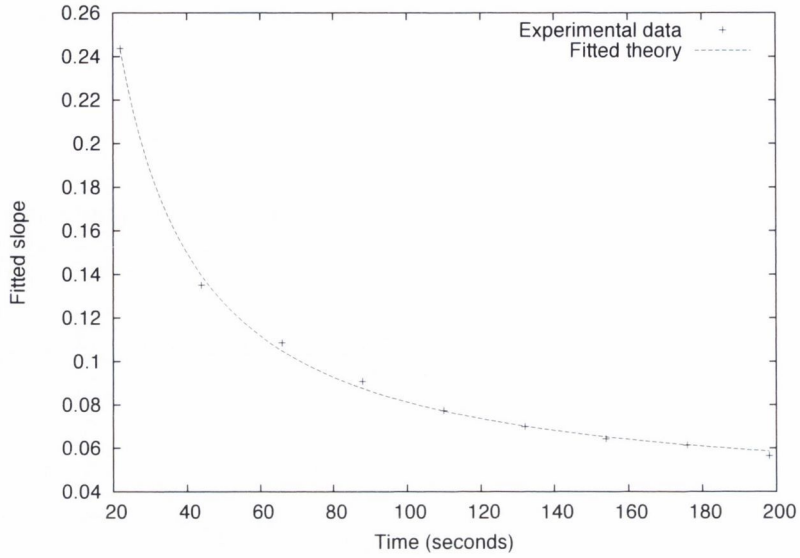

Figure 2.6: For every measurement time t in our experimental data, we can numerically compute a linear slope of the liquid fraction. We then fit Equation 2.9 to these numerical slopes, allowing us to determine t_a and — via c_1 — V_b.

From visual inspection of Figures 2.7 and 2.8, we can see that our recreated curves match the experimental data very closely. We also have a second measure of the goodness of our recreation available — the bubble volume V_b.

From our fits of Equation 2.9, we find the value $V_b = 8.4 \pm 0.7\,\mathrm{mm}^{-3}$. We were also provided with measurements of the average lengths of the Plateau borders on the walls of the tube containing the foam L_{PBW}. After rescaling these measurements for edge effects [33], we arrive at a value for the length of a Plateau border inside the bulk foam:

$$L_{PB} = \frac{L_{PBW}}{1.2}. \tag{2.10}$$

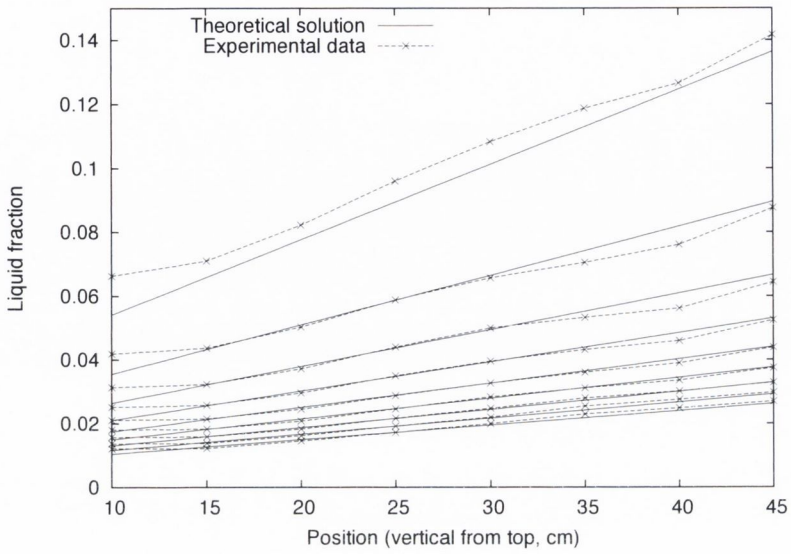

Figure 2.7: For much of the running time of the experiment, our recreation agrees very closely with experimental data. The theoretical curves are calculated from Equation 2.8, with parameters extracted from fits as discussed.

We must next relate L_{PB} to bubble volume V_b. We do this by approximating the sample foam with a Kelvin foam. The volume of a bubble in a Kelvin foam (by geometric considerations) is given by

$$V_b(L_{PB}) = 8\sqrt{\pi}L_{PB}^3. \tag{2.11}$$

For the measurements of L_{PB} provided with the experimental data, this leads to a value of $V_b = 8.2 \pm 0.8\,\mathrm{mm}^{-3}$, in agreement with the value found from our fits. This agreement between our linear FDE and experimental data confirms the findings of Carey and Stubenrauch [32] — that the foams used in their experiments

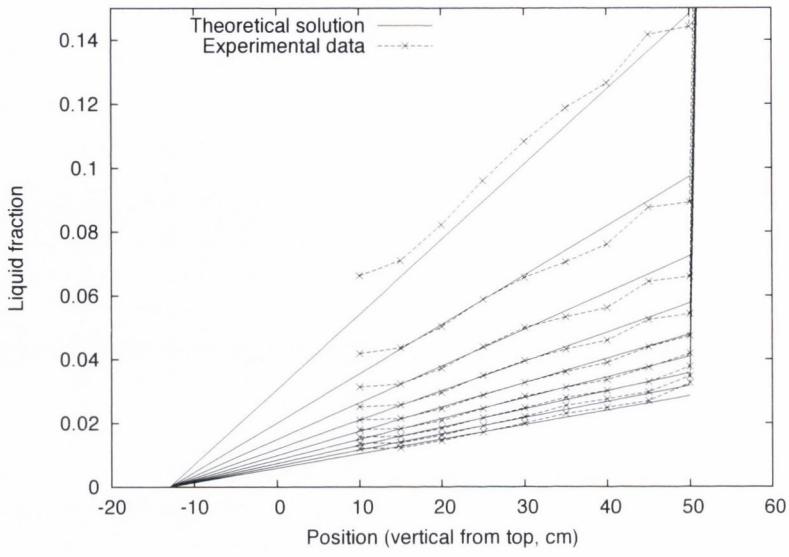

Figure 2.8: After calculating the various fit parameters, we are able to recreate the original experimental data from Equation 2.8, as it now has no free parameters for $\phi(x,t)$. The figure shows the full solution, including the finite offset $x_a = -0.12 \pm 0.01\,\text{cm}$. Good agreement is seen between the original experimental data (dashed lines) and the recreated solution (solid lines).

are well-described using channel-dominated drainage theory, exhibiting Poiseuille-like flow.

It is hopefully clear from this Section that, even with a simplified drainage model, we can still arrive at useful and valid comparisons to experiment. This is a recurring theme when working with drainage theory, and will be seen again in our work on foam fractionation (Chapter 3) and analysis of metal foams (Chapter 4).

Chapter 3

Foam Fractionation

3.1 Introduction to foam fractionation

Foam fractionation is the process in which a foam rises in a column and overflows at the top. The liquid collected from the overflowing foam, when it is collapsed, is relatively richer in the surface-active components of the liquid that was used to generate the foam. This process is of widespread practical importance in chemical engineering and biotechnology [34].

A resurgent mining industry, coupled with novel applications to the study of biological systems [35–37] (such as protein-stabilised foams), has lead to a greater need for a solid theoretical understanding of the underlying physics and chemistry of fractionation. While the theory behind the process has been studied in the literature since at least the 1960s (the work of Lemlich [38], for example, contains fairly complete descriptions of the various industrial processes and makes steps towards mathematical modelling), it has enjoyed something of a renaissance in

recent years. Major contributions with applications to the present work have come from Jameson (and collaborators) [39] and Stevenson (and collaborators) [40–43], both from within the fields of chemical and process engineering.

Also relevant to the present work, an avenue of research based on foam drainage theory and the FDE has been undertaken by Neethling et al. [44]. They presented results for a single fractionation column with overflow — building up a model from the channel-dominated FDE — and presented numerical and experimental results which confirmed the key points of their analysis. This approach has significant merit, as there is a large body of research on foam drainage which may be applicable to fractionation. In this way, we can see a potential opportunity to bridge disparate research efforts by physicists and engineers, and move the understanding of fractionation forward.

Attempts to derive a firm analytical model for fractionation processes have often been hampered by difficulties in describing the theoretical foam overflow reliably. Capturing the overflow requires consideration of column geometry, foam drainage and coarsening, rupture of bubbles, and the rheology of the overflowing foam itself. Reducing such complex behaviour to more mathematically-tractable boundary conditions is one of the main results of this chapter. It is therefore desirable to explore a model system which is representative of the fractionation process, and which involves boundary conditions that are realistic while being less challenging to theory than the more typical overflow from an open column.

Once we have such a model in place, we can move on to understanding fractionation in greater detail, which will aid the process of maximising the efficiency of industrial designs. As the process is used on the industrial scale, reducing inefficiency at the design stage and during operation may allow significant im-

provements to output and may reduce waste of materials and energy (a pressing concern in modern times).

3.2 A model system for foam fractionation

The model we chose for study is an inverted U-tube system, shown in schematic form in Figure 3.1. An inverted U-shaped tube connects two liquid reservoirs. Foam is generated by a gas sparger in the left-hand reservoir, rises through the left-hand (inflow) leg and through the U-bend, and flows downwards in the right-hand leg into the right-hand collection reservoir[1]. As the foam is in contact with a liquid surface at both ends of the tube, we have well-defined boundary conditions. This allows us to sidestep the challenge of mathematically describing an overflowing foam, and opens the problem of continuous foam fractionation to mathematical examination. U-tube systems are also amenable for experimental work (used, for example, by Martin et al. [45]). The U-tube makes it easier to collect outflowing foam and make accurate measurements of the foam. This will be further detailed in Section 3.2.5, which describes our experiments on a real U-tube.

We assume that there is a steady flow of both gas and liquid from left to right, and that the gas flow rate is constant. The key question, therefore, is: *what is the liquid flow rate that is delivered?* This must vary with the gas flow rate and other physical and chemical parameters of the foam, such as bubble size, surface tension and viscosity.

[1] In a real fractionation column of this type, the left reservoir would hold the solution containing surface-active molecules and the right reservoir would contain a more concentrated solution (the concentration difference would depend on the column set-up). As will be explained, our model does not consider this concentration directly.

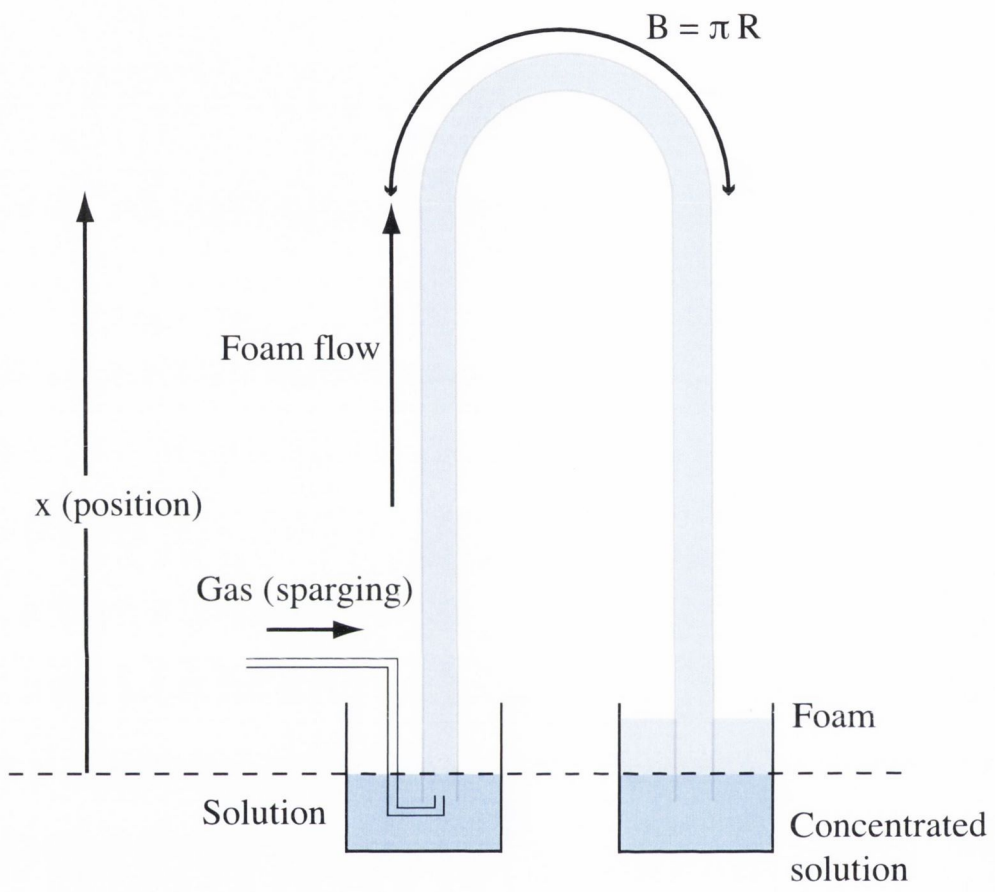

Figure 3.1: Schematic illustration of the inverted U-tube set-up for the study of foam fractionation. Gas is sparged into a surfactant solution reservoir at a constant rate, generating foam which flows through the tube. The foam preferentially carries the surface-active components of the solution, leading to an increase in concentration in the outflow reservoir. This mode of operation is termed "simple mode" [46] as there is no independent liquid feed.

A proportion of the surface-active molecules in the inflow reservoir become trapped at the film surfaces as the foam is generated. These molecules are carried through the tube with the moving foam and, hence, are delivered at a rate determined by the gas flow. However, the interstitial dilute liquid does not flow through the tube at the same rate (due to drainage through the foam). When considering the efficiency of a column, we may seek to ensure as many of the surface-active components are carried with the foam as possible, while minimising the delivery of the dilute solution. This will be discussed in greater detail in Section 3.3

We shall examine the behaviour of the U-tube using the steady-state version of the FDE introduced in Chapter 2.2. (A derivation of the full time-dependent FDE can be found in Appendix A.) A great advantage of the elementary FDE is that, with it, many problems may be treated *analytically* in a relatively straight-forward fashion. With a full analytical theory in place, we can begin to understand the process of fractionation in greater detail. Much of the analysis can also be extended to the more general case and, eventually, to other fractionation columns.

We will present numerical solutions which corroborate the findings of the analytic theory, and preliminary experiments to test it. We will also analyse the dependence of the results on the length of the two legs. We will derive a metric of performance for fractionation columns, and show how it may be used to maximise the efficiency of U-tube set-ups. Finally, we will outline how to extend these results to other types of fractionation column, with examples.

3.2.1 Basis of the theory

The steady-state form of the FDE relates local values of liquid flux J (volume flow rate per unit cross-sectional area) to liquid fraction ϕ, and is given by simply setting the time derivative of Equation 2.2 to zero, resulting in

$$\frac{\partial}{\partial x}\left(c_1\phi^2 - c_2\phi^{\frac{1}{2}}\frac{\partial\phi}{\partial x}\right) = \frac{\partial}{\partial x}(J) = 0, \tag{3.1}$$

where the quantity inside the parentheses is a local flow rate J and (as before) c_1 and c_2 are given by

$$c_1 = \frac{\rho g}{l_V \eta^*}, \tag{3.2}$$

$$c_2 = \frac{1}{2}\frac{C\gamma}{l_V^{1/2}\eta^*}. \tag{3.3}$$

In our model fractionation set-up we have a driving gas velocity V, which must be taken into account when considering the total flow rate. There is an additional flux term resulting from the transport of liquid through the U-tube simply due to the motion of the foam. This is given by the gas velocity multiplied by the local liquid fraction $V \times \phi$.

The gas velocity V is, more precisely, the result obtained by dividing the constant gas flux by the gas fraction $1 - \phi$ and, hence, is a function of position in the column. However, as the FDE is formulated for foams with a relatively low liquid fraction ($\phi \ll 1$), we may treat this velocity as constant and neglect the small variation arising due to changing liquid fraction. As we will see, this is a

fair approximation, as the variation of liquid fraction in the legs of the U-tube is limited.

The flow of gas and liquid will be treated as one-dimensional, i.e., we do not allow for any variation across the finite cross-section of the tube. Such variations are certainly detectable in experimental systems, but will be neglected here to allow the derivation of analytical results (and the numerical verification of those results).

In the following, x denotes the *upward* vertical coordinate for both the left (upward flow) and right (downward flow) legs, with $x = 0$ at the liquid surfaces and $x = L$ at the top (i.e., x refers to a height above the surface of the liquid reservoirs). We take both legs to be of equal length for simplicity of notation, however this is not required by the analysis. We will also denote the liquid fraction in each leg separately, by ϕ_l and ϕ_r respectively.

In the left-hand tube, both liquid and gas flow in the direction of increasing x. Our modified FDE thus takes the form

$$J = \phi_l(V - c_1\phi_l) - c_2\phi_l^{1/2}\frac{d\phi_l}{dx} \tag{3.4a}$$

$$\frac{d\phi_l}{dx} = -c_2^{-1}\phi_l^{-1/2}\left(c_1\phi_l^2 - \phi_l V + J\right), \tag{3.4b}$$

while, for the right-hand side — where both liquid flux and gas velocity now flow in the direction of decreasing x — we have

$$-J = \phi_r(-V - c_1\phi_r) - c_2\phi_r^{1/2}\frac{d\phi_r}{dx} \tag{3.5a}$$

$$\frac{d\phi_r}{dx} = -c_2^{-1}\phi_r^{-1/2}\left(c_1\phi_r^2 + \phi_r V - J\right). \tag{3.5b}$$

When describing foam fractionation, we will present results scaled by the constants c_1 and c_2 (introduced in Section 2.2). This allows meaningful comparison between foams that may have largely different physical and chemical characteristics, simply by calculating these constants and scaling appropriately. The reader may also apply our results to a system of interest in a similar manner. In this Chapter, we use the following (fairly typical) values for the parameters that make up c_1 and c_2: $\eta = 0.001\,\mathrm{Pa\,s}$, $\gamma = 0.05\,\mathrm{N\,m}$, $\rho = 1000\,\mathrm{kg\ m^{-3}}$, and $V_b \approx 4 \times 10^{-9}\,\mathrm{m^3}$, giving $c_1 \approx 3.2 \times 10^{-2}\,\mathrm{m\ s^{-1}}$ and $c_2 \approx 4.7 \times 10^{-5}\,\mathrm{m^2\ s^{-1}}$. This gives a value for $c_2/c_1 \approx 1.47 \times 10^{-3}\,\mathrm{m}$.

While our numerical results are presented in terms of these units, it can be helpful to have a feel for the sizes of the fractionation columns involved. Unless otherwise noted, the simulated columns have leg lengths between 10 cm and 1 m, and are driven with gas velocities between approximately 1 mm $\mathrm{s^{-1}}$ and 25 mm $\mathrm{s^{-1}}$. Experimental apparatus will be described in the appropriate sections.

When deriving an analytic theory, we neglect the effect of a finite bend, instead assuming that liquid fraction may be equated at the top of the two columns. This approximation will be examined by simulation in an appropriate regime of flow

parameters (see Section 3.2.4) by numerically integrating over the entire column, including the bend. A brief analysis of the expected error from this assumption can be found in Section C.1.

Keeping these approximations in mind, the boundary conditions for the U-tube model are therefore taken to be

$$\phi_l(L) = \phi_r(L) \tag{3.6}$$

and

$$\phi_l(0) = \phi_r(0) = \phi_c = 0.36, \tag{3.7}$$

where ϕ_c is, as before, the critical liquid fraction commonly taken for the liquid fraction at the liquid interface [5]. The key results are insensitive to this precise value.

3.2.2 Analysis of the limiting case: $L \to \infty$

We begin our analysis of the problem posed in the previous section by considering the limiting case of infinitely long legs, i.e., where $L \to \infty$. Working in such a limit will allow some simplifications to be made, allowing important limiting results to be derived.

We take the gas velocity V to be fixed, and take the liquid flux J to be variable. Determining the relationship between V and J — i.e., $J(V)$ — will be one of our first objectives. It is intuitively obvious that the flux J will be dependent on the leg length L, although we will first consider only the limiting infinite leg case.

We shall show that, in this limit, and with the above boundary conditions,

$$J \to J_0 = \frac{V^2}{4c_1}, \tag{3.8}$$

which is the value for which the expression in parentheses in Equation 3.4b has two coincident roots for ϕ_l.

The roots in question for Equation 3.4b are

$$\phi_{1,2} = \frac{V \pm \sqrt{V^2 - 4c_1 J}}{2c_1}, \tag{3.9}$$

while the corresponding roots for Equation 3.5b are

$$\phi_{3,4} = \frac{-V \pm \sqrt{V^2 + 4c_1 J}}{2c_1}. \tag{3.10}$$

All of these roots, when real, are significant for being constant-profile solutions. Since these do not fit the boundary conditions, such solutions are not used directly here. On the right-hand side, only ϕ_3 is positive and, therefore, ϕ_4 is largely irrelevant (as negative liquid fraction is not physically meaningful).

We integrate Equation 3.5b to obtain

$$L = -\frac{c_2}{c_1} \int_{\phi_r(0)}^{\phi_r(L)} \frac{\sqrt{\phi_r} d\phi_r}{(\phi_r - \phi_3)(\phi_r - \phi_4)}. \tag{3.11}$$

The integral in Equation 3.11 must diverge as $L \to \infty$, and this requires $\phi_r(L) \to \phi_3$. This further implies (from Equation 3.6) that $\phi_l(L) \to \phi_3$. In this way, the right leg sets an approximate boundary condition for consideration of the left-hand leg.

Again, we will have use for the integrated form (of Equation 3.4b),

$$L = -\frac{c_2}{c_1} \int_{\phi_l(0)}^{\phi_l(L)} \frac{\sqrt{\phi_l} d\phi_l}{(\phi_l - \phi_1)(\phi_l - \phi_2)}. \tag{3.12}$$

Consider the case $J < J_0$, for which the roots ϕ_1 and ϕ_2 are real. By the same argument as given above, we require $\phi_l(L) \to \phi_1$. But there is no finite value of J in this range for which $\phi_1 = \phi_3$, as required by Equation 3.6, hence no such solution is possible.

We now turn to the case $J > J_0$, for which ϕ_1 and ϕ_2 are complex. For any given J in this range, the denominator in Equation 3.12 has a minimum (finite) value and, hence, the integral in Equation 3.12 cannot diverge.

The remaining possibility is that $J \to J_0$ as $L \to \infty$. The integral

$$L = -\frac{c_2}{c_1} \int_{\phi_c}^{\phi_3} \frac{\sqrt{\phi_l} d\phi_l}{(\phi_l - \phi_1)^2} \tag{3.13}$$

is indeed divergent, as required. Thus, Equation 3.8 must hold in the limiting case.

All of this may be seen more clearly by examining the numerical solutions (see Section 3.2.4), but a formal derivation such as the above is desirable. That derivation becomes apparent when the nature of the approach to the limit of infinite L is analysed, finding the appropriate asymptotic form for $J(L)$ using the above integrals.

(Alternatively, there exist analytic solutions of Equation 3.12 and Equation 3.11. The full derivations are protracted and can be found in Appendix B.)

We now note a subtle feature of these solutions which may cause concern. For $J = J_0$, $\phi_l \to \phi_1 (= \phi_2)$ as $x \to \infty$. How can this be compatible with the boundary condition (Equation 3.6), since $\phi_1 \neq \phi_3$?

We may resolve this apparent paradox by noting that, for any finite large L, the liquid flux may be expressed by

$$J = J_0 + \epsilon^2, \tag{3.14}$$

where ϵ is small and results from the effects of finite leg lengths.

There is only an *apparent* asymptote at $\phi_1(J_0)$, eventually crossed by the solution, which then decreases to the required value, close to ϕ_3. Figure 3.2 illustrates this behaviour clearly using numerical solutions for the liquid fraction profile of the left leg. For $J < J_0$ this inflection does not exist, confirming that no solution can exist. The existence of the inflection was also discussed by Neethling et al. [44]. The basic $J = J_0$ condition has been identified in various forms by other recent authors (and there is also at least one much older statement — by Desai and Kumar [47])— on this same subject, but the effect of the finite leg sizes (contained in ϵ) has not yet been analysed. We will examine this leg dependence in Section 3.3.2.

For large L, ϕ is close to ϕ_3 in most of the right-hand tube and we may define the corresponding liquid velocity there as

$$v = J/\phi_3. \tag{3.15}$$

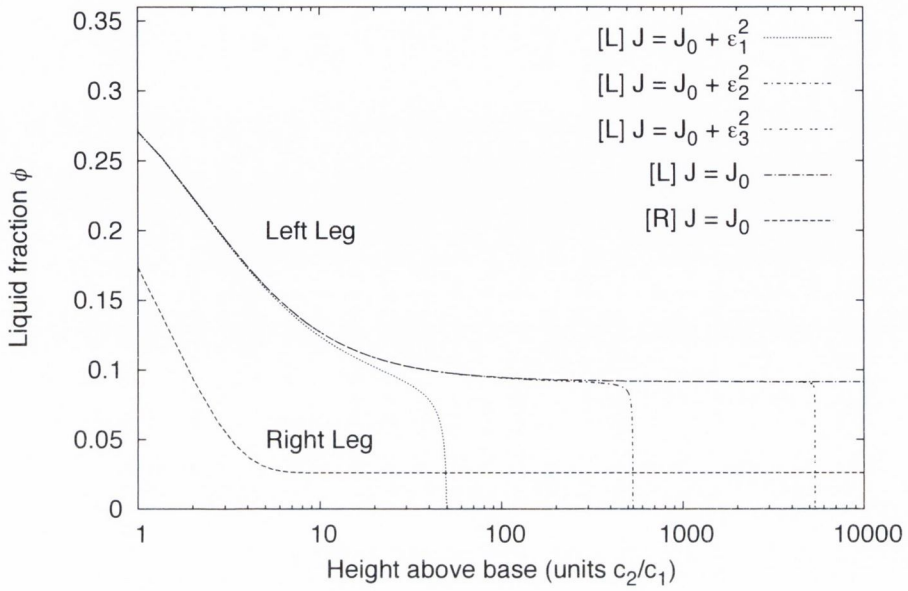

Figure 3.2: As $\epsilon \to 0$, the length of the left leg $L_l \to \infty$. The graphed solutions are for the left leg, except where indicated otherwise. The predicted apparent asymptotic behaviour is clear, especially in the smallest ϵ value solution. The curves here are solutions of Equation 3.4b for the left leg and Equation 3.5b for the right. Length is presented in units of c_2/c_1. The liquid fluxes are provided in terms of c_1 and are $J_0 \approx 8.4c_1 \times 10^{-3}$, $\epsilon_1 \approx 1.7c_1 \times 10^{-2}$, $\epsilon_2 \approx 1.7c_1 \times 10^{-3}$, and $\epsilon_3 \approx 1.7c_1 \times 10^{-4}$.

This enables us to arrive at the simple result

$$v = \left(2(\sqrt{2}-1)\right)^{-1} V \simeq 1.207V, \tag{3.16}$$

relating gas and liquid velocities in the right-hand leg.

This is a somewhat surprising result, in that the two velocities are related by a numerical constant. It is not inevitable on purely dimensional grounds, since the

theory contains a parameter (c_1) which has the dimension of a velocity. A similar argument holds for the left leg, where $J = v/\phi_1$. This leads to a liquid velocity of $v = V/2$. A similar result was presented by Neethling et al. [44] who derived it for an overflowing single leg column, taking the limit where the height of the overflowing foam section (i.e., how far the overflowing foam extends past the exit of the tube) tends to zero.

3.2.3 Generalisation of the infinite leg power law

We will take a step towards practical reality by generalising the power-law (which has often been empirically adjusted to describe particular surfactant systems [48]) at the heart of the equation.

We first modify Equation 3.4a by replacing the explicitly quadratic term with an exponent n (and changing the other terms as needed). The value of the exponent n is related to the prevailing dissipation mechanism for the flow of liquid through the foam, as discussed in Chapter 2. Our drainage model is based on channel-dominated drainage theory, leading to $n = 2$ [23]. The alternative dissipation mechanism of purely node-dominated drainage results in $n = 3/2$ [24]. In practice, n is often found from experiments and depends on the surfactant used. n has been found to take values varying from 1.92 to 2.29 for surfactants giving rise to more-or-less rigid interfaces (channel-dominated drainage) [48, 49], and 1.56 to 1.64 for surfactants with more-or-less mobile interfaces (node-dominated drainage) [24, 49].

The modified form of Equation 3.4a is

$$J = \phi_l V - b_1 \phi_l^n - b_2 \phi_l^{n-3/2} \frac{\partial \phi_l}{\partial x}, \tag{3.17}$$

where b_1 and b_2 are constants (equal to c_1 and c_2 respectively for $n = 2$). A similar modification may be made to the equations for the right leg. We begin by identifying constant profile solutions of the equation for the left-hand column, i.e., solutions for $\partial\phi/\partial x = 0$, which have the form

$$J = \phi_l V - b_1 \phi_l^n, \tag{3.18}$$

where b_1 is a constant containing physical parameters and $n > 1$ (note that $b_1 = c_1$ if $n = 2$, as it is in our model).

As before, we require coincident roots of this equation (for ϕ_l) as a condition for a matched solution in the limit $L \to \infty$. A full analytical formulation for the solution itself is not available in the general case, but is unnecessary in what follows.

The generalised results for J and v obtained from this condition are

$$J = b_1 (n-1) \left(\frac{V}{b_1 n} \right)^{\frac{n}{n-1}} \tag{3.19}$$

and

$$v = k(n) V, \tag{3.20}$$

where, again, k is a numerical constant dependent on the value of n.

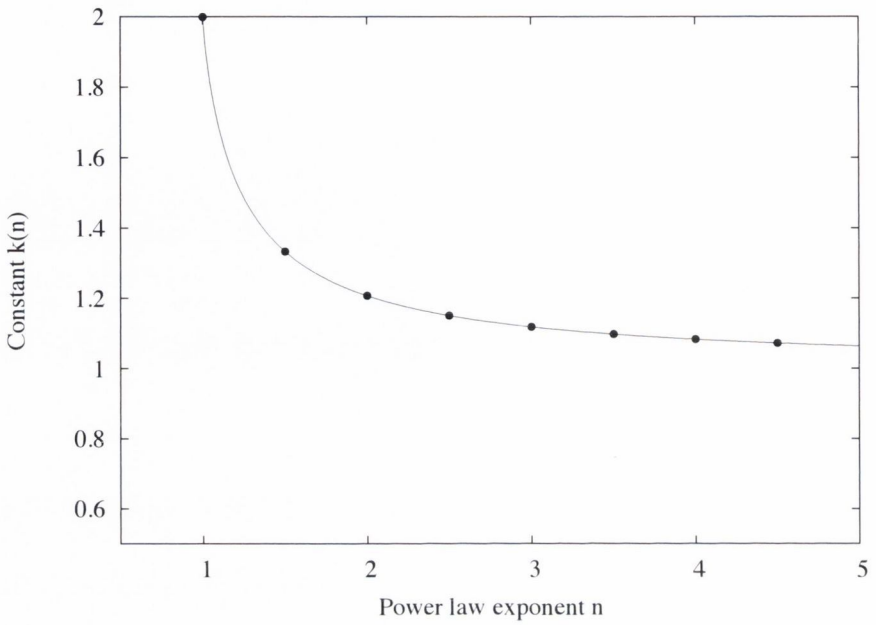

Figure 3.3: The dependence of liquid velocity v is proportional to the gas velocity V as $v = k(n)V$, where n is the exponent chosen for the power law at the heart of the drainage equation. The constant of proportionality $k(n)$ is a dimensionless number given by Equation 3.21. For the node-dominated drainage model (fully mobile interfaces) $n = 3/2$ [24]. For the channel-dominated drainage model (rigid interfaces), as used in the main body of this article, $n = 2$.

Thus, in the general case, the quadratic form for $J(V)$ is lost but v remains proportional to V. The constant of proportionality $k(n)$ is given by

$$k(n) = \frac{1}{d(n)}(n-1)\left(\frac{1}{n}\right)^{\frac{n}{n-1}}, \tag{3.21}$$

where the constant $d(n)$ is the real positive root of

$$d^n + d - (n-1)\left(\frac{1}{n}\right)^{\frac{n}{n-1}} = 0. \tag{3.22}$$

The form of $k(n)$ can be seen in Figure 3.3.

3.2.4 Numerical illustration

In order to validate and illustrate the analytical results discussed above, we will compare them with numerical simulations.

The Foam Drainage Equation (FDE) in its appropriate form is now solved for the entire U-tube, including a finite semicircular bend (a case for which there is no analytical equivalent).

The U-tube can then be thought of as a one-dimensional system, with the relevant component of gravity acting downwards in the left (input) leg of length L, upwards in the right leg (also of length L) and varying in the bend of length B. We thus write the (stationary) drainage equation for liquid fraction ϕ as a function of the new position variable z:

$$J = \phi(V - c_1\hat{g}(z)\phi) - c_2\phi^{1/2}\frac{d\phi}{dz}. \tag{3.23}$$

The function $\hat{g}(z)$ represents the variation of gravity and is defined piecewise as

$$\hat{g}(z) = \begin{cases} +1 & \text{if } 0 \leq z < L \\ -\sin\left(\pi\frac{z-B/2-L}{B}\right) & \text{if } L \leq z < L+B \\ -1 & \text{if } L+B \leq z < 2L+B. \end{cases}$$

In more physical terms this one-dimensional model implies that the liquid fraction across a cross-section of the tube will be homogenous. However, in a real foam inhomogeneities will arise in the bend as gravity no longer acts parallel to the flow direction (indeed, at the top of the bend gravity will be *perpendicular* to the flow). This can lead to the formation of a liquid boundary layer at the bottom of the bend walls, and this "hold-up" of liquid will cause a reduction in the liquid fraction in the right/outflow leg when compared to theoretical predictions, with the size of the discrepancy dependent primarily on the geometry of the bend section (i.e., how much liquid can pool on the bend surface). Modeling the effects of this non-uniformity will not be undertaken in this work.

The boundary conditions are set as before — i.e., both ends of the tube are in contact with a liquid reservoir — $\phi(z = 0) = \phi(z = 2L + B) = \phi_0 = 0.36$.

We require pairs of (V, J) that lead to a liquid profile consistent with these boundary conditions. Fixing V and integrating from left to right, starting from $\phi_0 = 0.36$, we use standard fitting techniques to determine the value of J for which the right-hand boundary condition is satisfied as well. This fitting of J is carried out using the MIGRAD minimiser from CERN's MINUIT software [50]. For more information on this software, see Appendix D.3. The integration is performed using Heun's method (explicit improved Euler method) [51]. This method is simple to implement and allowed rapid iteration on the numerical models which allowed more complete exploration of the problem space. Results from these integrations were tested against solutions calculated using Mathematica to ensure their validity.

In this way, we find the valid pairs of (V, J) for a given U-tube setup (e.g., leg length, bend radius, physical parameters of the surfactant solution). Results from these simulations are presented in Figures 3.4, 3.5 and 3.6.

Figure 3.4 shows a numerical computation of a full liquid profile for a U-tube system with a ratio of bend to leg length of 5/8, i.e., very similar to that used in some of our experiments (see Section 3.2.5). Note that the profile includes a full treatment of the bend, and that the bend and both legs have finite length. The analytic constant profile solutions for the left and right legs (Equations B.3 and B.5 respectively) are also plotted, highlighting the key difference in the left leg — the presence of an inflection point.

Figures 3.5 and 3.6 show, respectively, the variation of the liquid flux J with the gas velocity V and the variation of the liquid velocity v with the gas velocity V, for a U-tube system with ratio of bend length to leg length of 1/4. Despite the finite system dimensions in the simulations, the analytical predictions made by Equations 3.8 and 3.16 for the limit of infinite legs and zero bend radius are found to be in excellent agreement. Section C.1 gives a quantitative estimate of the effect of finite bend radius.

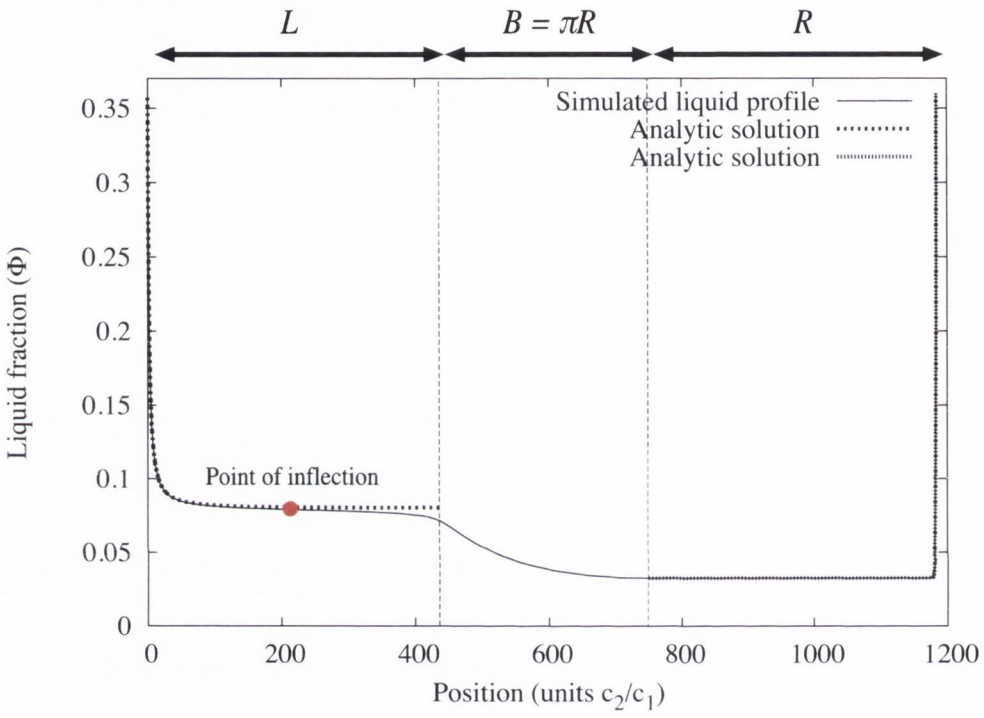

Figure 3.4: A numerical computation of a liquid profile for a U-tube system with bend to leg length ratio (5/8) very similar to that used in our experiments (see Section 3.2.5). Note that the profile includes a full treatment of the bend, and that the bend and both legs have finite length. The analytic constant-profile solutions for the left and right legs (Equations B.2 and B.5, respectively) are also plotted, highlighting the key difference in the left leg due to finite leg length — the presence of an inflection point.

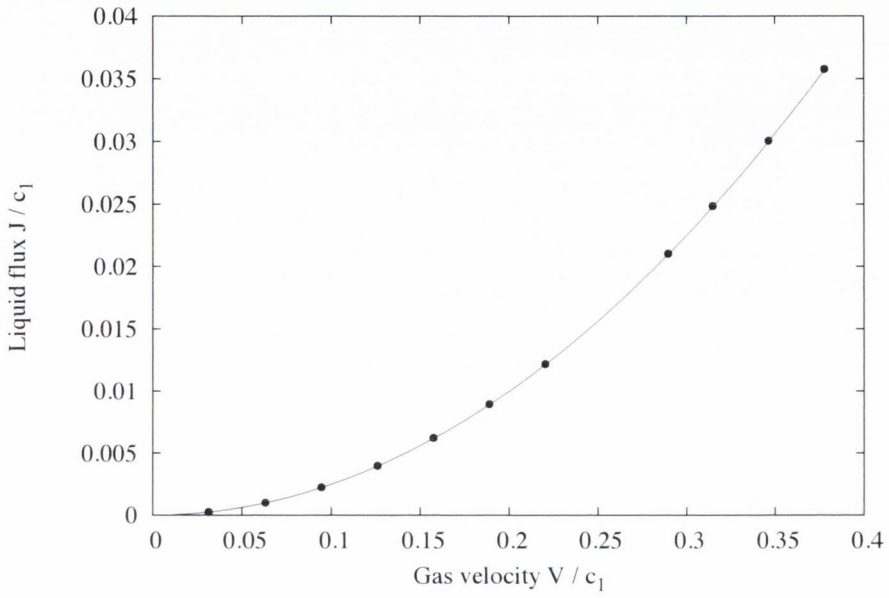

Figure 3.5: The analytic prediction given in Equation 3.8 for the relationship between liquid flux and gas velocity — $J = V^2/4c_1$ (solid line) — shows excellent agreement with values calculated from numerical solutions of Equations 3.4 and 3.5 (points). The method used to calculate these values is described in Section 3.2.4. Note that the analytical prediction is made for the limit of infinite leg length and zero bend length, while the simulations carried out used a tube with ratio of bend length to leg length of 1/4 (with leg length $L \approx 14\frac{c_2}{c_1}$).

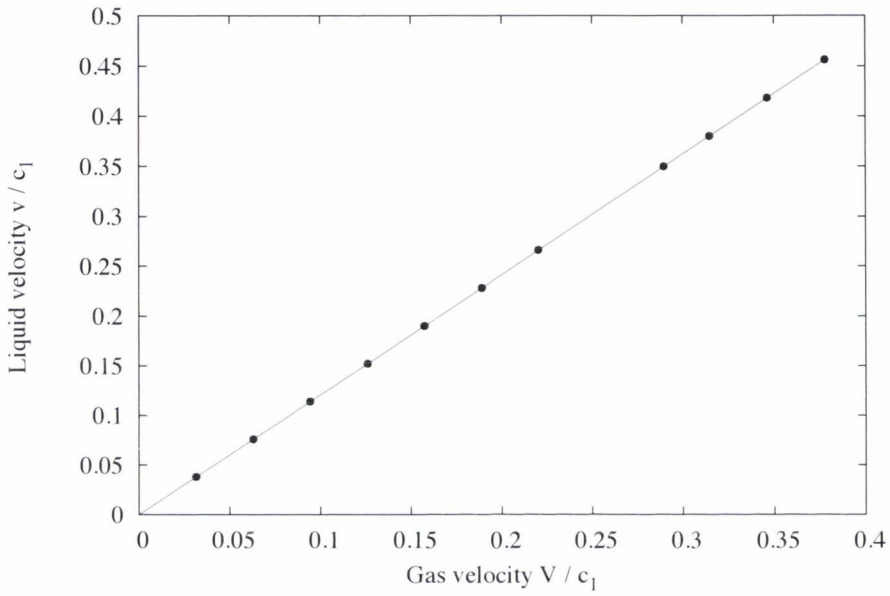

Figure 3.6: Equation 3.16 predicts a linear dependence of liquid velocity v on gas velocity V. As in Figure 3.5, simulation results (points) and analytic predictions (solid line) match extremely well. Note that the analytical prediction is made for the limit of infinite leg length and zero bend length, while the simulations carried out used a tube with ratio of bend length to leg length of 1/4 (with leg length $L \approx 14\frac{c_2}{c_1}$).

3.2.5 Experiments

(The author would like to thank Arthur Marguerite and Aaron Meagher for experimental support for this section).

Experiments were undertaken to test some of the key predictions made by the theory described above, which can be summarised as follows:

1. The ratio of the liquid fractions in the legs (measured sufficiently far from the liquid reservoirs) is approximately constant, and given by $\phi_1/\phi_3 = 1/(\sqrt{2} - 1) \approx 2.4142$ for rigid interfaces (by substituting Equation 3.8 into Equations 3.9 and 3.10) and by a different constant in other cases.

2. Equation 3.19 predicts that the dependence of liquid flux J on gas velocity V is a power law. Again the power law exponent n is dependent on the surfactant used (i.e., if the foam has mobile or rigid interfaces).

3. The dependence of the liquid velocity v on the gas velocity V is predicted by Equation 3.20 to be linear, with slope dependent on n.

The design of the experiments allowed us to check all three predictions. U-tube setups of the type shown in Figure 3.1 were assembled, with internal tube diameters of 5.8 mm and 15.7 mm. The lengths of the tube legs used were between 0.4 m and 0.64 m (for a total system length of 1.0 m to 1.7 m).

Foams were produced from aqueous solutions of sodium dodecyl sulfate (SDS) and Fairy Liquid (a commercial detergent), with concentrations above the critical micelle concentration (CMC). As SDS solutions are often unstable in light (releasing dodecanol into solution, which in turn leads to changes in the surface

mobility), fresh batches of the surfactant were produced regularly to minimise this effect. For the SDS experiments presented here, the solution was freshly prepared every other day and the experiments were carried out as close to the preparation time as possible to ensure consistency between runs.

Gas was blown through a ceramic filter, resulting in a polydisperse foam flowing through the tube (average bubble diameter approximately 1.0 mm). Once the foam had filled the entire tube, and the gas velocity had reached a steady state, experimental measurements were taken. For the surfactant mix used in our experiments, the foam parameters were as follows: $\eta = 0.001\,\mathrm{Pa\,s}$, $\gamma = 0.032\,\mathrm{N\,m}$, $\rho = 1000\,\mathrm{kg\ m^{-3}}$, and $V_b \approx 5.4 \times 10^{-10}\,\mathrm{m^3}$. For these values, we get $c_1 \approx 8 \times 10^{-4}\,\mathrm{m\ s^{-1}}$ and $c_2 \approx 1.5 \times 10^{-5}\,\mathrm{m^2\ s^{-1}}$.

Our analytical model of fractionation does not consider the effect of variations in bubble volume in space or time. In real-world foams, bubble volumes will change due to coarsening and coalescence (although the effect of coarsening can be slowed using non-diffusing gases such as perfluorohexane [14]), and this variation may account for at least some of the discrepancies observed between preliminary experiments and our model. Measurements taken during our experiments suggest a variation in bubble size of up to $1.2V_b$ in the worst case (i.e., the lowest gas velocity and hence the highest residence time spent by bubbles in the U-tube). Higher gas velocities reduce this time, and therefore lessen the effect of coarsening. No ruptures were observed throughout the experiments.

Gas velocity was measured by visually tracking individual bubbles in the foam. Liquid velocity was measured by adding fluorescein (a fluorescent dye) to the surfactant solution in the left reservoir (see Figure 3.1) and tracking the moving front using UV lighting. Liquid flux was measured by collecting the outflowing

foam in a beaker and measuring the mass of liquid collected over time to infer a liquid volume flow rate Q. The liquid flux is then simply $J = Q/A$ where A is the cross-sectional area of the tube. Liquid fraction was estimated (to within a constant) from the thickness d_{PB} of a Plateau border at the tube surface. Liquid fraction should be proportional to the square of this quantity, at least in the dry limit. We simply measured d_{PB} in both legs, and took the squared ratio of these values as an approximate measure of the ratio of the corresponding liquid fractions.

Results from our experimental measurements can be seen in Figures 3.7 and 3.8. Figure 3.7 shows the relationship between the gas velocity V and the liquid flux J. The data is very well described by a power-law fit to Equation 3.19, with exponent $\frac{n}{n-1} = 2.3 \pm 0.2$. This corresponds to a value of $n = 1.80 \pm 0.15$. Fairy Liquid has been associated with fairly rigid interfaces (i.e., $n \approx 2$) in previous foam drainage experiments [25, 28], so the theoretical expectation is approximately realised. It would be interesting to repeat these experiments in combination with other drainage experiments that more directly determine n.

Figure 3.8 shows the dependence of the liquid velocity v on the gas velocity V. Again, the general theoretical prediction ($v = k(n)V$) is verified, with a linear fit describing the data well. The fitted slope is $k = 1.23 \pm 0.07$. From Figure 3.3 we can see that this slope corresponds to a value of $n = 2.0 \pm 0.4$, consistent with the value from the $J(V)$ relation.

Measurements for the Plateau border thickness were taken approximately halfway up each tube leg (see Figure 3.4 for a numerical calculation of a full liquid fraction profile, noting the non-constant ϕ in the left leg) for an SDS foam. Multiple measurements were taken and averaged, giving $\phi_1/\phi_3 = 2.5 \pm 0.5$. The relatively large error in this measurement is larger than the variation in the left-leg liquid fraction

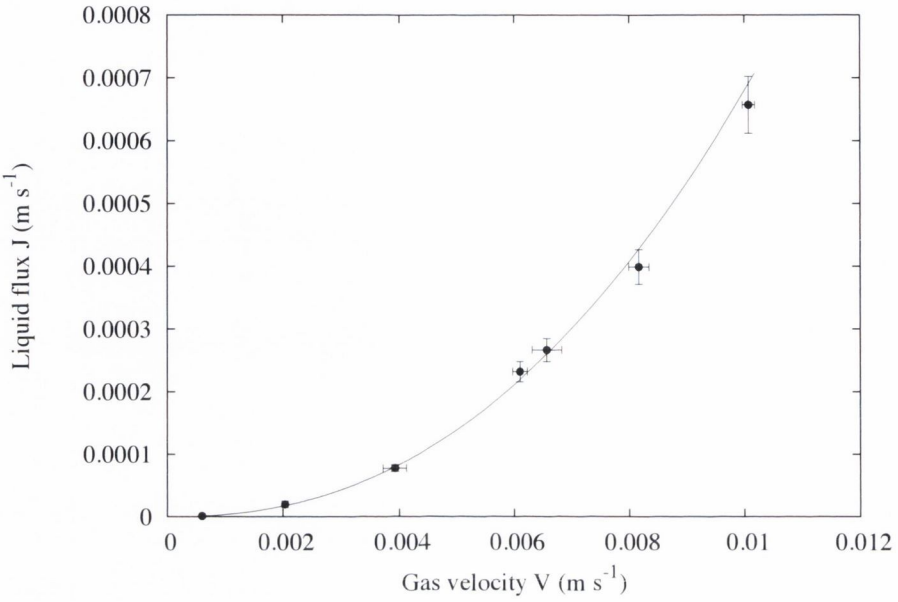

Figure 3.7: Experimentally determined variation of liquid flux J (in a U-tube with internal diameter 15.7 mm and leg length 0.64 m) as a function of gas velocity V. The foam was produced from an aqueous solution of the commercial detergent 'Fairy Liquid'. The solid line shows a fitted power law (as predicted by Equation 3.19) with exponent $\frac{n}{n-1} = 2.3 \pm 0.2$.

(Figure 3.4), thus the precise point at which the measurements were taken is of limited influence. The theoretical prediction for this value is $1/(\sqrt{2}-1) \approx 2.4142$ as outlined above, assuming $n = 2$.

In summary, we find general agreement between theory and experiment on points 1–3 above. However, the value of the power-law index n that was inferred was not in accord with expectations for the surfactant used (i.e., SDS-stabilised foams have been observed to have high surface mobility [52], and as such would tend to be better described by node-dominated drainage).

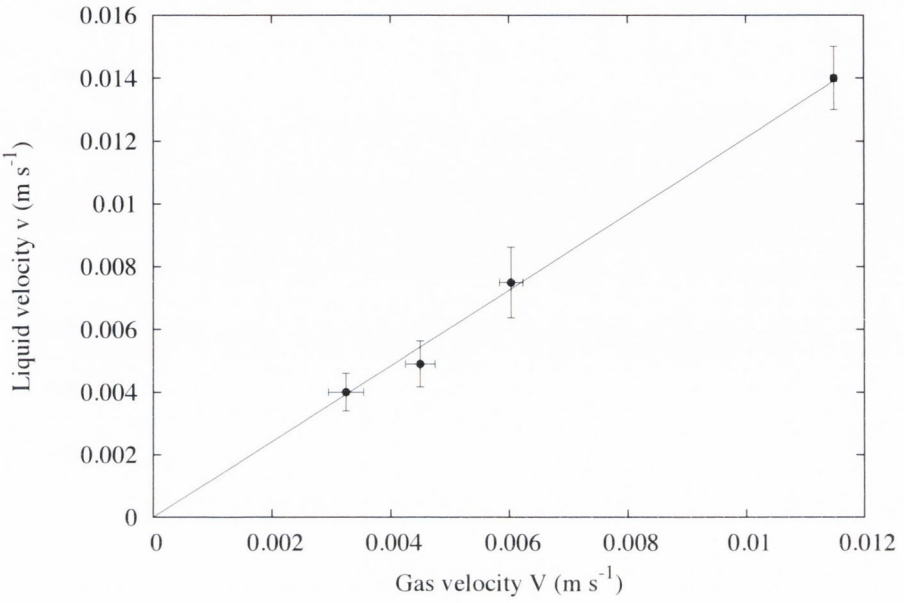

Figure 3.8: Experimentally determined variation of liquid velocity v (in a U-tube with internal diameter 15.7 mm and leg length 0.64 m) as a function of gas velocity V. The foam was produced from an aqueous solution of the commercial detergent 'Fairy Liquid'. The solid line shows a linear fit (as predicted by Equation 3.20), with slope 1.23 ± 0.07. This slope corresponds to a power-law exponent of $n = 2.0 \pm 0.4$ (see Figure 3.3).

3.3 Performance metrics for the U-tube fractionation column

Performance in a fractionation column can be considered in terms of enrichment (the ratio of concentration between the solution at the end of the column and the feed at the start) or recovery (the fraction of the desired product that is recovered from the outflowing foam).

As an illustrative example of how the analytic models outlined in previous sections may be applied to column performance, we will look at the recovery performance of the U-tube, which may be considered to be the increase in concentration between the input reservoir and the collected outflowing foam. As our model does not include chemical concentrations, we will use an approximation for the recovery.

Let us aim to increase the concentration of the surface-active components in the outflow. The amount of surface-active molecules that are carried through the column will be related to the available area of film surfaces and, therefore, to the gas velocity V (as increasing the gas velocity will cause more bubbles to move through the column and, hence, more surface-attached molecules). However, the foam has a finite liquid fraction and, thus, liquid that does not contain much of the components to be concentrated will also be carried through the column, reducing the outflow concentration. We can therefore construct a simple proxy for the recovery performance of the column — the ratio of V (representing the amount of surface-active components carried through the column) to J (representing the other components carried through):

$$\frac{V}{J(L)} = \frac{V}{J_0 + \epsilon(L)^2}. \tag{3.24}$$

Our use of V to represent the proportion of surface active components carried through the foam hinges on two assumptions (both of note in experimental systems). The bubbles must spend enough time in the liquid reservoir to reach equilibrium with the surfactant solution (i.e., adsorption processes reach an equilibrium). This will depend on the specific chemical make-up of the foam system under consideration and, due to the time-dependent nature of the process, cannot

easily be quantified in our existing model. We also assume that the surfactant concentration in the solution is not majorly impacted by the gas flow rate V (i.e., the depletion effect can be ignored). Again, this will depend on the precise chemistry of the solutions being used. If these assumptions are not true then the amount of surfactant per surface area will decrease as the gas velocity increases, leading to a more complicated relationship between V and the amount of surface-active components carried through the column (as the total amount will still increase, but at a lower rate as V increases).

In order to compute this metric, we will need to derive the dependence of flux on finite inflow leg length, $\epsilon(L)$. In our analytic model of fractionation, the behaviour of the inflow leg is defined in part by a top boundary condition, set in the finite case by the outflow (right) leg. Therefore, we first turn our attention to finite size effects in the right leg.

3.3.1 Limiting behaviour of liquid fraction in the right leg

In order to fix an upper boundary condition for the top of the left leg, we first consider the right leg. The equation for the variation of liquid fraction is

$$\frac{d\phi_r}{dx} = \frac{1}{c_2\phi_r^{1/2}}\left(J + \phi_r(-V - c_1\phi_r)\right). \tag{3.25}$$

Writing $J = J_0 + \epsilon^2$ (with $J_0 = V^2/4c_1$), we obtain

$$\frac{d\phi_r}{dx} = -\frac{c_1(\phi_r - \phi_3)(\phi_r - \phi_4) + \epsilon^2}{c_2\phi_r^{1/2}}. \tag{3.26}$$

Here, ϕ_3 and ϕ_4 represent the roots of the expression in parentheses in Equation 3.25, and are:

$$\phi_3 = \frac{-1+\sqrt{2}}{2c_1}V \tag{3.27}$$

$$\phi_4 = \frac{-1-\sqrt{2}}{2c_1}V \tag{3.28}$$

In the limit of infinite leg lengths, $\phi_r \to \phi_3$ as $x \to \infty$. For large enough leg length L_r, we may assume $\Delta\phi = (\phi_r - \phi_3)$ is small, as ϕ_r asymptotes to this value, and we can therefore approximate Equation 3.26 by

$$\frac{d\Delta\phi}{dx} = -\frac{c_1}{c_2}\frac{(\phi_3-\phi_4)}{\phi_3^{1/2}}\Delta\phi, \tag{3.29}$$

neglecting terms of order ϵ^2. Then

$$\frac{d\Delta\phi}{dx} = -\left(2\frac{\sqrt{c_1}}{c_2}\sqrt{1+\sqrt{2}}\,V^{1/2}\right)\Delta\phi. \tag{3.30}$$

Accordingly, $\Delta\phi$ decreases exponentially with height x and we can write a decay length as

$$L_d = \frac{c_2}{2\,\sqrt{c_1}\sqrt{1+\sqrt{2}}\,V^{1/2}}. \tag{3.31}$$

Therefore, by increasing leg length from L_d to $2L_d$ the liquid fraction is decreased by a factor $1/e$. The error in this length is of order ϵ^2. For $L_r \gg L_d$ this implies that, at the top of the leg,

$$\phi_r(L_r) - \phi_3 \propto \exp\left(-\frac{L_r}{L_d}\right) \tag{3.32}$$

and that, for such a case, it would be a good approximation to take $\phi_r = \phi_3$, therefore fixing the boundary condition for the top of the left leg at the same value that was found for the limit of infinite legs. A comparison of a full numerical solution and the simple exponential may be seen in Figure 3.9.

With an approach to defining upper boundary conditions for the finite-leg U-tube, we can turn our attention back to the left leg.

3.3.2 Finite size effects of the left leg

Our next step in calculating the performance metric is to determine $\epsilon(L_l)$, i.e., to quantify the effect of *finite* length for the left leg of the inverted U-tube. As discussed in Section 3.3.1, the length of the right-hand (output) tube L_r has a relatively small effect on the boundary conditions of the U-tube above a certain threshold length, given by Equation 3.31. As such, provided L_r is set to a sufficiently large value, L_l dictates the nature of ϵ. The effect of finite length is to increase J from the minimum value J_0, as shown in Equation 3.33.

$$J(L_l) = J_0 + \epsilon(L_l)^2. \tag{3.33}$$

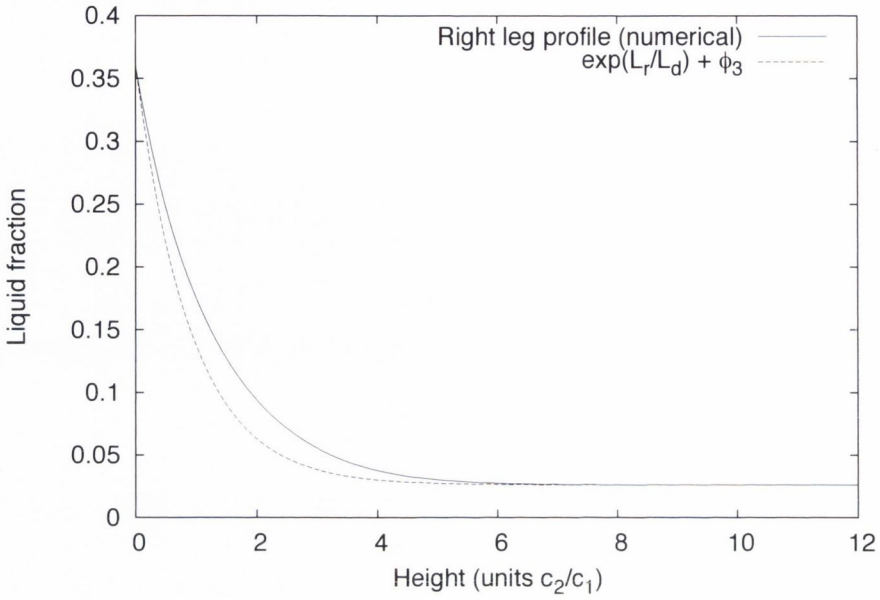

Figure 3.9: A numerical solution for the liquid profile in the right leg (solid line) is compared to the exponential model given in Equation 3.32 (dashed line). The exponentially decaying curve tracks the numerical solution well, and both curves tend to ϕ_3, as expected, over approximately the same distance.

This increase in J leads to a decrease in efficiency as more dilute solution is carried through the U-tube.

We can define an integral for the leg length based on Equation 3.4 (using the liquid flux given in Equation 3.33):

$$L_l = -\frac{c_2}{c_1} \int_{\phi_b}^{\phi_t} \frac{\sqrt{\phi_l}\, d\phi}{(\phi_l - \frac{V}{2c_1})^2 + \frac{\epsilon^2}{c_1}}. \tag{3.34}$$

After setting the bounds of integration to appropriate values and solving (with some assumptions, discussed in Appendix C.2), we arrive at an asymptotic expression for L_l:

$$L_l = \mu_1 V^{1/2} \epsilon^{-1} + \mu_2 + \mu_3 V^{-1/2}, \tag{3.35}$$

where

$$\begin{aligned} \mu_1 &= \frac{\pi}{\sqrt{2}} \frac{c_2}{c_1}, \\ \mu_2 &= -\frac{2}{\sqrt{\phi_c}} \frac{c_2}{c_1}, \\ \text{and } \mu_3 &= -\frac{2\sqrt{2}}{3} \left(\sqrt{2} - 1\right)^{3/2} \frac{c_2}{c_1^{1/2}}. \end{aligned}$$

A complete derivation of this result may be found in Appendix C.2. Rearranging the relation in terms of $\epsilon(L_l)$, we arrive at an equation describing the effect of left leg length on liquid flux:

$$\epsilon(L_l) = \frac{\mu_1 V^{1/2}}{L_l} \left(1 + \frac{\mu_2}{L_l} + \frac{\mu_3}{L_l} V^{-1/2}\right). \tag{3.36}$$

From these equations, we can see that $\epsilon(L_l) \propto 1/L_l$ (to first order) — increasing L_l will decrease $\epsilon(L_l)$, with $\epsilon(L_l) \to 0$ as $L_l \to \infty$. Equation 3.33 may be compared to numerical solutions. This is shown in Figure 3.10, with good agreement over a wide range of L_l.

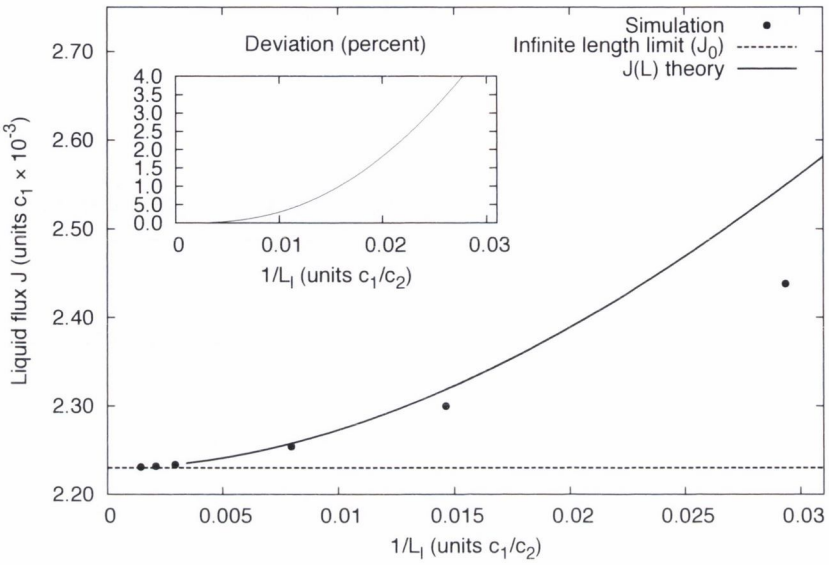

Figure 3.10: Liquid flux J increases as the left leg length L_l is decreased (as predicted by theory), thus decreasing the efficiency of the fractionation process. The analytic results for $J(L_l)$, given by Equation 3.33 (with $\epsilon(L_l)$, set by Equation 3.36), show good agreement for a wide range of L_l, with deviations from the numerical results only becoming significant for legs shorter than approximately $100c_2/c_1$. The inset shows the relative difference (in percentage) between numerical results and the theoretical prediction.

We may also explore the behaviour of $\epsilon(L_l)$ numerically. Fixing the gas velocity V, we set $J = J_0 + \epsilon_i^2$ for some ϵ_i and integrate the flux equation (Equation 3.4). We then take the point at which the liquid fraction $\phi = \phi_3$ to be the leg length $L_l(\epsilon_i)$, as this is the value of the liquid fraction at the top of the right leg (see Section 3.3.1 for the origin of ϕ_3 in this context).

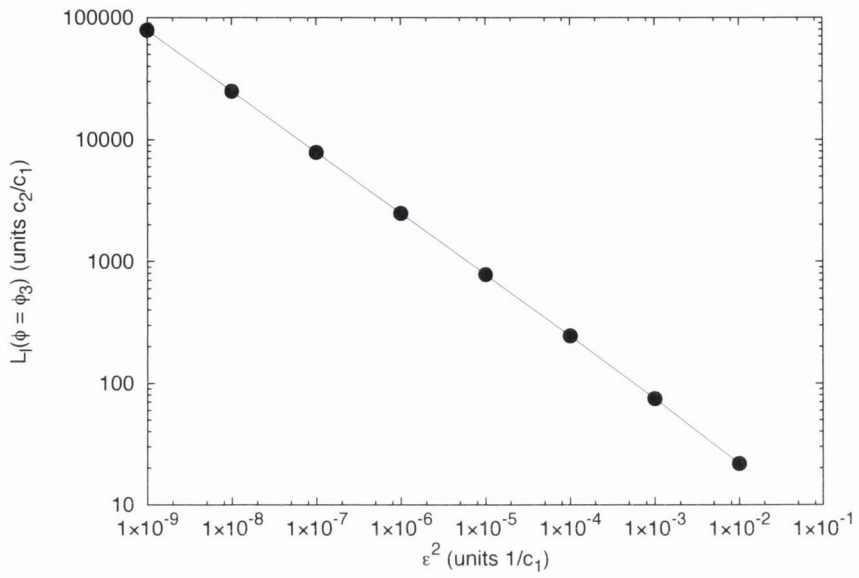

Figure 3.11: As $\epsilon \to 0$, the length of the left leg $L_l \to \infty$ (taking the length of the leg to be the height where $\phi = \phi_3$). The figure shows numerical results for $L(\epsilon^2)$ on a log-log plot. The slope of $-\frac{1}{2}$ corresponds to $L \propto \epsilon^{-1}$, as predicted by Equation 3.35 for finite values of V (in this case, $V = 0.12c_1$).

We can use this method to see how $L_l(\epsilon_i) \to \infty$ as $\epsilon_i \to 0$, shown in Figure 3.11. The figure shows (on a log-log plot) the shape of $L(\epsilon^2)$. As predicted by Equation 3.35, we observe a slope of $-\frac{1}{2}$, corresponding to $L \propto \epsilon^{-1}$.

Figure 3.2 shows the variation of the left leg liquid fraction profiles with ϵ, and that decreasing ϵ brings the finite leg solution closer to the infinite leg result, $J(L) = J_0$ (as predicted).

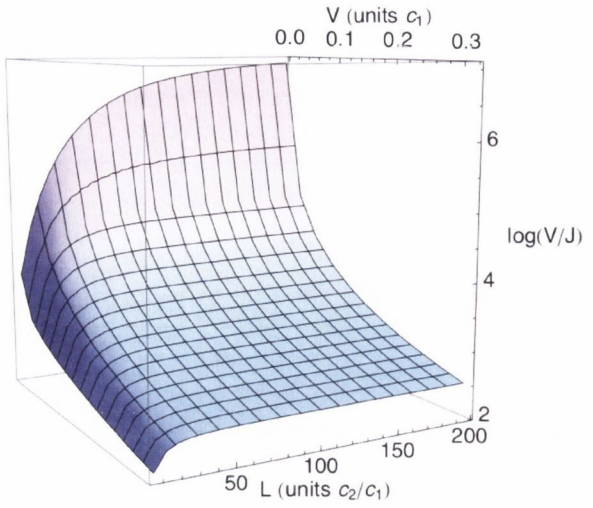

Figure 3.12: Our metric of efficiency as given by Equation 3.24 — V/J — is inversely proportional to gas velocity V (as $J \propto V^2$) and proportional to leg length L_l. Plotting with a logarithmic z-axis shows how efficiency can be dramatically increased by decreasing V.

3.3.3 Results for performance metrics

As discussed above, the performance of the U-tube fractionation column will depend on both the gas velocity and the length of the inflow leg L_l. Plotting Equation 3.24 (substituting Equations 3.33 and 3.36), and using the same physical parameters previously discussed, gives us Figure 3.12.

Figure 3.12 contains a lot of useful information about our metric of efficiency. Firstly, reducing gas velocity V *increases* efficiency. Secondly, for any given V, reducing L_l can lead to large performance drops. This can be seen more clearly in Figure 3.13.

These figures allow us to make the following recommendations for fractionation column operation: firstly, the gas velocity V should be reduced as much as possible (taking into account desired output rates and physical limitations of the foam);

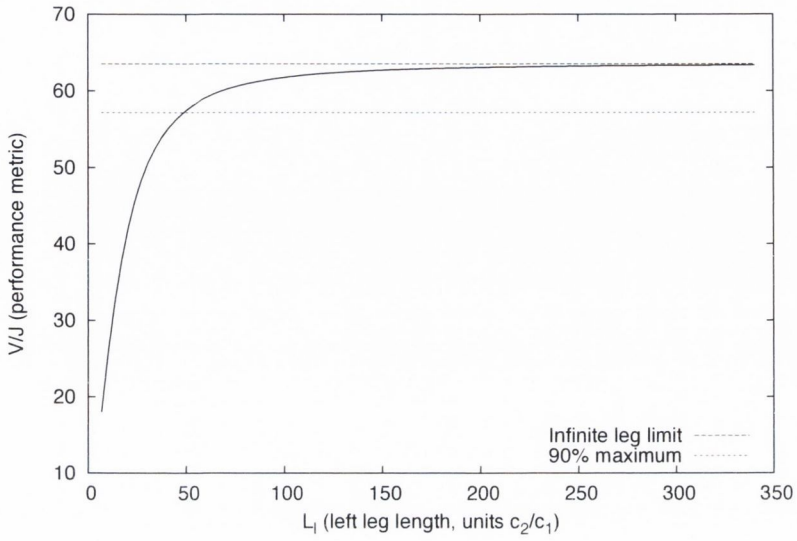

Figure 3.13: Fixing V lets us see the dramatic effect varying L_l can have on performance. The maximum performance occurs in the infinite leg limit (where $J = J_0$), shown along with a line indicating 90% of theoretical maximum performance. Reducing the leg length below approximately $100c_2/c_1$ leads to a drastic drop in performance from the theoretical maximum.

and, secondly, the length of the inflow leg L_l should be chosen carefully to ensure that operation is (for example) in the 95% regime or better. There may of course exist physical limitations on gas velocity and column size in real fractionation columns.

3.4 Alternate fractionation columns

3.4.1 Fractionation column components — the skimmer

While we have had success in our analysis of the U-tube, we have not yet generalised our approach to other types of fractionation columns. Any real industrial process will likely diverge from our idealised model and, as such, it is worthwhile to attempt to analyse a very different column in the same manner.

In certain fractionation applications, a further goal is to remove the surface-active components of the liquid phase as quickly as possible (for example, removing excess proteins from aquaria). In those cases, "skimmers" are often employed. These devices collapse and remove foam from the top of a straight column and, with the foam, liquid which is rich in surface-active molecules. A schematic showing a column with a skimmer can be seen in Figure 3.14.

We will now consider the case in which a skimmer provides the boundary condition at the top of a single vertical column. The skimmer removes foam, and with it liquid, at some rate $J_s = \phi_t V$, where V is gas velocity and ϕ_t is the liquid fraction at the top of the column. Conservation of mass then gives

$$J_s = \phi_t V = \phi_t v_l, \tag{3.37}$$

where J_s is the flux resulting from the action of the skimmer and v_l is the liquid velocity at the top of the column. $v_l = V$ at the top.

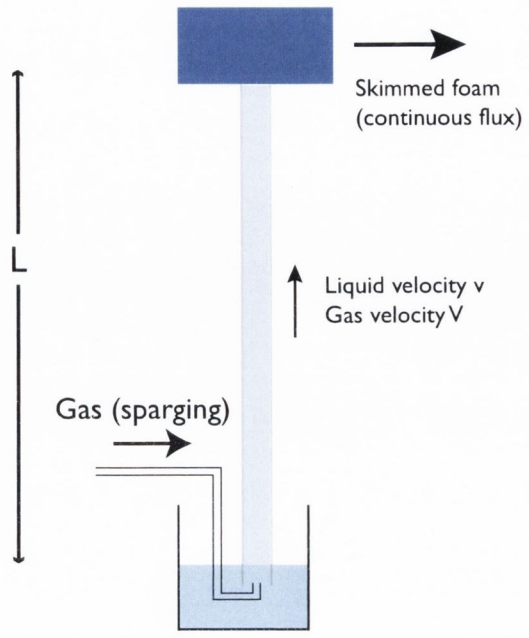

Figure 3.14: The skimmer removes liquid from the top of the column at a constant rate (by collapsing the foam). There is therefore a finite liquid flux J_s, which must equal $J(V)$ at the skimmer. This allows us to define a top boundary condition for the skimmer-variant column.

The appropriate boundary condition is therefore

$$\phi_t = \frac{J_s}{V}. \tag{3.38}$$

We will proceed to calculate J_s in the same manner as before. We first determine the infinite leg solution, then add corrections for the effect of finite leg length.

In the infinite leg limit, $J_s = J_0$ (see Appendix C.3). The arguments for $J = J_0$ in the left leg of the full U-tube model hold again here. Then, considering a finite leg length L, we will have a liquid flux of the form $J_s(L) = J_0 + \epsilon_s(L)^2$ as before (the form of $\epsilon_s(L)$ is different from the U-tube case, and will be outlined below).

ϕ_t can, therefore, be written as

$$\phi_t = \frac{J_0 + \epsilon_s^2(L)}{V} = \frac{V}{4c_1}\left(1 + \frac{\epsilon_s^2(L)}{J_0}\right). \tag{3.39}$$

In the limit of infinite leg length, the left leg of the U-tube and the skimmer column share the same solution (as we neglect the upper boundary conditions set by the bend and skimmer respectively). The asymptotic value for liquid fraction is therefore $\phi_1 = V/2c_1$ (as $J = J_0$ in the infinite limit). This implies that the liquid fraction at the skimmer ϕ_t is half the asymptotic value, as

$$\phi_t = \frac{V}{4c_1} = \frac{\phi_1}{2}. \tag{3.40}$$

This agrees with previous work by Neethling et al. [44], who noted this relation for overflowing single columns. Figure 3.15 shows a numerically solved liquid fraction profile for a single column with skimmer in which $\phi_t = \phi_1/2$ may be seen.

We can derive a formula for $L_l(V)$, following the same procedure outlined in Section 3.3.2 and Appendix C.2. We arrive at an expression with a similar form to that in Equation 3.35, as follows:

$$L_l = \mu_1 V^{1/2}\epsilon_s^{-1} + \mu_2 + \mu_4 V^{-1/2}, \tag{3.41}$$

where μ_1 and μ_2 are the same as in the U-tube, as only the top boundary condition has changed. The last term (μ_3 in the U-tube) does depend on the

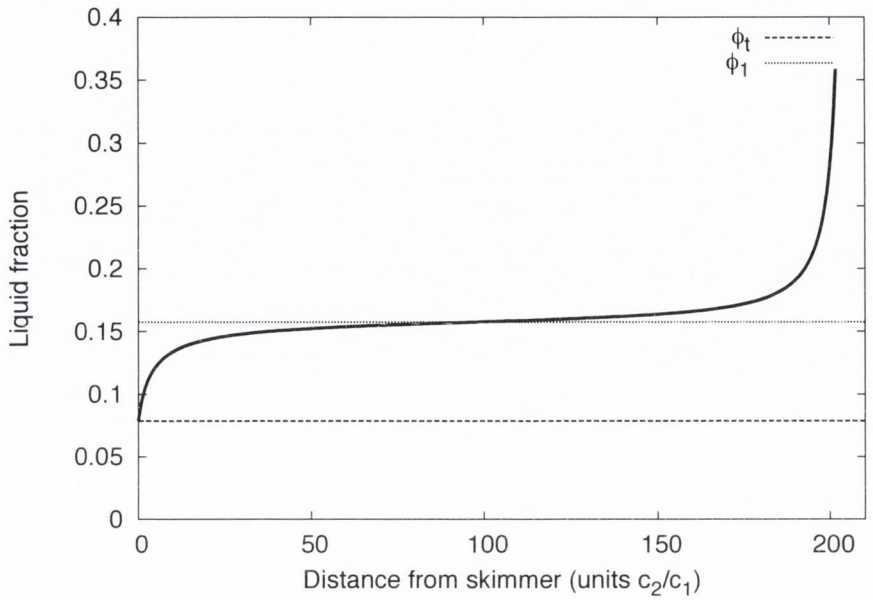

Figure 3.15: A numerical solution for a fractionation column including a skimmer (solid line). The boundary condition at the top of the column (i.e., the left-most side) where the foam contacts the skimmer is given by Equation 3.38. The bottom boundary condition requires the liquid fraction to go to $\phi_c = 0.36$ where the foam contacts the liquid reservoir. The relation $\phi_t = \phi_1/2$ can clearly be seen here (dashed lines). For the values of c_1 and c_2 used in our simulations (see Section 3.2.1), the length of the skimmer column is found to be 30 cm.

top boundary condition, which changes from $\phi_l(L) = \phi_3$ (for the full U-tube) to $\phi_l(L) = \phi_t$. It thus changes to μ_4, given by:

$$\mu_4 = -\frac{1}{3}\frac{c_2}{c_1^{1/2}}V^{5/2}. \tag{3.42}$$

A full derivation may be found in Appendix C.3. From here, we follow the same procedure as used for the U-tube — solving Equation 3.41 for ϵ_s — leading to Equation 3.43 as follows:

$$\epsilon_s(L_l) = \frac{\mu_1 V^{1/2}}{L_l}\left(1 + \frac{\mu_2}{L_l} + \frac{\mu_4}{L_l}V^{-1/2}\right). \tag{3.43}$$

We can then calculate a similar metric of efficiency for the skimmer, in this case V/J_s. Figure 3.16 shows numerical solutions for the skimmer column, along with theoretical predictions for $J_s(L)$ (following from Equation 3.41, as in the U-tube set-up). Good agreement can be seen over a wide range of leg lengths L.

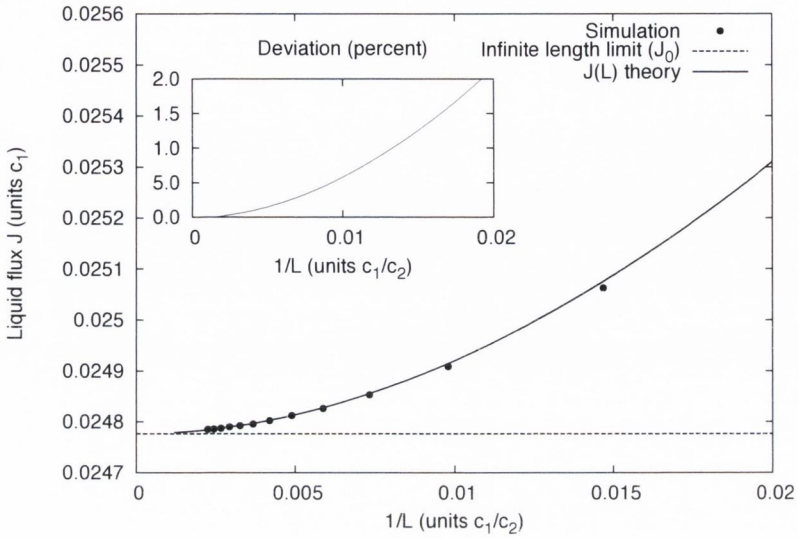

Figure 3.16: Analytic and numerical results for the skimmer system show good agreement over a wide range of leg lengths. Deviations from the numerical results become more significant as the legs become shorter (i.e., as the assumptions made in the derivation of the theory exert a larger influence; see Appendix C.2). The inset shows the relative difference (in percentage) between numerical results and the theoretical prediction.

3.4.2 Analysing fractionation modes using forced drainage

Throughout this work we have looked only at the so-called 'simple' mode of fractionation [38], with no liquid feed independent of the main solution reservoir. However, some fractionation columns incorporate a solution feed into the column (analogous to forced drainage experiments). Such designs aim to ensure that all the surface-active components fully adsorb on to the bubble surfaces, increasing

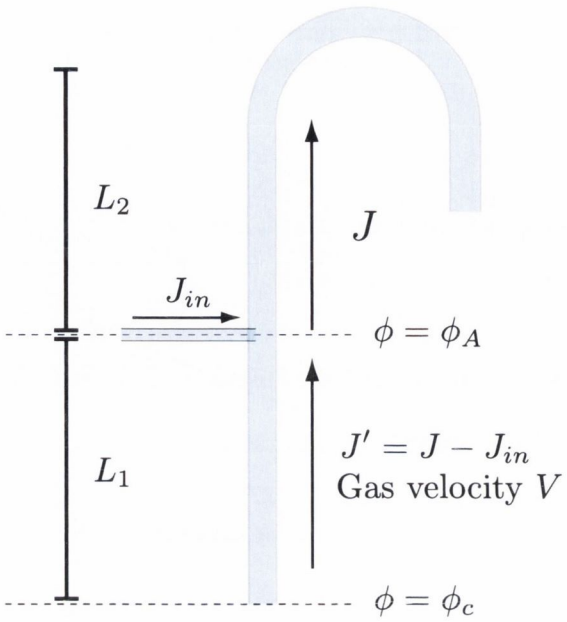

Figure 3.17: Modelling stripping and enriching mode requires the consideration of extra flux terms to represent liquid added through the elevated feed. Note that for large enough J_{in}, J' is negative. In real fractionation columns, there may be one or more such feeds and, in some cases, the output of the column is added back (in what is termed 'reflux'). Such modifications aim to improve the performance of the fractionation process.

the enrichment performance of the column. An example is shown in schematic form in Figure 3.17.

This may be analysed in a straightforward manner, building off the preceding results for the simple U-tube which apply above the point at which the additional liquid is introduced. We assume L_2 (the length of the leg segment above the liquid addition) is large enough to take $J = J_0$, as discussed in Section 3.3.2.

We may model the left (inflow) leg of such a column using numerical solutions based on Equation 3.4, with J replaced by $J(z)$:

$$\frac{d\phi_l}{dx} = \frac{1}{c_2\phi_l^{1/2}} \left(\phi_l(V - c_1\phi_l) - J(z)\right), \tag{3.44}$$

where

$$J(z) = \begin{cases} J - J_{in} & \text{if } 0 < z \leq L_1 \\ J & \text{if } z \geq L_1 \end{cases}$$

This differential equation can be solved numerically, resulting in liquid fraction profiles for the left leg. The right (outflow) leg solution remains identical to that of the simple U-tube. An example numerical solution is shown in Figure 3.18, with a solution for the same column leg without forced drainage for comparison.

The additional flux J_{in} can be chosen to increase the liquid fraction in the lower part of the leg (within limits of stability). Controlling the liquid fraction in this manner may allow the column adsorption efficiency to be improved. In order to gain the most from the additional liquid flow, the length L_1 must be sufficiently long to ensure complete adsorption. Large increases in enrichment are possible using forced drainage as reported by Martin et al. [45].

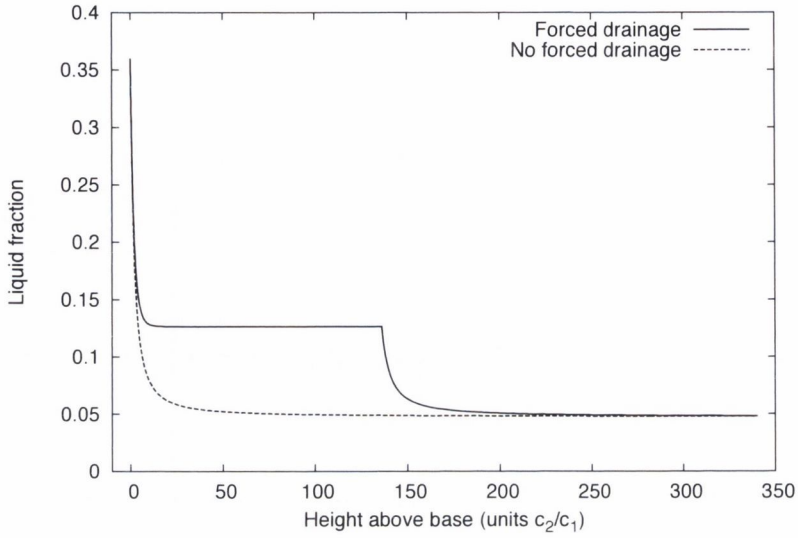

Figure 3.18: Numerical solutions for the left (inflow) leg clearly show the effect of forced drainage, with a dramatic increase in liquid fraction around the point where additional flow is added (in this case, $z \approx 140 c_2/c_1$). Two regimes are clearly visible, demarcated by the change in $J(z)$. In both curves, the base liquid flux is J_0 — the limiting value for the case of infinitely long legs.

3.5 Conclusions and Outlook

Despite widespread use of foam fractionation in several industrial and commercial applications [34], only limited attempts have been made to create complete analytic models of the process.

We have presented a complete model system for fractionation — that of an inverted U-tube. This model has proven itself to be a rich source of analytical results, both in limiting and finite cases. The limiting case of infinite leg lengths

provides a useful starting point for a thorough analysis, leading to several key results:

- the limiting value of the liquid flux J as $L \to \infty$ is quadratic in the gas flow velocity V ($J_0 = V^2/(4c_1)$);
- the ratio of liquid velocity v to gas velocity V is linear; and
- such results may be generalized to other forms of the foam drainage equation, giving other power laws for J (for example).

In all cases, numerical simulations were carried out and agreed closely with analytic predictions. Preliminary experimental tests were also conducted and predicted behaviours were observed (namely quadratic $J(V)$ and linear $v(V)$).

We also provided an alternate boundary condition in the form of the single column with skimmer. The analytic approach used to examine the U-tube is shown to be valid in the skimmer set-up, and numerical results again agree closely with predictions.

When building a model for processes like fractionation — as used in industry and chemical engineering — it is important to consider real-world uses. We have therefore attempted to keep the model and analysis as widely applicable as possible and to in mind the constraints that exist in industry. With that in mind, we analysed the effects of varying leg length on the operational efficiency of foam fractionation. Our results predict how the ϵ term in the liquid flux equation $J = J_0 + \epsilon^2$ varies with left leg length. As before, numerical simulations were carried out and agree closely with our analytical results. Real-world columns often include multiple liquid inflows to improve efficiency and performance [45],

and we have carried out preliminary work on integrating multiple flows into our model.

Our model may therefore allow the operators of such columns in both experimental and industrial contexts to make design and operation decisions to improve the efficiency of their set-ups, and provides an alternative theoretical foundation from which to analyse fractionation. It has the added benefit of being based on elementary drainage theory (the Foam Drainage Equation), which renders a large body of existing research available to researchers of fractionation.

Future work on our model should largely focus on increasing its applicability to real-world columns. Including chemical effects such as adsorption time may allow simple limits to be placed on column size (a length below which the efficiency of the column is reduced, as not all surface active molecules are carried through the foam but, instead, drain out of the foam). We also note that the current analysis and numerical simulations were carried out using a steady-state form of the FDE. Re-introducing time-dependent changes in the liquid fraction could allow us to examine the approach to the steady-state and any other time-dependent phenomena in the fractionation process.

Chapter 4

Drainage of liquid metal foams

4.1 Introduction to metal foams

In recent years, metal foams have become a subject of great interest in materials engineering [53], with promising applications arising in many areas, including vehicle design and advanced prosthetics. Large-scale production has, however, been hindered by an incomplete understanding of the processes by which metal foams stabilise and solidify, and how these processes influence the final structure of the foam. This is still a major challenge, as examining the molten system *in-situ* and verifying proposed mechanisms requires sophisticated experimental set-ups.

Two main mechanisms of film and foam stability have been proposed for metal foams. Some authors postulate that high bulk viscosity is essential [54], while others consider the influence of solid particles to be responsible [55–58]. These particles are theorised to partially wet the liquid surface and therefore accumulate on surfaces, building a kind of 'network' of interconnected particles, stabilising

the system. Unfortunately, these possible mechanisms are difficult to isolate from each other, as the presence of solid particles in the melt induces a higher viscosity. Detailed analyses of metal foams in the liquid (molten) state have yet to be carried out. The existing results are based on microstructure analysis of solidified samples, models, or simulations.

For such simulations and modelling, knowledge of melt parameters such as the liquid viscosity and surface tension is required. The standard approach has been to assume that the parameters taken from the bulk liquid matrix material are valid for the metal foam. However, the contribution of the foam structure itself must also be considered. Standard measurement techniques for viscosity and surface tension require the destruction of the sample structure and are therefore not generally useful. Compounding our difficulties, the values of surface tension and viscosity of metallic melts (e.g., aluminium) available in the literature are usually for very pure metallic melts, while the molten metal used in foaming experiments will contain impurities such as oxides.

Here, we outline a method that allows us to extract values for surface tension and viscosity from experimental data by iteratively solving the Foam Drainage Equation (which describes the flow of liquid in a foam), as presented in Chapter 2. Parabolic flights offer the unique possibility of performing experiments in varying gravity conditions, allowing the creation of a foam with a homogeneous liquid fraction (density profile) under microgravity, which is a well-defined initial state for our simulations. Brunke and Odenbach [59] made early steps towards considering liquid metal foams, showing qualitatively that numerical solutions of drainage theories captured the essence of an evolving metal foam.

4.2 Experiments on metal foams

The author would like to thank Francisco Garcia-Moreno and the rest of the group at the Institute of Applied Materials, Helmholtz Zentrum Berlin, for providing the experimental data used for this analysis as described below, and for many fruitful conversations about the experiments and data analysis techniques required.

As liquid metal foams are a challenging material to work with, we will first outline the apparatus and techniques used to contain and measure the evolving foam. The standard notation used to describe metal alloys is based on the composition of that alloy. For example, the alloy AlSi6Cu4 is composed of 6% Silicon, 4% Copper and, therefore, 90% Aluminium. The presence of any additives, such as stabilising particles or blowing agents, will be noted where applicable (e.g., AlSi9 + 0.6 wt.% TiH_2 is an alloy consisting of 91% Aluminium and 9% Silicon, with 0.6 % by weight of TiH_2 blowing agent).

4.2.1 Experimental apparatus and procedures

The X-ray transparent furnace used in microgravity experiments is shown in Figure 4.1. Developed and manufactured in cooperation with the Swedish Space Corporation [60], it can reach temperatures of up to 700 °C with high temperature homogeneity (±1 K). It allows precursor samples to be foamed to a maximum size of $20 \times 10 \times 20$ mm^3, expanding by a factor of 5 for a relative density (equivalent to liquid fraction) of 0.2.

Several different foamable precursor materials were used, falling into two categories defined by alloy and preparation method:

- AlSi6Cu4 + 0.6 wt.% of TiH_2, prepared by mixing the elemental powders with the blowing agent TiH_2, compacting the mix using cold isostatic compression and finally casting using the thixocasting method [61].

- AlSi9 + 0.6 wt.% of TiH_2 with 5, 10 and 20 vol.% SiC particles were prepared using the so-called FORMGRIP method [62].

The samples prepared were approximately $20 \times 10 \times 4$ mm^3 in size to fit into the foaming crucible. The AlSi6Cu4 samples were foamed at 650 °C and AlSi9 samples containing SiC particles at 700 °C.

The furnace was coupled with a micro-focus X-ray source and a flat panel detector, both provided by Hamamatsu Japan. The X-ray source has a 5 µm diameter spot, allowing relatively high resolution imaging. The flat-panel detector consisted of a 2240×2368 pixel array, with 50 µm pixel size. It could be operated at a maximum capture rate of 8 frames per second by sacrificing overall resolution (using 4x4 binning or squares of 16 pixels as pseudo-pixels, the effective sensitivity of the detector could be increased to allow higher frame rates). Each detector pixel contained image information from a sample area of 12.5×12.5 µm^2 for all the experiments (taking into account the 4-fold magnification).

This set-up allowed X-ray radioscopy of the foaming process *in-situ* [63], and is shown in schematic form in Figure 4.1.

4.2.2 Liquid fraction analysis

X-ray radioscopic imagery was captured throughout the flights, and images were analysed to obtain the variation of liquid fraction in the samples. Assuming that the density of a solid foam corresponds to the liquid fraction of the liquid foam,

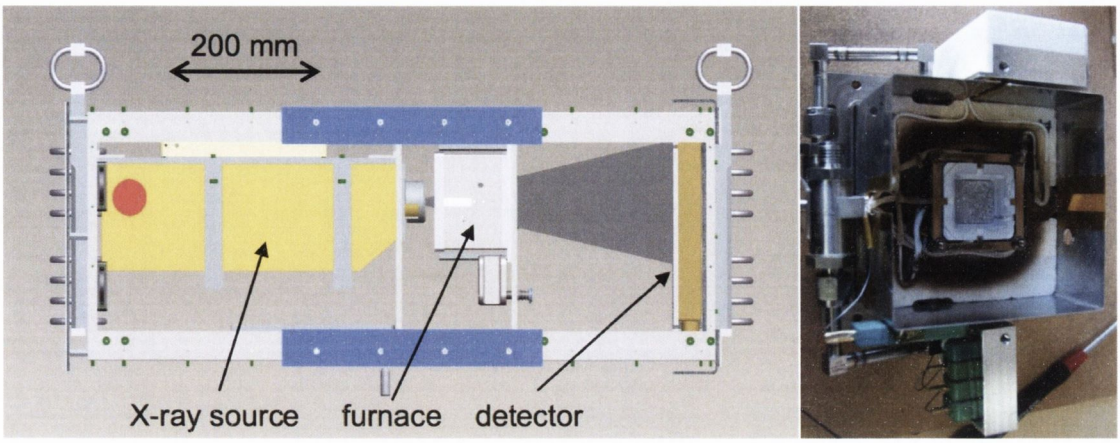

Figure 4.1: The X-ray radioscopy set-up used during the parabolic flights. On the left, a CAD schematic shows the micro-focus X-ray source, the foaming furnace and the detector. On the right, a photograph shows a foam sample inside the furnace. Images courtesy of Francisco Garcia-Moreno, Helmholtz Zentrum Berlin.

the analysis provides 2D liquid fraction distributions of the evolving foam ($\phi(x, z)$) by applying Beer-Lambert's attenuation law to the intensity $I(x, z)$ obtained from the X-ray images:

$$I(x, z) = I_0 \exp\left(-\mu\phi(x, z)\right), \tag{4.1}$$

where μ is the mass-specific absorption coefficient of the base alloy and I_0 the initial beam intensity. Strictly speaking, this law is in general only applicable for monochromatic X-rays due to the wavelength-dependent absorption coefficients of different materials. But it is applicable for polychromatic X-rays and one single material, as is the case here. For a constant foam depth d in beam direction, the time dependent liquid fraction of the foam can be calculated by

$$\phi x, z, t = \frac{\ln(I(x, z, t)/I_0)}{\ln(I_{liquid}/I_0)}, \tag{4.2}$$

where I_{liquid} is the transmitted intensity after attenuation of beam by liquid metal of thickness d (i.e., the melt before it has foamed, at 100% liquid fraction). The key external factor affecting drainage is gravity, which acts in the (vertical) z-direction only. We can therefore average all pixel values in the horizontal x-direction to arrive at an integrated liquid fraction profile which is a function of position z and time t only (the density values in the y-direction are already averaged by the beam traversing the sample). This averaging process gives smoother, more representative profiles and can be calculated with:

$$\phi(z,t) = \frac{\ln\left(\frac{1}{n}\sum_{i=0}^{n} I(x_i,z,t)/I_0\right)}{\ln(I_{liquid}/I_0)}. \tag{4.3}$$

A series of radioscopic images — with the corresponding gravity levels — were recorded, allowing qualitative observation of the foaming process (see Figure 4.2). These images cover the changes in the foam structure during one parabola, i.e., $1\ g \rightarrow 1.8\ g \rightarrow 0\ g \rightarrow 1.8\ g \rightarrow 1\ g$.

Pronounced gravity-induced drainage was observed near the completion of the foam expansion of an AlSi6Cu4 foam at 650 °C during the first 1.8 g phase. Transition to microgravity induced a homogeneous liquid fraction distribution all over the foam in a few seconds, followed by a strong drainage to the bottom of the foam at the transition from $0 \rightarrow 1.8\ g$. The radioscopic images of this transition were used as input for the quantitative analysis presented in Section 4.2.2. Figure 4.3 shows two X-ray images extracted from a radioscopy series of the expanded AlSi6Cu4 foam obtained *in-situ* during the transition from $0 \rightarrow 1.8\ g$. Large changes in the foam are apparent even though the images are separated by just one second, emphasising the rapidity of the liquid flow due to drainage. As

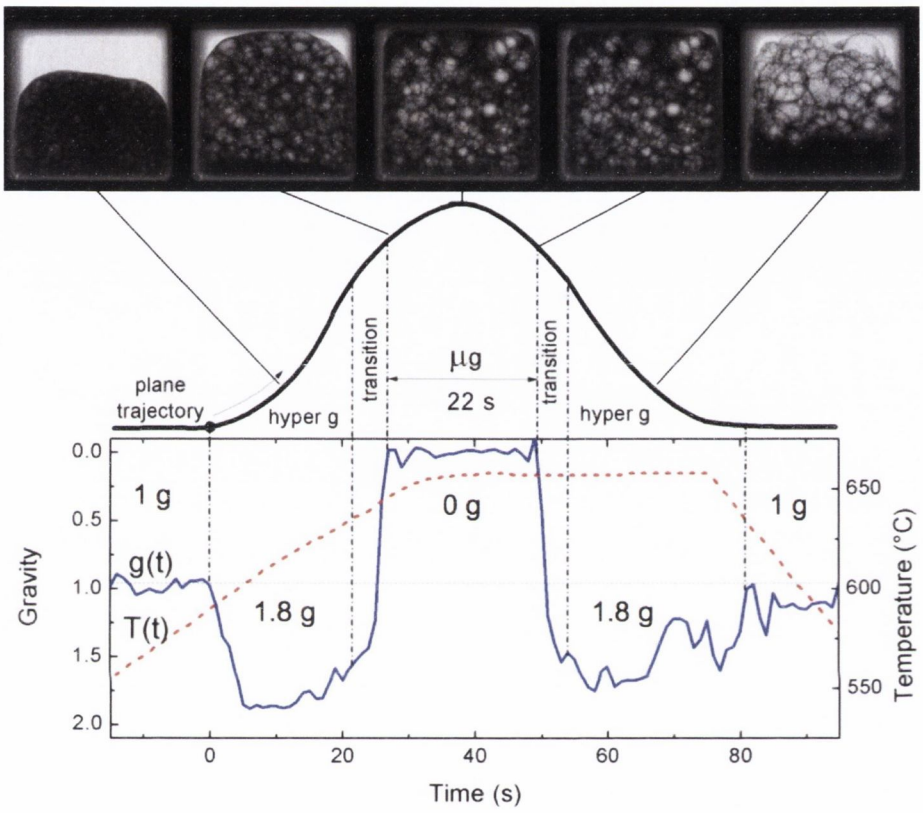

Figure 4.2: An outline of a parabolic flight. The temperature $T(t)$ of the melt during the parabola is shown by the dashed line, with the gravity $g(t)$ in blue (bottom). The radioscopic images on top show the evolution of an AlMg6Cu4 foam sample. Note that the gravity profile $g(t)$ is inverted, with microgravity at the top and hypergravity at the bottom. It should also be noted that there is not a smooth variation of gravity, with some 'jitter' observed throughout. In some cases, this may lead to negative values of gravity during microgravity stages of the flight. Images courtesy of Francisco Garcia-Moreno, Helmholtz Zentrum Berlin.

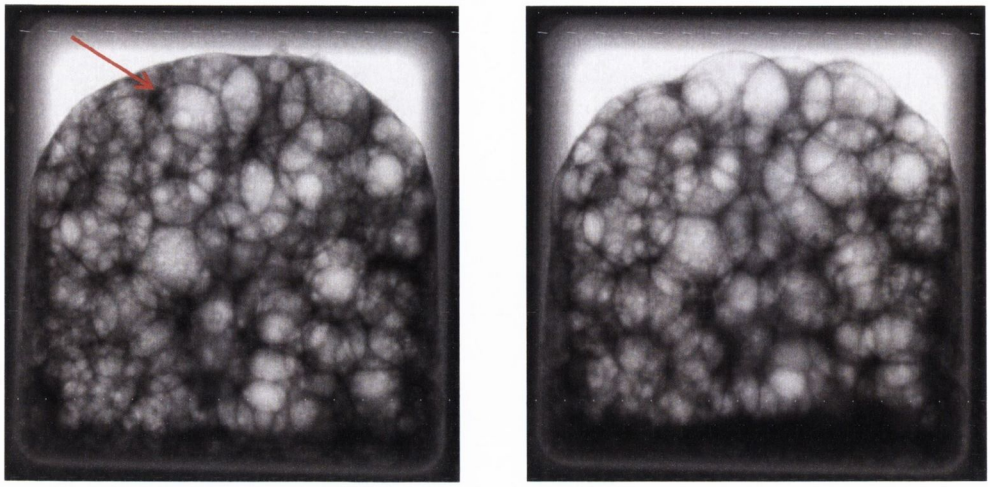

Figure 4.3: X-ray radioscopic images of an AlSi6Cu4 liquid metal foam (with 0.6 wt.% TiH_2 blowing agent), during the transition from 0 g (left) to 1.8 g (right). The time between images is one second. The arrow indicates a ruptured bubble. Note the swift increase in pooled liquid metal collecting at the bottom of the foam. Images courtesy of Francisco Garcia-Moreno, Helmholtz Zentrum Berlin.

the upper part of the foam dries out, melt is collected at the bottom, leading to a vertical liquid fraction gradient. Despite the large liquid rearrangement, most of the bubbles can still be identified. Coalescence of bubbles was limited in this time period, with just a few events observed (one example is indicated by an arrow).

In Figure 4.4, the variation of drainage in AlSi9 foams with concentration of SiC particles is shown (from left to right, 5, 10 and 20 vol.% of SiC particles, respectively, at 700 °C, after the $0 \rightarrow 1.8$ g transition). The liquid flow is visibly reduced as more particles are added. This can be clearly seen in the greatly reduced amount of melt collected at the bottom of the 20% SiC sample as compared to the 5% SiC sample.

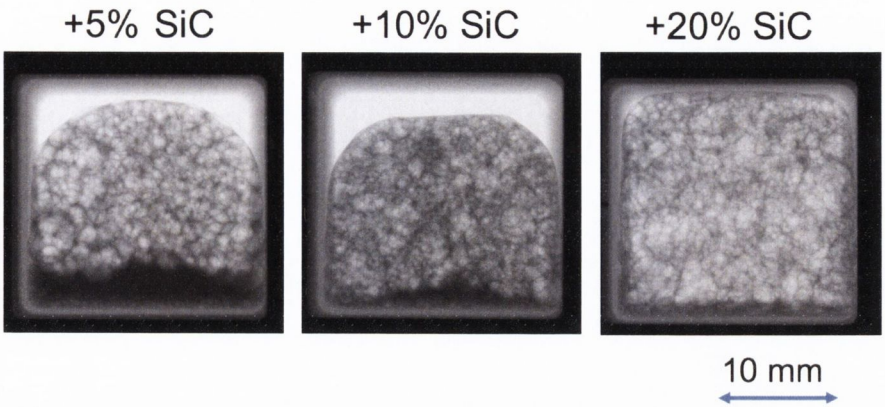

Figure 4.4: Drainage in AlSi9 foams varies dramatically with concentration of SiC particles (from left to right, 5, 10 and 20 vol.% of SiC particles, respectively) at 700 °C, after the $0 \rightarrow 1.8\ g$ transition. The liquid flow is visibly reduced as more particles are added (most obviously in the amount of melt collecting at the bottom of the foam). Images courtesy of Francisco Garcia-Moreno, Helmholtz Zentrum Berlin.

4.3 Determining melt parameters from numerical solutions

4.3.1 Numerical analysis of radioscopic images

The experimental data (after processing using the algorithm outlined in Section 4.2.2) consists of a series of liquid density profiles for each experiment, i.e., for each value of the SiC concentration studied. An example of the liquid fraction profiles studied may be seen in Figure 4.5.

The data consists of approximately 25 seconds of usable profiles, captured at a rate of 4–8 per second (depending on the experimental configuration used). As the frame-rate is relatively low, there can be large variations between profiles. Due

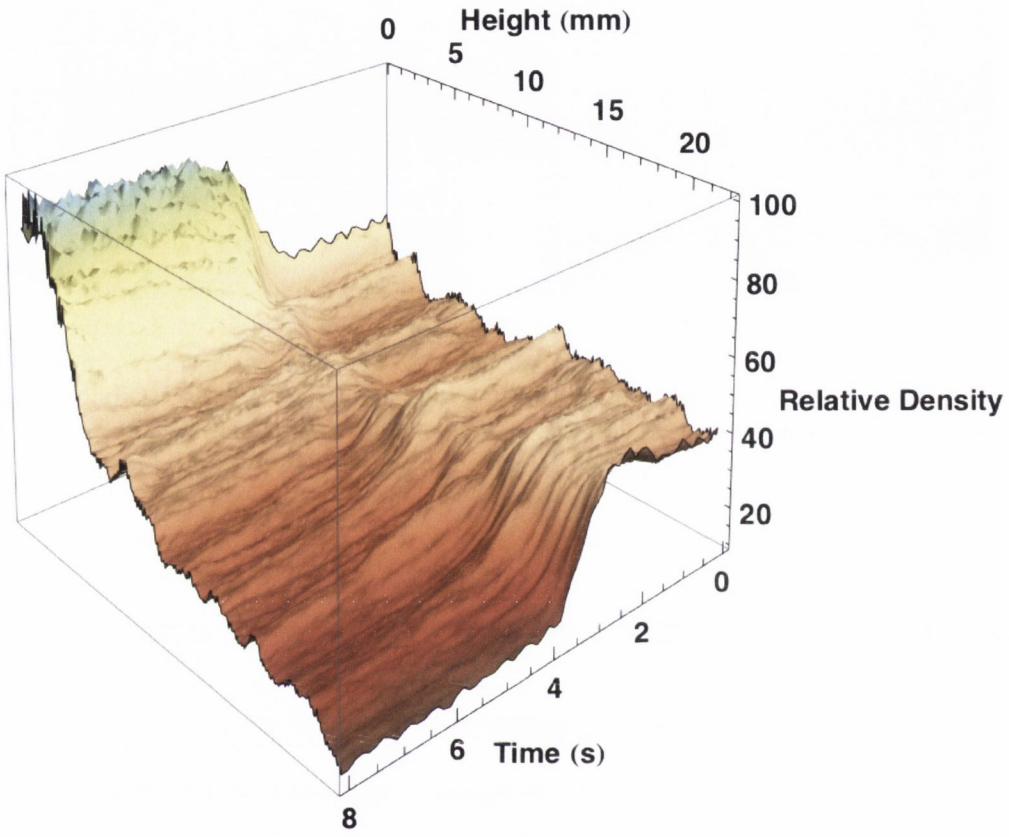

Figure 4.5: Experimentally obtained liquid fraction profiles of an AlSi6Cu4 foam recorded over a parabolic flight. The profiles start in microgravity (with time increasing from right to left), after the precursor had fully melted and expanded to fill the foaming crucible. The density of the foam is relatively homogeneous and remains so until approximately $t = 2$ seconds, when we enter a hypergravity phase of the parabolic flight. The onset of drainage is readily apparent from the images, and the foam tends quickly towards a final drainage profile at $t = 8$ seconds.

to the limited number of bubbles making up the foam melt, any bubble rupture can have a large effect on the liquid profiles due to the ensuing rearrangements. Previous research by Garcia-Moreno et al. [64] suggests a rate of 2.5–5 bubble ruptures per second for the sample sizes used in these experiments.

Rather than using all of this data to determine a single set of values for the parameters of the system, we split the data into multiple subsets. Each of these subsets is defined by the start time and duration, with subsets allowed to overlap (i.e., one subset may start at $t = 0$ and run for 5 seconds, while another starts at $t = 2$). This decision was taken to mitigate the effect of noise in the experimental profiles — even if one subset contains spurious data due to (for example) a large bursting bubble, we can still determine useful values for surface tension and viscosity from other subsets. This process is graphically explained in Figure 4.6. The shorter lengths of each subset also minimises any effect of coarsening on the sample. As we do not have 3D information on the melts available (instead working from 2D projections), we cannot directly measure the bubble volume from the experimental data. We instead calculated an average bubble volume from the radioscopic images using the Kelvin foam approximation discussed in Section 2.2 (i.e., noting that a Kelvin cell with edge length L has volume $8\sqrt{\pi}L^3$, and approximating our foam as a collection of Kelvin cells). We took multiple measurements of edge lengths from each image and analysed images from different times during the experiment. This was done to minimise the effect of changing bubble volume on our numerical solutions, and to reduce the error of coarsening on the bubbles that made up the liquid metal foams. Over the time-scales of our image sequence subsets, coarsening appeared to have a quite limited effect, with average bubble size increasing only by a factor of 1.05 – 1.1.

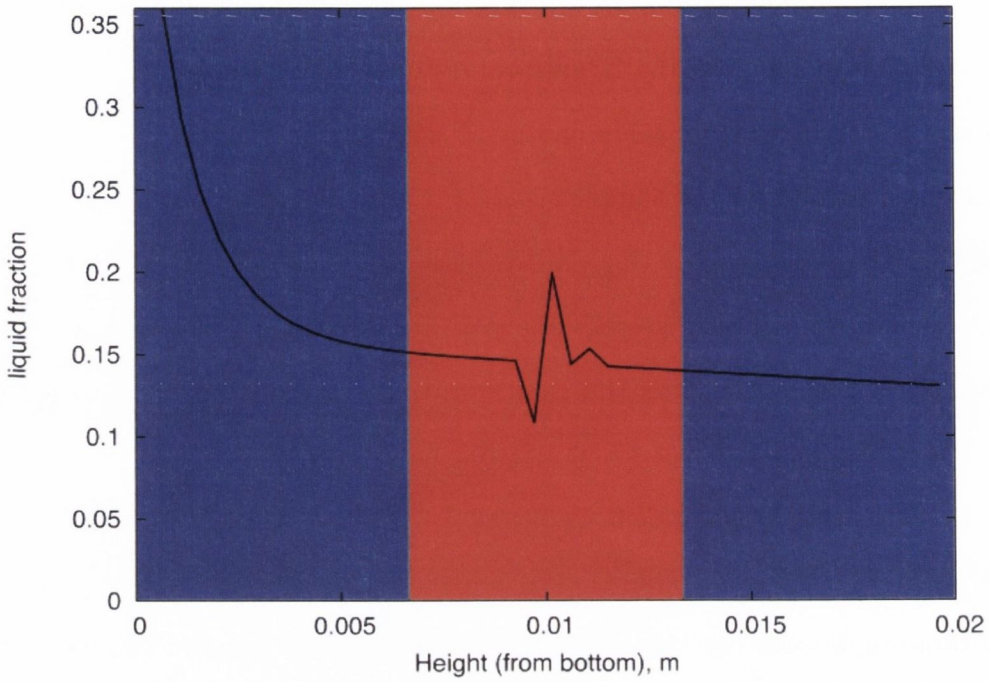

Figure 4.6: Conducting multiple fits over different subsets of the same drainage profiles allows us to minimise the effect of noise or bursting bubbles on the final results. In the figure, we see three fit sections. The blue sections are 'good', and should be well fitted. However, the red section is 'bad', with spikes in the profile which may throw off the fits. By calculating all three fits we can still extract some useful results. In the real fits, these sections are allowed to overlap and the process is repeated for sections of different length.

The starting profile from each subset was set as the 'seed' profile for our simulations, and we chose starting values for the surface tension and viscosity. From these starting conditions, we could numerically integrate the Foam Drainage Equation (Equation 2.1) to generate a prediction of how that foam would evolve[1]. We used the experimentally measured gravity values to take into account the variation of gravity during the experiment. The value $g(t)$ was set at every time-step

[1]This may be considered a more complex variant of the process outlined in Section 2.4, as we are working with the full FDE rather than a linear approximation.

during the evaluation, using a precise measurement, if available, and interpolating otherwise.

We then fitted the integrated numerical solution to experimental data starting from the same 'seed' profile. This fit was used to update our initial guesses for the surface tension and viscosity. The process was repeated until we were satisfied that a best-fit had been achieved. Note that this approach required many such numerical solutions, as each fitting iteration changed the initial conditions of the integration. An example of a final fit is shown in Figure 4.7, with the differences between the experimental data and simulations plotted in residual form in Figure 4.8.

Numerical integration was carried out using an explicit finite difference method with forward differences. This approach is computationally efficient to solve, which is important as our algorithm requires many complete solutions to power the fitting process. While implicit integration methods are usually preferred due to improved stability, previous work found that explicit methods are sufficiently stable for our use [65]. Space- and time-steps were chosen to balance speed with numerical accuracy.

We compared the simulation to experiments on a grid defined by Δt (the interval at which experimental profiles were captured) and Δz (the vertical resolution of the detector). This comparison (over multiple experimental profiles, depending on the duration of the simulated evolution) provided the basis for using a fitting algorithm to choose the best pair of γ, η values for the experimental system. We conducted the fits using the MIGRAD minimiser from CERN's MINUIT software [50]. By conducting multiple fits, each with a different starting point and evolution length, we were able to arrive at a more representative value for each

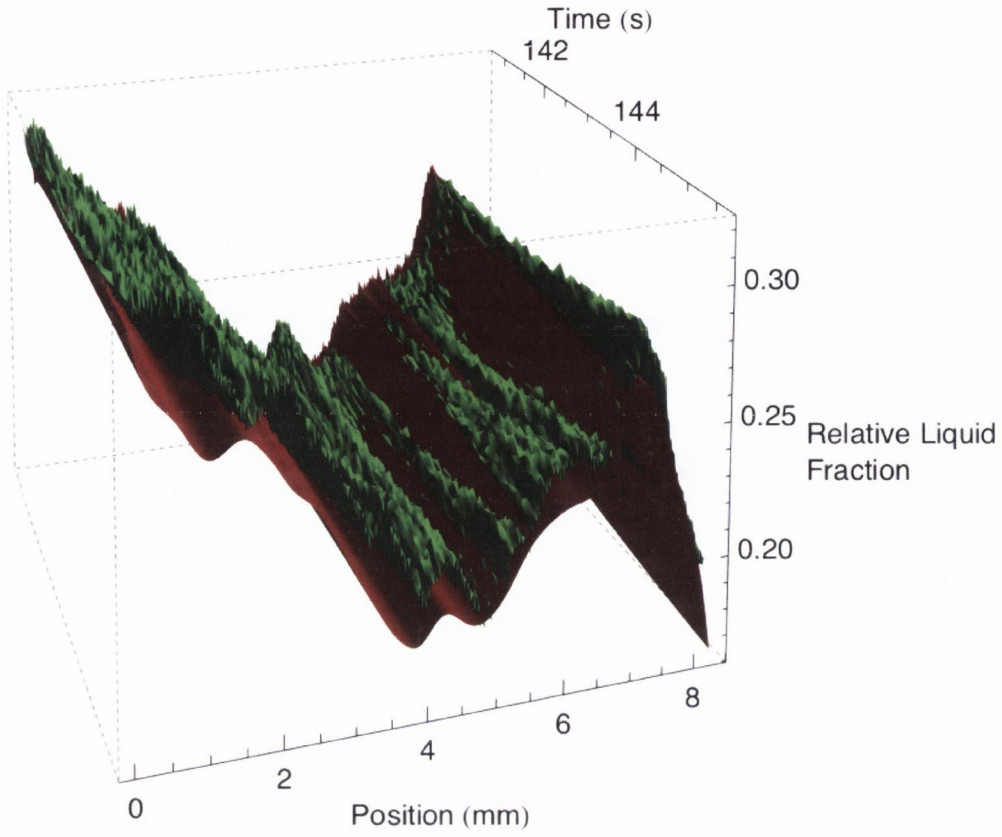

Figure 4.7: An example of a final fit for an AlSi9 + 5 vol.% SiC liquid metal foam, with experimental data shown in green and the numerical solution shown in red. Both liquid fraction curves start from the same base liquid fraction profile (starting at 141 s)

parameter and provide some measure of the error using the standard deviations. For more information on this software, see Appendix D.3.

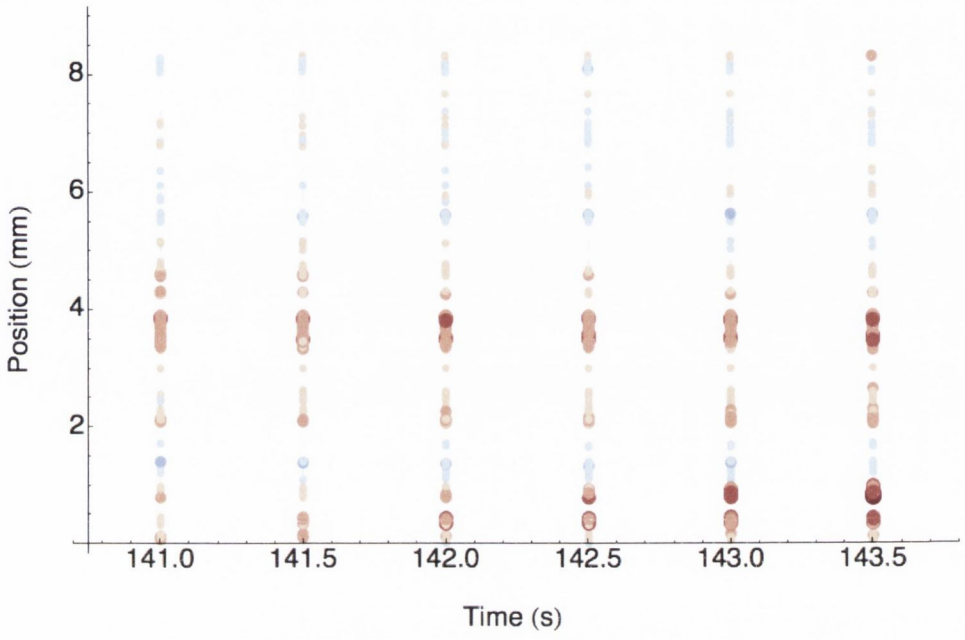

Figure 4.8: By plotting the residuals between the experimental data and fitted simulations for an AlSi9 + 5 vol.% SiC liquid metal foam (i.e., the data shown in Figure 4.7) we can see how the fits under- and over-estimate the liquid fraction profile. In this figure the magnitude of the residual is given by the size of the circle, with positive residuals in red and negative in blue. We can see, therefore, that in this case the fit tends to over-estimate the liquid fraction closer to the bottom of the foam, and that the residuals become larger as time progresses.

4.3.2 Results from numerical solutions

We calculated surface tension and viscosity by treating them as fit parameters in a fit between numerical calculations and experimental data. By averaging the results over many fitting runs, we extracted values for experimental systems with varying amounts of SiC. The obtained results for foams of AlSi6Cu4, AlSi11 and AlSi9 + 5, 10 and 20 vol.% SiC are presented in Table 4.1, together with bulk values for comparison extracted from the literature. Note that the errors of the

analysed foam properties shown are the standard deviations of the results taken over many fitting runs.

The viscosity of the AlSi6Cu4 foam was found to be 25 and 30 times higher than that of bulk cast Al and AlSi7, respectively. For the AlSi11 foam, viscosity was found to increase by more than 35 times (in comparison to the corresponding bulk alloy). An even higher viscosity increase was measured for AlSi9 + SiC foams, with values 65 to 120 times higher than pure Al, and 75 to 140 times higher than bulk AlSi9 alloy, depending on the particle content. There is also a trend of increasing viscosity corresponding to increasing SiC concentration, with viscosity almost doubling as particle content is increased from 5 to 20 vol.%.

The surface tensions of the AlSi6Cu4 and AlSi11 foams at 650 °C are up to 25 % lower than the literature values for bulk Al, AlSi7 and AlSi9 at 700 °C [67]. The surface tensions of foams of the alloy AlSi9 + SiC at 700 °C are up to 38 % lower than the corresponding bulk values without particles [67]. There is also a small trend of increasing surface tension with increasing SiC concentration, but the trend is comparable to the standard deviations.

The errors presented for our fitted values are calculated by taking the standard deviations of all the fitting run results. However, there may be other errors arising from uncertainty in other parameters in the FDE. Most importantly, we assume a constant average bubble volume over the fitting duration of each subset. If there was in fact some small variation in this volume it would affect the fitted values. To quantify any potential error arising from this effect we ran fits to the same subsets of data, varying deliberately the bubble volume each time ($0.9V_b, 1.0V_b, 1.1V_b$). We found that a 10% change in bubble volume led to approximately 2–3% changes in surface tension and viscosity. This error could not account for the very large

Alloy	Formation path	Temperature ($^\circ C$)	Surface Tension (N/m)	Viscosity ($mPa\ s$)
AlSi6Cu4 (+0.5 wt.% oxides)	PM, thixocast, foam	650	0.78 ± 0.02	31 ± 4
AlSi11 (+0.5 wt.% oxides)	PM, foam	650	0.65 ± 0.02	37 ± 3
AlSi9 +5 vol.% SiC	bulk, foam	700	0.53 ± 0.05	80 ± 10
AlSi9 +10 vol.% SiC	bulk, foam	700	0.57 ± 0.04	120 ± 10
AlSi9 +20 vol.% SiC	bulk, foam	700	0.61 ± 0.04	150 ± 20
Al	bulk, cast	660	-	1.38 [66]
Al	bulk, cast	700	0.869 [67]	1.23 [68]
AlSi7	bulk, cast	700	0.857 [67]	1.08 [69]
AlSi7 (+0.5 wt.% oxides)	PM precursor	700	-	1.7 [70]
AlSi9	bulk, cast	700	0.854 [67]	1.08 [69]
AlSi11	bulk, cast	650	-	1.16 [71]
AlSi11	bulk, cast	700	0.849 [67]	1.06 [69]

Table 4.1: Results for surface tension and viscosity for AlSi6Cu4, AlSi11, and AlSi9 + 5, 10 and 20 vol.% SiC foams obtained from fitting numerical solutions of the foam drainage equation to experimental liquid density profiles. Bulk values for aluminium and aluminium alloys from literature are listed for comparison. PM indicates an alloy formed using the 'powder-melt' technique.

values of viscosity measured, suggesting that these results are quite insensitive to limited bubble volume variation.

4.3.3 Discussion of numerical results

Viscosity

While operational temperature [71, 72] and alloy composition [69] have been experimentally shown to have slight effects on the viscosity of molten metals, they cannot account for the large, order-of-magnitude increases in viscosity found in the microgravity experiments on foams.

We turn, therefore, to the particle content of the melt (either in the form of added particles or oxides) and to structure of the foam itself, consisting of thin films and Plateau borders.

Reproducing Equation 2.1 here for clarity, we propose additional terms for the effective viscosity contained in the Foam Drainage Equation

$$\frac{\partial \phi}{\partial t} + \frac{1}{\eta^*}\frac{\partial}{\partial z}\left(\rho g \frac{V_b^{2/3}}{5.35}\phi^2 - \frac{C\gamma}{2}\sqrt{\frac{V_b^{2/3}}{5.35}}\phi\frac{\partial \phi}{\partial z}\right) = 0. \tag{4.4}$$

The effective viscosity $\eta^* = 3 \times 50 \times \eta_{liq}$, where η_{liq} is the bulk melt viscosity. The factor 3 in η^* arises from the 3D nature of the Plateau border network and 50 from the channel geometry. The addition of stabilising particles (or the presence of oxides) will further augment the effective viscosity, leading to an effective viscosity for the liquid metal in the foam with the form

$$\eta^* = 3 \times 50 \times S \times P \times \eta_{liq}. \tag{4.5}$$

Alloy	Temperature	P	S
AlSi11 +0.5 wt.% oxides	650 $°C$	1.6 [70]	25
AlSi9 +10 vol.% SiC	700 $°C$	2.0 [73]	55
AlSi9 +20 vol.% SiC	700 $°C$	3.2 [73]	42

Table 4.2: Experimentally determined values for the particle factor P (the increase in viscosity of bulk alloy by the addition of particles) allow us to calculate S (the contribution of the altered foam structure) from our numerically-calculated values generated from the fits to experimental data.

Here, P is a factor related to the presence of solid particles in the melt (as the bulk viscosity will be changed from that of a pure metal by the addition of particles) and S is a structural component related to changes to the foam structure due to the presence of particles.

P has been determined experimentally for several of the foams under consideration in this work, allowing us to calculate the contribution of S as well. The parameters determined in this manner are summarised in Table 4.2.

We find $S \gg 1$ for all foamed structures. This structural effect is likely made up of several contributing processes, outlined in Figure 4.9. The presence of particles in the liquid flowing through the borders will be limited by the reduced area of the borders (from particles adsorbing onto the walls) and from particle-particle interactions (jamming of freely-flowing particles with fixed particles) [56].

Particles slow down drainage due to the increased viscosity of the associated melts, but explaining foam stability solely by this increased viscosity is too simplistic. Particles also adhere to gas/metal interfaces and prevent rupture of such films. In this way — rather than just slowing down the decay — the lifetime of foams can be increased massively. Therefore, particles have a dual function: they first stabilise thin metal films in which the melt, then lead to the high effective

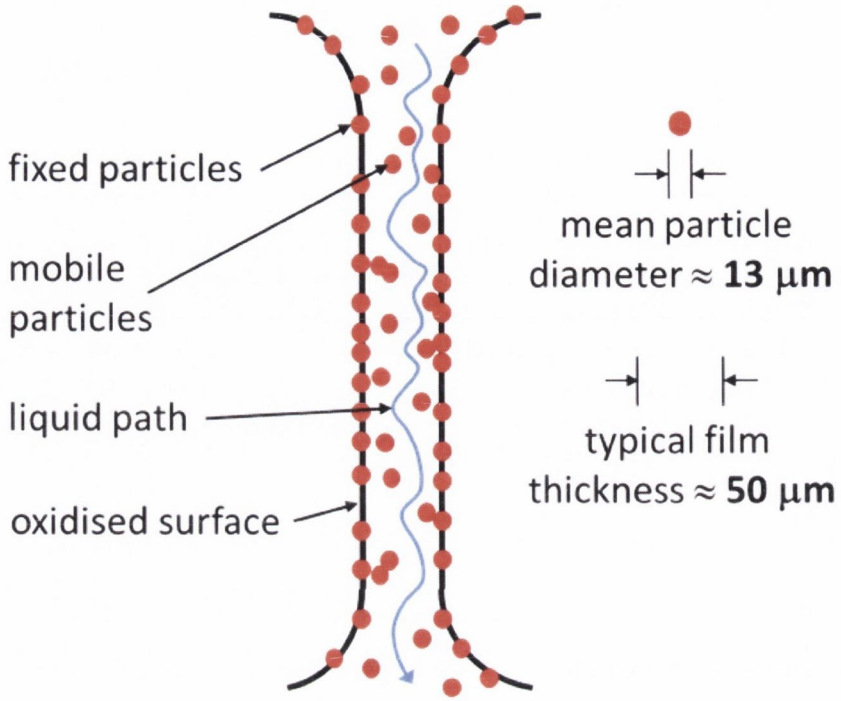

Figure 4.9: The structural effects leading to the factor S increase the effective melt viscosity in multiple ways, from hindering flow (e.g., jamming between mobile particles and fixed particles) to reducing the effective area of the Plateau borders.

viscosity quantified in the present work. We will look more closely at an analogous form of film stability in aqueous foams in Chapter 5.

Surface Tension

Like viscosity, the surface tension of aluminium is weakly affected by an addition of silicon [67]. The present measurements show that further alloying and/or addition of particles reduces surface tension. Surface tensions of liquid AlSi11, AlSi6Cu4 and, especially, AlSi9 + SiC foams are lower than the values of the corresponding bulk alloy found in the literature. The presence of partially wetting solid particles in the melt surfaces can indeed modify the values of surface tension [56, 64]. A

lower surface tension would enhance foam stability as the total interfacial energy is decreased. However, since the measured effect is rather small compared to the increase of viscosity, surface tension is unlikely to play a dominant role in foam stabilisation (although it will contribute to the enhanced stability of the foam). Finally, variations of the concentration of surface adsorbed particles over the surfaces will lead to surface tension gradients, creating stabilising and restoring forces in a manner analogous to the Marangoni effect (see Chapter II for more details).

4.4 Conclusions and Outlook

Metal foams are promising advanced materials, with potential applications in areas as varied as prosthetics and vehicle design [74]. However, analysing such foams in their molten state has proven difficult due to the hostile environment of liquid metal. Current methods rely on destructive *ex-situ* tests, which make reasoning about the processes that affect formation more difficult, hindering the development of these materials.

We present here the first analysis of metal foam viscosity and surface tension based entirely on *in-situ*, non-destructive measurements and novel applications of numerical simulations. Our approach has the potential to allow more detailed measurement of key properties of metal foams, providing valuable direction for experimentalists and engineers. X-ray radioscopic data for metal foams undergoing free drainage during parabolic flights was collected and processed. We iteratively fit numerical solutions of the Foam Drainage Equation to subsets of these data, allowing melt viscosity and surface tension to vary as free parameters of the fit.

By averaging multiple fits, we determined values for these key parameters without destroying the foam or otherwise interfering with it in the liquid state.

From these results, several points become immediately obvious. We observed increased viscosity of all examined alloys when comparing foams to bulk molten metal. This is likely due to the changes in foam structure arising from the presence of oxide layers or SiC particles. Addition of particles has been seen to increase viscosity in bulk molten metal but, even factoring this into account, we still observe viscosity increases of over an order of magnitude. Previous work has also qualitatively observed dramatic increases in viscosity in this manner [70]. The presence of oxides and SiC particles appears to reduce surface tension, but this effect is much smaller than that observed for viscosity.

Going forward, we note that while our method is used here to analyse metal foams, it is completely general in its approach. It requires only time-dependent liquid fraction profiles and could be applied to other systems of interest, such as polymeric foams [75, 76]. We note again the non-invasive nature of this approach, which does not require direct contact measurements from the foam (which could damage or destroy the samples). By using a more sensitive (and faster) X-ray flat panel detector, time resolution could be further improved, allowing for improvements in the determination of the viscosity and surface tension.

Part II

Foam Stability

Chapter 5

Statistical analysis of soap film lifetimes

5.1 Introduction to foam stability

While most familiar bubbles and foams tend to be ephemeral in nature — bursting and collapsing as we watch — given the right conditions, foams may be remarkably stable, lasting for periods of months [77]. There are several ways to increase the stability and longevity of foams, usually involving the removal of one or more of the causes of foam decay[1]. Firstly, the environment the foam is contained in has a significant effect. Humidity and temperature may increase evaporation of liquid from the foam, while particles in the atmosphere (such as dust) can easily trigger the rupture of a soap film. The process of foam drainage decreases the liquid

[1]Of course, the converse is also true, and foam decay may usually be hastened by the inverse processes.

content of the foam, weakening it and amplifying the effects of other destabilizing mechanisms. The chemical composition of the foam (e.g., the concentration of surfactants) also has a significant effect. The main stabilizing mechanism of surfactant-based foams is the Marangoni effect [5], which redistributes surfactant molecules over the entire soap film in response to surface tension gradients, counteracting thinning of the films and resisting film rupture. In this Chapter, we will consider the stability of the individual components of a foam — the thin films that make up the interfaces between bubbles — and how they age and weaken.

To consider the stability of a foam — an issue of great practical importance in industrial applications (where it may be desirable to increase foam stability or decrease it) — we must first understand the stability of the individual films that make up a foam. Much of the previous work on soap film stability and lifetimes has dealt with micro-scale films, or single films [78]. In many real-world foams, the constituent films tend to be larger, and it is not clear whether or not previous results can be extrapolated to larger scales. Here, we will present an experiment which took a statistical approach to determining soap film lifetimes. The experiment was designed to remove as much outside influence on the films as possible, focusing in on the ageing of static films.

During 2009, we carried out an experiment on soap film lifetimes as part of a public exhibition on foams[2]. This experiment was designed to take advantage of the projected large attendance in order to generate large data sets which would lend themselves well to rigorous statistical analysis of many individual soap films, and will be described in detail in Section 5.2

[2]The exhibition was hosted in the Science Gallery, Dublin, and was titled 'BUBBLE'. More information about the gallery may be found at `www.sciencegallery.com`.

We had a secondary aim (inspired, in part, by the public nature of the experiment) of presenting a pedagogically useful example of unpredictability. There has been mounting concern that physicists are not taught statistics and probability well [79–81]. This issue has been noted in other fields as well — the discovery of widespread errors due to the incorrect application of certain statistical methods in medical research [82] is a prime example. As research generates ever-increasing volumes of data [83], a good understanding of statistics and probability will become even more important. This experiment provided an ideal platform for observation and further statistical analysis. It also made contact with the general theory of failure (such as electrical breakdown or fracture under stress [84]) in materials.

Previous experiments on the lifetimes of soap films were on a much reduced scale. Rämme [85] presented a study of 42 bubbles which were exposed to the atmosphere during experimentation. We studied a far greater number of bubbles which were protected from environmental influences throughout. More importantly, we collected sufficient data to determine a lifetime distribution. We were able to determine the probability distributions that govern such film lifetimes, which may allow predictions to be made about the more general cases. We will also comment on possible mechanisms of rupture.

5.2 Experimental set-up

(The author would like to thank Brendan Bulfin for assistance in running the experiment, and Aaron Meagher for design of the apparatus).

Due to the public nature of the exhibition, the experiment was designed to be engaging and to allow visitors to take part. Visitors were given the task of filling a

perspex tube with equally-spaced parallel soap films, or a "bamboo" foam [3, 5, 86, 87]. Design decisions were made to increase repeatability and reproducibility as much as possible given the public setting of the experiment (including supervision by an assistant, and the use of a guide to ensure correct tube position and angle). When the perspex tube was correctly positioned, air was bubbled into the tube at a constant gas flow to create a foam (containing approximately 10–20 films). The position of the tube was chosen to ensure that the foams created by different visitors were as similar as possible. The tube was then corked (with stoppers wetted from the same soap solution) to isolate it from the environment. The number of circular films remaining in each tube was recorded every day. Over the course of the exhibition, 150 samples were created in this manner for a total soap-film count of 2,586. This data provided the foundation on which statistical analysis could be based.

The apparatus used is shown in schematic form in Figure 5.1. Air flow was provided using a consumer aquarium pump (and rubber tubing) which injected air into a solution of approximately 3 parts in 11 commercial dish-washing detergent (Fairy Liquid). A constant gas pressure lead to the formation of approximately equal-volume gas bubbles. The rising bubbles were then collected in a perspex tube with an internal diameter of 16 mm. If the ratio of tube diameter to bubble diameter (referred to as λ in the literature) is in the range 0.44–1.25, the bubbles self-order into a regular bamboo-like structure [3, 88–90] consisting of equidistantly-spaced parallel soap films.

For the set-up used in the exhibition, we found it useful to place the tube at an angle as shown in Figure 5.1. We required monodisperse bubbles with a volume sufficient to ensure adequate spacing between films (1 to 2 cm). Increasing the gas

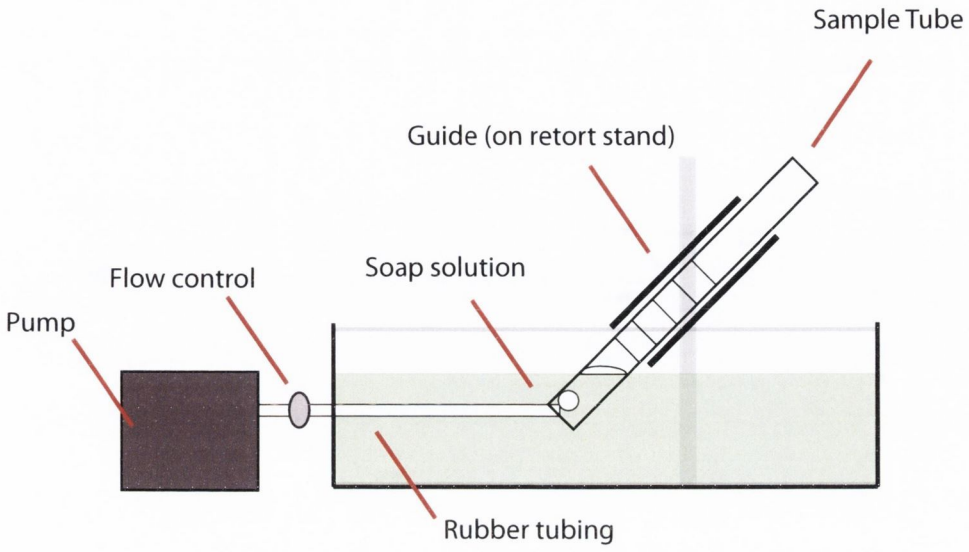

Figure 5.1: A schematic representation of the creation of parallel and equally-spaced soap films in a tube. The bubble volume is controlled by the tilt angle of the tube (approximately 35 degrees, as measured on the guide) and by constant gas flow from a consumer aquarium pump. For the former control mechanism to be effective, the bubbles need to be in contact with the tube wall as they emerge from the rubber tubing.

flow rate to achieve this spacing can lead to turbulence [91], which would prevent formation of the required ordered structures. By using a low gas flow rate and holding the tube at a fixed angle (approximately 35°) with the aid of a guide, we were able to create foams of the required quality [92]. At this angle, the bubbles are 'pinned' to the sloped wall as they are generated, allowing them to grow larger than would be possible with purely vertical tubes. Consumer aquarium pumps proved sufficient for this purpose.

The tube was then labelled with the name of the participant and the date the sample was created, and displayed vertically on a wall in the Gallery (see Figure 5.2 and 5.3). The tubes were mounted vertically, as orienting the tubes horizontally (and hence vertically orienting the films) would result in films of non-uniform

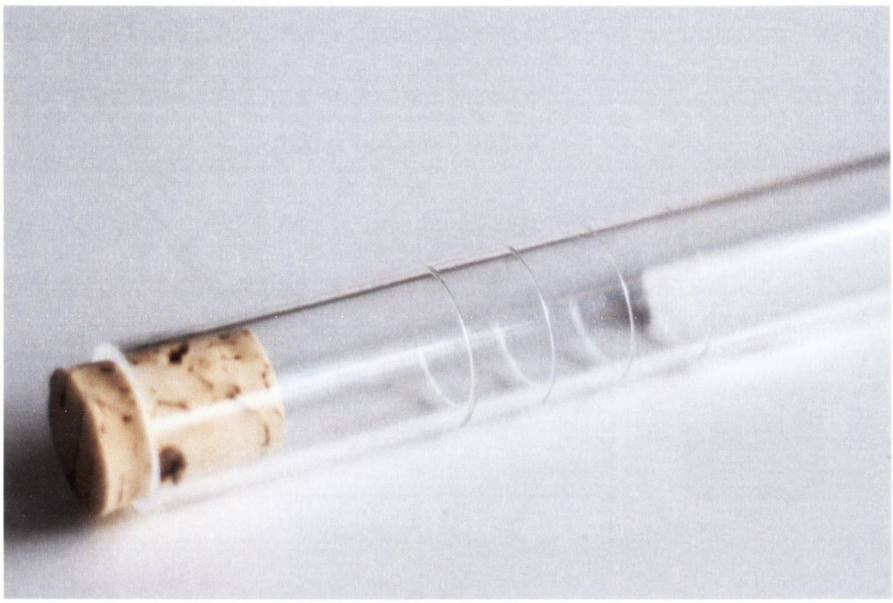

Figure 5.2: A close-up of a single sample created by a member of the public. The parallel soap films that define a bamboo foam are clearly visible. The corks used to seal the tube were wetted in the same solution that was used to create the foam. The identifying label can be seen to the right of the image.

thickness due to the drainage of liquid from the films under gravity. Furthermore, liquid would gather in the meniscus at the lower part of the film and, without the guarantee of an accurate horizontal tube display, liquid could drain from the films and gather at one end of the tube.

Foam samples were created mainly over the first month of the exhibition, with new samples added when all films in an existing sample burst (thus maintaining a full rack of tubes). The day-to-day environment of the Gallery was outside our control (for example, temperature and humidity levels could vary daily) and, due to the duration of the experiment, these effects may have been exacerbated by changing weather (going from Summer to Autumn). Another issue involved physical interference with experimental samples by members of the public (for

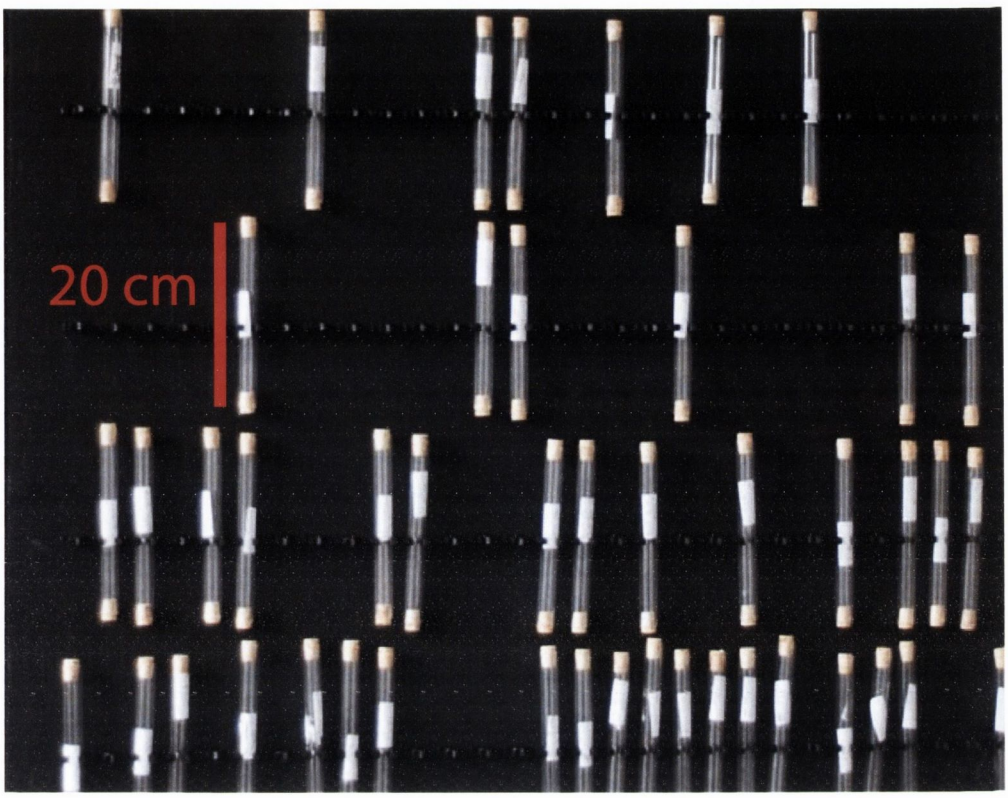

Figure 5.3: A snapshot of the public display of tubes containing soap films in the Science Gallery. The gaps show where samples were removed after all films had burst in the corresponding tubes. The tubes were aligned vertically to ensure the liquid content of the horizontal films remained constant and to minimise drainage of liquid from the films.

example, children playing with the samples). Where possible, steps were taken to mitigate such effects through the use of barriers and notices, but quantifying the effect is likely impossible.

Every day, the total number of films contained in every tube was manually counted. Because the soap films became very thin as the experiment progressed, every tube had to be carefully examined (complicating visual measurements, a burst film may leave a soap ring behind where it contacted the tube). To avoid miscounts, films were recorded only if they were seen to produce a reflection.

When making comparisons between results from bamboo foams and more commonly-encountered foams an important caveat must be kept in mind. In most foams, the large majority of films are connected with a network of liquid channels which allow the redistribution and drainage of liquid through the foam. This movement of liquid can counter the effects of films drying out and thinning (driven by variations in the capillary pressure). However in a bamboo foam the horizontal films are effectively independent from each other (aside from very limited drainage through the films on the surface of the tubes [86, 93]).

5.3 Data analysis and results

In order to analyse the aggregate lifetime data, we must first determine which distribution function best describes it. The distributions most widely applied to lifetime data are the Weibull distribution, the Gamma distribution and the log-normal distribution [94]. Our data forms a strongly asymmetric distribution, ruling out any symmetric distribution function (including Gaussian distributions). To determine which distribution best describes our data, we applied the two-sample Kolmogorov-Smirnov test [95].

This non-parametric test determines if two samples are drawn from the same distribution. We used the Kolmogorov-Smirnov test to compare the empirical distribution to the best fit of each candidate distribution, with the null hypothesis that the data tested are from the same continuous probability distribution. The Weibull distribution was the only candidate to pass the Kolmogorov-Smirnov test. More information on the Kolmogorov-Smirnov test and the Weibull distribution can be found in Appendices E.2 and E.3 respectively.

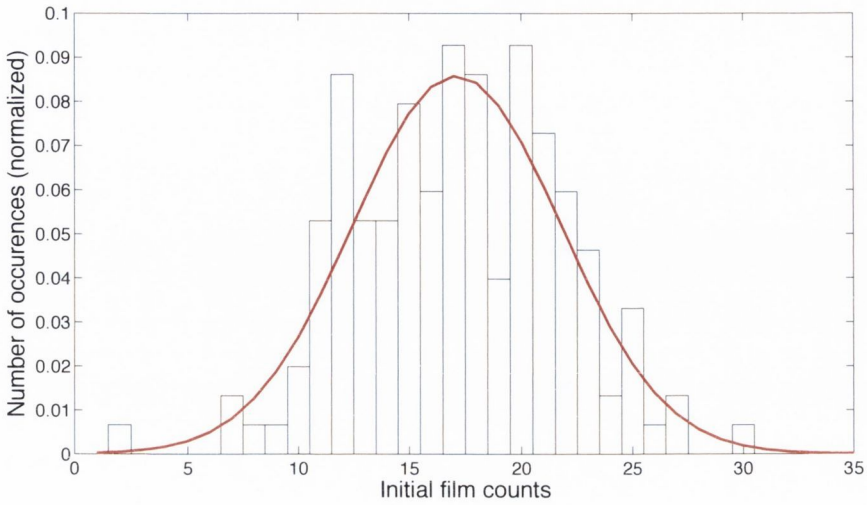

Figure 5.4: The distribution of initial film counts with a fitted normal distribution. The data is well described by the distribution, with the majority of samples starting out with between 11 and 23 films. The noise is likely due to the large number of participants in the experiment.

None of the distributions perfectly describe the initial stages of the decay, underestimating the number of failures in the first few days. This is likely due to the experimental conditions, as incorrectly-corked samples may deteriorate more rapidly. The effects of atmospheric exposure were quantified using a small control group, and will be discussed in Section 5.4.

Figure 5.4 shows the distribution of the initial number of films in the tubes. The solid line is a fit to a normal distribution. This fit, and other fits in this Chapter, were carried out using maximum likelihood estimation. For a more detailed overview of this technique, see Appendix E.1. From Figure 5.4 we can see that the majority of samples started with an initial number of films between 11 and 23.

We first consider the distribution of the bursting of films. We calculated the day-to-day differences in the film counts for every sample. This difference tells us how many films burst each day in each sample. Figure 5.5 shows a histogram of

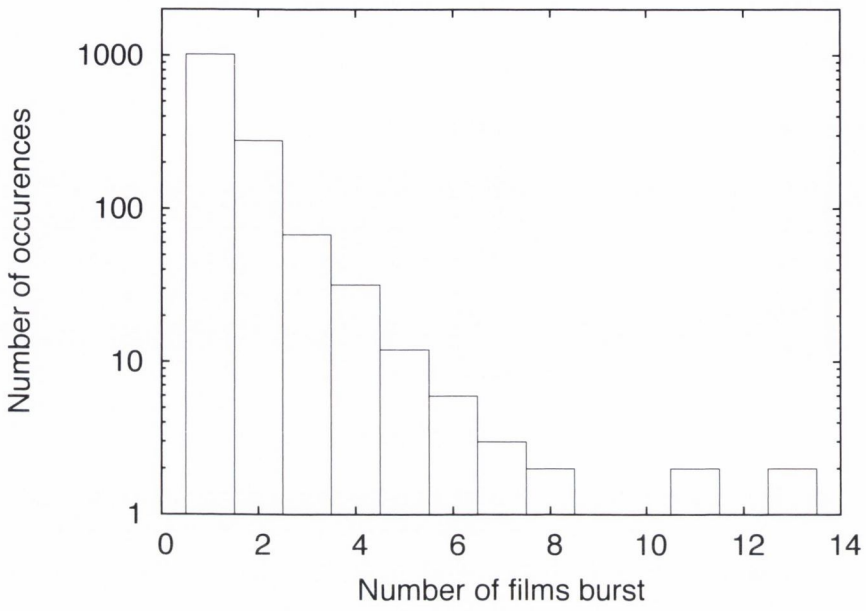

Figure 5.5: Looking at each individual tube rather than the entire experiment, we can calculate a distribution of the number of films that burst in a 24-hour period. Summing these daily distributions gives us the aggregate distribution for the entire exhibition run. The x-axis corresponds to the number of films that burst in a sample over the course of a single day. The y-axis shows the number of times this happened throughout the entire experiment. We can see that large bursting events were rare (for example, although we observed single films bursting approximately 1000 times, only two observations of 11 films bursting were made).

the number of occurrences of the different counts of film bursts, i.e., how many times n films burst in a sample in one day. By plotting on a log-linear scale, we see that approximately 90% of events involve only one or two bursts, with some large events as outliers.

From our daily records of the number of films in every tube, and our knowledge of the ages of the films, we were able to compute a lifetime distribution for the

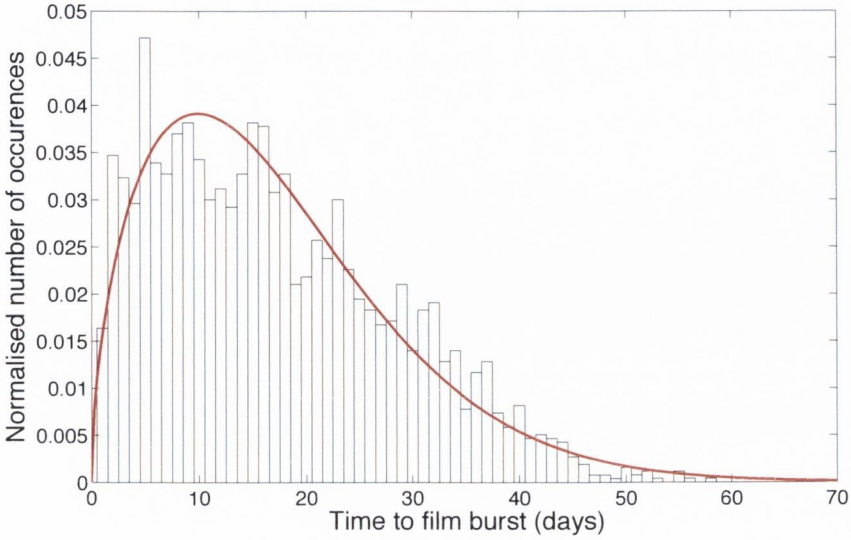

Figure 5.6: Distribution of lifetimes of individual films given by a fitted Weibull probability distribution (given by Equation E.4), with $k = 1.55 \pm 0.05$ and $\lambda = 19.2 \pm 0.5$. Despite some noise in the lifetime data, it is well-fitted by this distribution. The failure to capture the first days is likely due to improper initial tube sealing, leading to quicker film deaths.

films, which is shown in Figure 5.6. Note that although the number of films in every sample was recorded every day, it was not feasible to track individual films over their lifetimes. The data was fitted to a Weibull distribution using maximum likelihood estimation in Matlab (see Appendix E.1 for more details) and is shown as a solid line in Figure 5.6.

The differences between the fit and the data were found to follow a normal distribution, suggesting that the differences can be attributed to random factors such as the experimental environment.

Integrating the data results in a far smoother cumulative probability distribution, shown in Figure 5.7 (which also shows a fit to Equation E.5). The fits in Figures 5.6 and 5.7 result in a value for the shape parameter of $k = 1.55 \pm 0.05$. This value for k (i.e., $k > 1$) corresponds to a failure rate (the frequency with

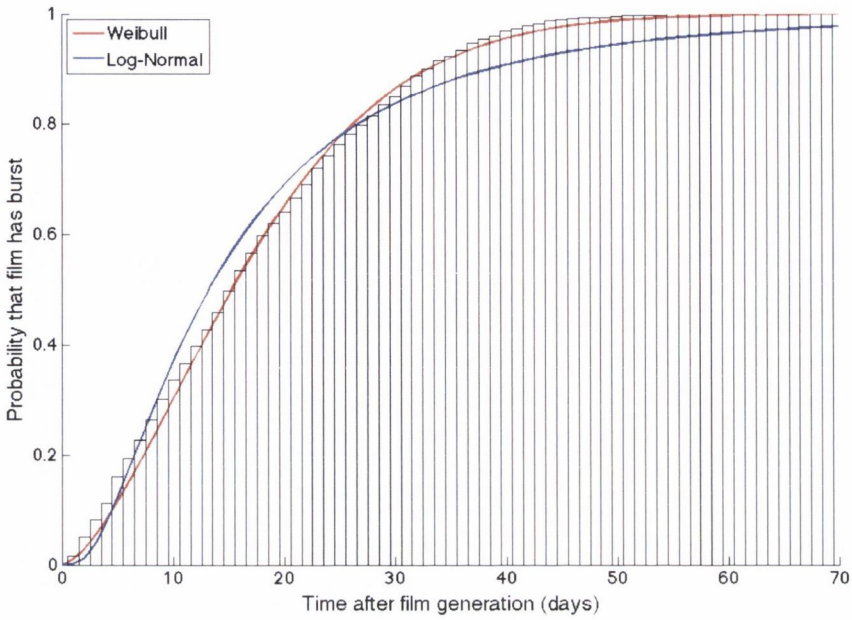

Figure 5.7: Integration of the data from Figure 5.6 results in a smoothing of the data. The red line shows a fit to the cumulative Weibull distribution (Equation E.5), with the same Weibull parameters as in Figure 5.6. A fit of the log-normal distribution is also plotted (blue line), and it is readily apparent that the Weibull distribution describes the data much better.

which some component of a system fails) that increases with time. In our case, it represents the frequency of films bursting. Experimental observations of the ageing films showed that they became thinner and, hence, more delicate over the course of the experiment.

There are several possible explanations for this ageing, including evaporation and drainage of liquid from the films. Evaporation is influenced by the quality of the seal on the sample tubes, and by the ambient temperature and humidity. Due to the nature of the experiment, these variables were outside our control. Because drainage in bamboo foams occurs only in the thin wetting films along the tube walls [86], it is very limited. Visual observations showed that most films became

black films (i.e., the film thickness decreases to approximately 20 nm or less) after 2–3 weeks, suggesting that most of the liquid has drained or evaporated by then.

To determine the possible influence of interactions between films — such as avalanches (where a film bursting triggers its neighbouring films to burst) and stabilization mechanisms — the average lifetime as a function of the initial number of films in the sample tube (local average) was plotted together with the average of all film lifetimes (global average). If interactions have a large influence on the lifetime of films, we expect the average lifetime to change with the number of films in the sample. For example, we might expect more avalanches when films are closer together. Figure 5.8 plots the comparison between the global average and local average for tubes with initial film counts in the range 11–23. Tubes with other initial film counts were excluded from the comparison due to limited statistics outside this range (see Figure 5.4). There is good agreement between the local and global averages over all initial film counts, and the average lifetime appears constant with respect to the initial film count, pointing to a limited effect from avalanches, intra-film stabilization mechanisms and other film-film interactions. We may also probe the potential effects of such mechanisms by looking for history-dependence in our samples. In other words, does the number of films that have already burst in a sample affect the expected lifetime of the remaining films? If we consider all samples that had N films at some time t, we can see whether there is any correlation between the starting film counts for those samples and their final ages. We did not find any significant dependency of this type in our data — if a sample is 10 days old and contains 10 films it is likely to survive for the same amount of time going forward whether it started with 11 films or 20 films.

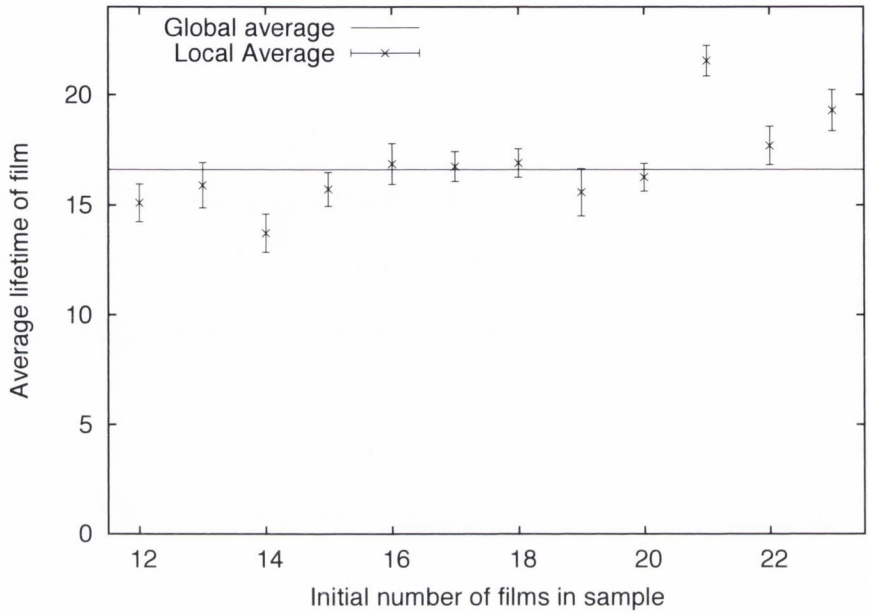

Figure 5.8: The effects of interactions between films was investigated by calculating the average film lifetime as a function of starting population. The average film lifetime appears to be independent of the initial number of films in the sample, as can be seen by comparison to the global average (solid line).

5.4 Effects of exposure to atmosphere

To examine the effects of exposure to the environment on the lifetimes of the films, we carried out a smaller-scale laboratory experiment consisting of a total of 70 films spread over 5 tubes. The samples were prepared using the same apparatus as in the main experiment, but with the sample tubes left uncorked at one end. This exposed the films to several disruptive forces, including (but not limited to) increased evaporation, airborne contaminants and air flow. Figure 5.9 shows the large difference uncorking the tubes made on the lifetimes of the films. All films

in the uncorked tubes burst within two days, while the average film lifetime in a corked tube was over 16 days, with some films lasting 60 days. This rapid film death may explain the discrepancy between the fitted Weibull distribution and the first few days of experimental data. Improperly sealed tubes would experience a greater exposure to the environment, leading to much shorter film lifetimes than would otherwise be expected.

Similar variations in lifetimes were achieved in a small-scale study of bubble lifetimes undertaken by Rämme [85] by increasing the viscosity of the surfactant solution used in his experiment. While our experiment did not vary the chemical composition of the foam, increasing viscosity would hinder the drainage of liquid from the films (as commented on in Part I), suggesting that loss of liquid is a primary cause of film instability, present in our control in increased evaporation losses.

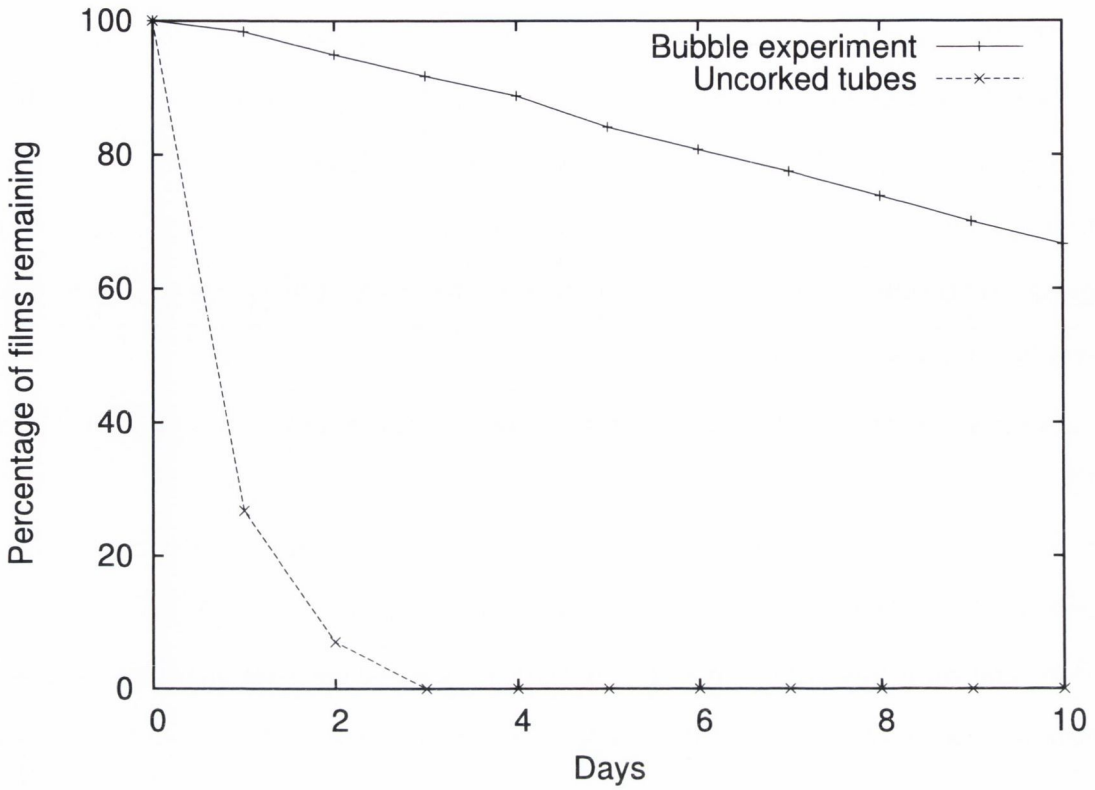

Figure 5.9: By plotting the percentage of surviving films as a function of time for both the corked tubes from the main Science Gallery experiment and the uncorked tubes from our additional experiments, we can see the dramatic decrease in lifetime arising from exposure to the atmosphere. All other aspects of the experiment were kept the same, with the uncorked tubes filled with identical solution and using the same apparatus.

5.5 Possible mechanisms of rupture

A film thins through drainage and evaporation [78] until it reaches a minimum thickness. The dependence of potential energy on film thickness may contain two minima, corresponding to the common black film and Newton black film (with film thickness $\approx 20\,\text{nm}$ or $\approx 5\,\text{nm}$, respectively). A thin film in such a state is stabilised by the balance between the van der Waals attraction and various repulsive forces (for example electrostatic interactions [96]). Furthermore, the film is stabilised

against external perturbations by the Marangoni effect (a local increase in film area leads to a temporary increase in surface tension, which, in turn, creates a restoring force which brings the film back to equilibrium). Black films are fragile and easily rupture due to environmental effects such as airborne contaminants and air flow. In our experiment, these effects were reduced by sealing the films in sample tubes. However, even in these protected conditions, the film lifetime is finite. What causes the films to rupture?

An often-invoked model is rupture induced by thermally excited capillary waves [78, 97] on both surfaces of the film. These waves can move the interfaces temporarily closer together, and the increased van der Waals attraction then leads to rupture (overcoming the repulsive forces). This mechanism is illustrated in Figure 5.10. Recent work on the related area of bubble coalescence points to the importance of hydrodynamic interactions [98]. It is not clear how the models for film rupture can give rise to the Weibull distribution, which we found to have a width of approximately 20 days compared to a mean film lifetime of over 16 days.

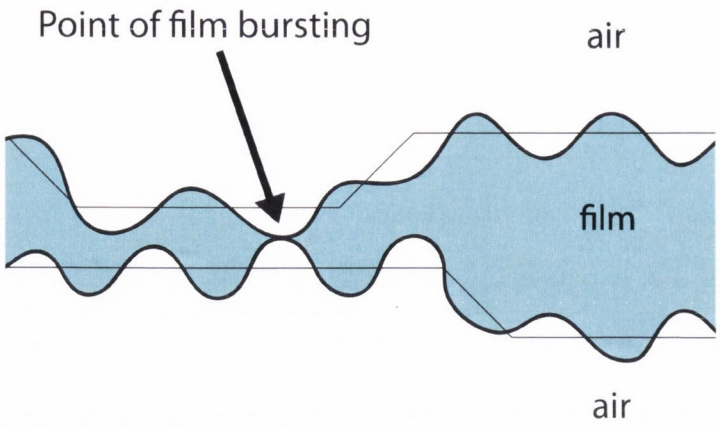

Figure 5.10: While no theories of film ageing, film instability, or film death are universally accepted, several models exist in the literature [78]. The primary mode of film rupture is believed to be the growth of surface waves (also known as capillary waves or corrugations). As the film thins, destabilizing forces overcome stabilizing forces and surface waves begin to grow. The fastest growing wave will burst the film at the thinnest point (as the films are not homogeneous).

5.6 Conclusions and outlook

While soap film stability has been measured in the past (for example, by Rämme [85]), previous studies used small sample sizes with a limited number of films. Our experiment collected data for over 2,500 films, allowing for the first time thorough statistical analysis of film lifetimes.

We were able to identify the most likely candidate probability distribution for soap film lifetimes, with statistical analysis showing that the data is well described by the Weibull distribution. The final fits of the Weibull distribution to our data give a shape parameter $k > 1$, indicating that there is a process by which the films age and become more likely to burst as time goes on (and that the expected failure rate will increase over time). This is consistent with experimental observa-

tions of the soap films and is likely due to some combination of evaporation and drainage of liquid out of the films. Our results also show that soap films can be surprisingly stable given the correct circumstances, with a 16-day average lifetime and with some films surviving for nearly two months. We also note that our shape parameter k is approximately 3/2, hinting to a square-root dependence on time for the film bursting process (or more precisely, a square-root dependence damped by a decaying exponential function). Keeping in mind the caveat noted previously (arising from the difference in structure between our samples and more complex foams) this dependency could be the basis for a model of the ageing and death of foams.

We also carried out a second experiment, in which films were exposed to the environment. We cannot overstate the effect of such atmospheric exposure, with every film in the second group destroyed within two days (an approximately 30-fold reduction in lifetimes). This may suggest that in (for example) industrial processes such as foam fractionation, foam coarsening and rupture effects may vary widely between surface bubbles and those inside the foam (with the outer layer effectively shielding those inside). Li et al. [99] (see also [100]) have presented research on the effects of humidity on the process of foam fractionation (see Chapter 3.1), noting that the stability of foams in fractionation columns shows a strong dependence on exposure to the environment and the resulting evaporation. Researchers in these fields may be able to use our experimental approach to quantify the difference between exposed and protected parts of their foams.

Repeating this experiment in more rigorous conditions, and with more information about individual films — such as individual film lifetimes and positions relative to the exterior of the bamboo foam — may allow for a more detailed anal-

ysis, to include potential effects of avalanches (i.e., where a film bursting triggers the bursting of neighbouring films) and leakage of samples (where those films closest to corks would likely burst preferentially). Using this experimental approach with more complex foams could allow further insight into any possible theoretical models for film decay and bursting. Finally, and on a personal note, the public nature of the exhibition was rewarding for the author and for members of the public. Much academic research exists in a rarefied world, removed completely from the general public. In this work, we were able to engage with visitors who had little to no experience with the scientific method and let them feel part of a real research effort. Even though the samples were created by members of the public, and kept in the non-ideal circumstances of a public exhibition, we were able to extract useful results due to the large amount of data collected, showing that this public-experiment approach still has scientific merit. Outside of the direct aims of the experiment, the research on film stability presented here has some important points of contact with other work presented in this thesis and with the general issue of foam deterioration and decay.

Chapter 6

Coda

In this Thesis, we have explored important subsets of the wide field of foams — the drainage of liquid through the complex network of Plateau borders integral to all foams, and the effects that the changes in liquid have on the longevity and stability of foams. These processes are of great practical importance in many areas.

Drainage

We have created a thorough analytical model for the industrial process of foam fractionation. Starting from a simple geometry (the inverted U-tube), we created a model based on elementary foam drainage theory (using a modified version of the Foam Drainage Equation).

Throughout our analysis, we aimed to keep the model as widely applicable as possible and to keep in mind industrial constraints. To this end, we analysed the effects of varying leg length on the operational efficiency of foam fractionation.

Comparisons to numerical simulations and experiments confirmed the validity of our fractionation model. Real-world columns often include multiple liquid inflows to improve efficiency and performance [45], and we have carried out preliminary work on integrating multiple flows into our model.

Our model may therefore have application in the design and operational efficiencies of both experimental and industrial uses of fractionation. As it is based on elementary drainage theory — the Foam Drainage Equation — it provides a solid foundation from which to extend theory, and makes a large body of existing drainage research available to the fractionation field.

Future work on our model should largely focus on increasing this applicability to real-world columns. Including chemical effects such as adsorption time may allow simple limits to be placed on column size (a length below which the efficiency of the column is reduced, as not all surface active molecules are carried through the foam, but instead drain out of the foam). Applying the full, time-dependent form of the FDE could allow us to study how the fractionation column approaches the steady-state, and predict how the efficiency of the column is affected by such behaviour. Other aspects of fractionation — such as solution concentration — also have a time-dependent aspect, which could be better understood by application of the full FDE.

We also presented analysis of drainage in metal foams — promising advanced materials with strong potential in areas such as prosthetics and vehicle design [74]. While current methods for analysing such foams rely on destructive *ex-situ* tests (which make it difficult to understand the dynamic nature of these systems), we have developed a method which allows analysis of draining metal foams in the liquid state. By fitting numerical solutions of the full FDE to liquid fraction

profiles calculated from X-ray radioscopy, we were able to extract values for the surface tension and viscosity of the molten foam *in-situ*, without destroying or otherwise interfering with the foam.

We applied our method to drainage profiles for freely-draining foams generated from several different metal alloys (the profiles were captured on parabolic flights). We observed dramatic increases in viscosity for all examined alloys when comparing foams to bulk molten metal, likely due to changes in the foam structure due to the presence of oxide layers or stabilising particles on the surfaces.

Going forward, there are several potential directions in which to take our research, and some enhancements to the method could be made. Our analysis method is completely general in its approach (requiring only time-dependent liquid fraction profiles), and could, therefore, be applied to other systems of interest such as polymeric foams [75, 76]. Improvements to the X-ray detectors used could allow better time and space resolution, leading to more data available for our fitting routines (and, hence, more accurate values for the viscosity and surface tension). While we have used the FDE in an elementary form, modifications to the basic equation have been proposed which take into account more changes to the foam (such as a changing number of bubbles). Including such modifications may allow corrections to the data, again improving the fit quality. Finally, and perhaps most challenging, 3D tomographic scans of a draining foam could greatly enhance our knowledge of the foam structure, including direct measurement of bubble volumes over time.

Stability

The deterioration of foams over time (or, indeed, the lack of deterioration) is a major concern in many industrial processes utilising foams. However, this is a complicated phenomenon, depending on both the make-up of the foam and its surroundings — including atmospheric effects such as humidity, temperature and airborne particles.

We conducted a public experiment on soap film lifetimes, consisting of over 2,500 films which were sealed in tubes to minimise atmospheric effects. This large sample size allowed for the first thorough statistical analysis of the ageing and lifetimes of films (previous work used much smaller sample sizes). Our analysis showed that the data is well described by the Weibull distribution, and that soap films can be surprisingly stable given the correct circumstances (a 16-day average lifetime with some films surviving for nearly two months).

A second laboratory experiment explored the effect of atmospheric exposure by creating identical samples but not sealing them. This lead to the bursting of every film within two days — an approximately 30-fold reduction in lifetimes. This suggests that, in processes such as foam fractionation, foam coarsening and rupture effects may vary widely between surface bubbles and those inside the foam. The dependence on exposure to the environment of the stability of foams in fractionation columns has been noted [99].

Repeating this experiment in more rigorous conditions, and with more information about individual films — such as individual film lifetimes and positions relative to the exterior of the bamboo foam — may allow for a more detailed analysis of these effects.

The Stability of a Draining Foam

In the introduction to this Thesis we commented on the complex interplay of forces that drive the evolution of a foam. We have discussed two of these forces — the drainage of liquid through the Plateau border network, and the ageing and rupture of the films that make up the foam. In many real-world foams these two forces feed into each other, with drainage changing the local liquid content of the foam (and, hence, changing the likelihood of film rupture), and with film and bubble ruptures changing the structure of the draining foam.

The stability of foams is of paramount importance in many applications. Hutzler et al. [29] have further noted the importance of modeling foam and film stability when attempting to analytically describe the Bikerman foam test [1]. The work of Li and Stevenson [99] has pointed to a strong effect of humidity on the overall performance of fractionation columns — casting into doubt, perhaps, comparisons between experiments conducted in laboratories with large humidity differences.

Our current drainage theories do not take into account the stability and rupture of bubbles in the foam. This can easily lead to unphysical results, such as a foam with liquid fractions far below what could realistically be sustained in experimental systems. Approximations can be made in numerical simulations (by simply removing those parts of the foam that fall below threshold liquid fractions), but incorporating film stability into analytical models of drainage would be a great improvement.

[1] This test uses a similar set-up to our fractionation models, in which a gas is sparged into a tube at some gas velocity V. Rather than overflowing however, the foam decays in the tube, reaching a metastable state (in which the rate of foam bursting is balanced by foam creation) at some height. This height will be different for different foams and, as such, allows comparisons to be made between them.

Our experiments on film stability (while quite simple in design) have two major contributions to this problem. Firstly, while the experiments presented in this Thesis only examined the simplest case — a binary choice between a completely sealed foam and a completely exposed foam — it is immediately apparent how major an effect atmospheric exposure has on film lifetimes (see Figure 5.9). Further experiments could be designed to probe the intermediate regions, with a focus on humidity control most immediately applicable to current research efforts in fractionation. Our experimental set-up allows for easy control of other processes that may affect stability, such as initial liquid fraction and polydispersity. Secondly, and from a more theoretical perspective, the Weibull distribution found for the ageing and death of our soap films could be of use in extending drainage theory. We may be able to add a term to the average bubble volume $V_b(x,t)$ to take into account the changing number of bubbles over time based on this distribution. Employing a more probabilistic approach to film death would seem to be an improvement over simple threshold values. However, as noted in Section 5.2, there are key differences between the structure of our experimental bamboo foams and more common foams. Further experiments will be necessary to determine if and how this lifetime distribution varies with the underlying foam structure.

Closing Remarks

Throughout this thesis we have attempted to ground our models and theories with comparisons and applications to real-world systems.

Keeping experimental and industrial applications in mind focused and directed our research on fractionation, helping to guide theoretical work towards a general

model of the process, including considerations of efficiency and operational constraints. And, despite the humble beginnings of our research into film lifetimes, we found common ground with fractionation researchers, who are working on the demanding issues of environmental influences on industrial-scale processes.

Our research on the properties of metal foams closely linked elementary drainage theory to cutting-edge experimental techniques, and allowed, for the first time, direct analysis of the liquid melt properties *in-situ*. Again, the use of the well-tested foam drainage theoretical model allowed us to understand more fully the stabilising processes in experimental foams.

The results we have presented show the significant utility of drainage theory for examining experimental systems and the potential it has for modelling real-world processes. This approach is integral to the Trinity method — linking analytical, numerical and experimental results — and provides a solid foundation to build future work on. We hope, as well, that the public nature of the experiments presented in Chapter 5, and the success of that research, may inspire other researchers to include outreach in their work when possible.

Part III

Appendices

Appendix A

Full derivation of the Foam Drainage Equation

The Foam Drainage Equation describes the drainage of liquid through an isotropic network of Plateau borders in 3D (shown in schematic form in Figure 2.1). It is a non-linear partial differential equation for the foam density as a function of time and vertical position. It was originally presented in this form by Verbist and Weaire [101]. While analytical solutions have been found for specific sets of boundary conditions (as discussed in Chapter 2), in the general case it must be solved numerically.

To start the derivation, consider a single vertical Plateau border (PB) with cross-section $A(x,t)$, where x is the vertical (downwards) coordinate and t is time.

The radius of curvature of the PB sides depends on the pressure difference between the liquid and gas phases, as given by the Laplace-Young law

$$\Delta p = \frac{\gamma}{R}, \tag{A.1}$$

where γ is the surface tension and R is the radius of curvature.

Assuming that all bubbles are at equal pressure (taken as the average over all bubbles in the system if the bubbles are not exactly equal), then the PB is symmetrical and we can relate its cross-sectional area to the radius of curvature:

$$A = \left(\sqrt{3} - \frac{\pi}{2}\right) R^2 = C^2 R^2. \tag{A.2}$$

The cross-section of a PB (including the radius of curvature) can be seen in Figure A.1.

We next consider the volume element of the PB — $A(x,t)\ dx$. The forces acting on a volume element are (per unit volume):

- gravity: ρg
- dissipation: $-\eta^* \frac{u}{A(x,t)}$, where $\eta^* = f\eta_l$
- capillarity: $(\partial/\partial x)\Delta p$, where $\Delta p = \gamma/R$,

where η^* is given by the bulk liquid viscosity n_l multiplied by a geometric factor f arising from the shape of the channel. For a simple cylinder, this factor is $8\pi \approx 25$, while, for a PB, it needs to be found numerically and is approximately 50. Inertial effects are neglected and Poiseuille dissipation is assumed (i.e., laminar viscous flow, incompressible liquid), and we disregard additional dissipation within the

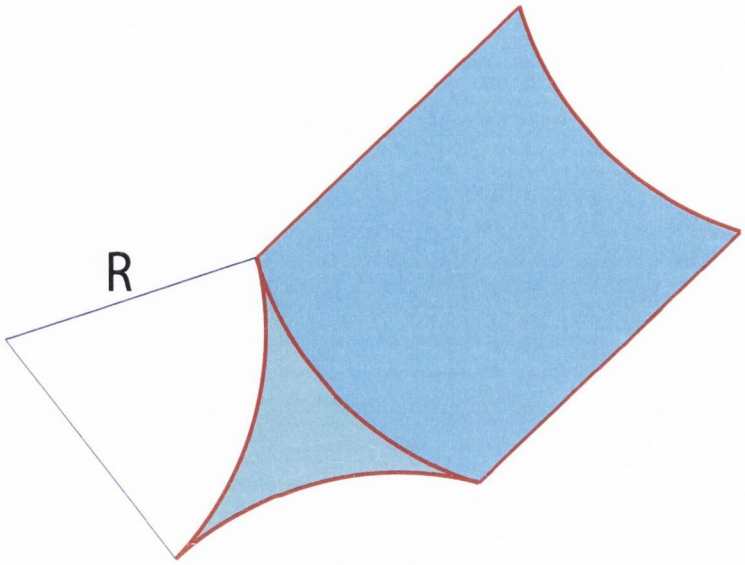

Figure A.1: A Plateau border in schematic form (reproduced here for clarity), showing the cross-sectional shape of the border. The curved shape of the Plateau border results from the Young-Laplace equation.

junctions (i.e., this is channel-dominated drainage). The dissipation is proportional to the mean liquid velocity $u(x,t)$ and inversely proportional to the cross-sectional area A.

Taking the force balance for these quantities gives

$$u = \frac{1}{\eta^*}\left(\rho g A - \frac{C\gamma}{2}A^{-1/2}\frac{\partial A}{\partial x}\right). \tag{A.3}$$

We can now introduce the equation of continuity:

$$\frac{\partial A}{\partial t} + \frac{\partial (Au)}{\partial x} = 0. \tag{A.4}$$

Substituting the expression obtained from considering the force balance for u, we arrive at the foam drainage equation:

$$\frac{\partial A}{\partial t} + \frac{1}{\eta^*}\frac{\partial}{\partial x}\left(\rho g A^2 - \frac{C\gamma}{2}\sqrt{A}\frac{\partial A}{\partial x}\right) = 0. \tag{A.5}$$

From this starting point, it is straightforward to generalise this equation to a fully isomorphic 3D foam by approximating the foam by a network of randomly-oriented PBs. We allow each PB to be some angle θ to the vertical. To facilitate this, we replace the vertical coordinate x with the coordinate in the direction of the PB $x_\theta = \frac{x}{\cos\theta}$, and replace gravity g with $g_\theta = g\cos\theta$. This leads to a variation of the previously derived dimensional form:

$$\frac{\partial A}{\partial t} + \frac{\cos^2\theta}{\eta^*}\frac{\partial}{\partial x}\left(\rho g A^2 - \frac{C\gamma}{2}\sqrt{A}\frac{\partial A}{\partial x}\right) = 0. \tag{A.6}$$

We must next take the *network average* of $\cos^2\theta$:

$$\langle\cos^2\theta\rangle = \frac{\int_0^\pi \cos^2\theta\sin\theta d\theta}{\int_0^\pi \sin\theta d\theta} = \frac{1}{3}. \tag{A.7}$$

This result means that the non-dimensional FDE for an isomorphic 3D network takes an identical form to that for a single vertical PB, with only a single change. We simply have to replace $\eta^* = 50\eta_l$ with $\eta^* = 3 \times 50\eta_l = 150\eta_l$, where η_l is the bulk liquid viscosity.

This network averaging also accounts for the junctions where the PBs meet, provided we make some approximations. We do not take any dissipation within the junctions into account (i.e., we assume perfectly channel-dominated drainage). Next, we approximate the junction as consisting of straight PBs which meet in a

symmetric tetrahedron (this is valid for foams with low liquid fractions). As $\cos\theta$ sums to zero over the four PBs that make up the junction (a simple geometric consideration), the conservation rule for the junction is obeyed.

Our next step is to rewrite the FDE in terms of liquid fraction ϕ rather than cross-sectional area A. To do this, we express ϕ in terms of A:

$$\phi_l(x,t) = l_V A(x,t), \tag{A.8}$$

where l_V is the total length of Plateau borders per unit volume of foam, $l_V \simeq 5.35 V_b^{-2/3}$. Here, V_b is the average volume of a bubble in the foam, and the constant 5.35 arises from geometric consideration of a Kelvin foam (see Figure 1.11). Similar values are found for a large variety of different bubble types [7] and varying liquid fractions (with differences of up to 2% from different structures, and no more than 10% from variations in liquid fraction). This volume can be estimated from the average Plateau border length (again treating the bubbles in the foam as Kelvin cells), as a Kelvin cell with edge length L has volume $V_b = 8\sqrt{\pi}L^3$.

This leads us to the full form of the FDE, expressed in terms of liquid fraction:

$$\frac{\partial\phi}{\partial t} + \frac{1}{\eta^*}\frac{\partial}{\partial x}\left(\frac{\rho g}{l_V}\phi^2 - \frac{C\gamma}{2}\sqrt{\frac{\phi}{l_V}}\frac{\partial\phi}{\partial x}\right) = 0. \tag{A.9}$$

As this equation is quite unwieldy, we will gather the assorted constants into two constants, c_1 and c_2, leading to a final FDE:

$$\frac{\partial\phi}{\partial t} + \frac{\partial}{\partial x}\left(c_1\phi^2 - c_2\phi^{\frac{1}{2}}\frac{\partial\phi}{\partial x}\right) = 0, \tag{A.10}$$

where c_1 and c_2 are given by

$$c_1 = \frac{\rho g}{l_V \eta^*}, \tag{A.11}$$

$$c_2 = \frac{1}{2}\frac{C\gamma}{l_V^{1/2}\eta^*}. \tag{A.12}$$

c_1 has dimensions of velocity and c_2/c_1 dimensions of length.

The effect of variable bubble volume

In the preceeding derivation of the FDE it was assumed that the bubble volume and, hence, l_V was constant. In those foam systems where this is not a valid assumption, l_V will be time- and space-dependent and $l_V(x,t) \simeq 5.35 V_b(x,t)^{-2/3}$ must be explicitly included in the continuity equation.

Equation A.4 therefore becomes

$$\frac{\partial(A l_V)}{\partial t} + \frac{\partial(A l_V u)}{\partial x} = 0 \tag{A.13}$$

or

$$\frac{\partial \phi}{\partial t} + \frac{\partial(\phi u)}{\partial x} = 0. \tag{A.14}$$

The rest of the derivation proceeds as before and we arrive at a variant of the FDE which includes the variation of $l_V(x,t)$,

$$\frac{\partial \phi}{\partial t} + \frac{1}{\eta^*}\frac{\partial}{\partial x}\left(\frac{\rho g}{l_V}\phi^2 - \frac{C\gamma}{2}\sqrt{\frac{\phi}{l_V}}\frac{\partial \phi}{\partial x} + \frac{C\gamma}{2}\left(\frac{\phi}{l_V}\right)^{3/2}\frac{\partial l_V}{\partial x}\right) = 0. \tag{A.15}$$

In the experimental systems we work with in this Thesis, bubble volume can be treated as constant (as described in the relevant experimental sections), and as such we may work with the simpler form of the FDE.

Appendix B

Analytic solutions for U-tube with infinite leg lengths

We may derive analytic solutions to the integrals that define the liquid fraction profiles for the left and right legs of the U-tube model used in Chapter 3 (as given in Section 3.2.2). The form of these integrals depends on whether the roots of the quadratic equations — Equation 3.9 (for the left leg) and Equation 3.10 (for the right) — are real or complex. We show here only solutions for the real roots; solutions for the complex case do exist (although they are very cumbersome) and may be found, for example, in the tables of Petit-Bois [102].

For the left-hand leg, we must consider two cases depending on whether the roots of Equation 3.9 — ϕ_1 and ϕ_2 — are distinct or coincident. For the case where ϕ_1 and ϕ_2 are real and distinct, we integrate Equation 3.12 to obtain

$$x = f_l(\phi_l) - f_l(\phi_c), \tag{B.1}$$

where $f_l(\phi)$ is given by

$$f_l(\phi) = -\frac{c_2/c_1}{(\phi_1 - \phi_2)}\left(\sqrt{\phi}_1 \ln\left|\frac{\sqrt{\phi} - \sqrt{\phi}_1}{\sqrt{\phi} + \sqrt{\phi}_1}\right| - \sqrt{\phi}_2 \ln\left|\frac{\sqrt{\phi} - \sqrt{\phi}_2}{\sqrt{\phi} + \sqrt{\phi}_2}\right|\right), \text{ for } \phi_1 \neq \phi_2. \tag{B.2}$$

In the case that ϕ_1 and ϕ_2 are real and coincident, we instead consider Equation 3.13:

$$f_l(\phi) = c_2/c_1\left(\frac{\sqrt{\phi}}{(\phi - \phi_1)} - \frac{1}{2\sqrt{\phi}_1} \ln\frac{\sqrt{\phi} - \sqrt{\phi}_1}{\sqrt{\phi} + \sqrt{\phi}_1}\right), \text{ for } \phi_1 = \phi_2. \tag{B.3}$$

In the limit $x \to \infty$, we obtain $\phi_l \to \phi_1$.

For the right-hand leg, we must only integrate Equation 3.11 (for real roots of Equation 3.10), arriving at

$$x = f_r(\phi_r) - f_r(\phi_c), \tag{B.4}$$

where $f_r(\phi)$ is given by

$$f_r(\phi) = \frac{-c_2/c_1}{\phi_3 - \phi_4}\left[\sqrt{\phi}_3 \ln\left(\left|\frac{\sqrt{\phi} - \sqrt{\phi}_3}{\sqrt{\phi} + \sqrt{\phi}_3}\right|\right) + 2\sqrt{-\phi_4}\left(\arctan\sqrt{\frac{\phi}{-\phi_4}}\right)\right]. \tag{B.5}$$

In the limit $x \to \infty$, we obtain $\phi_r \to \phi_3$.

Example solution profiles of Equation B.2 and B.5 are shown in Figure B.1.

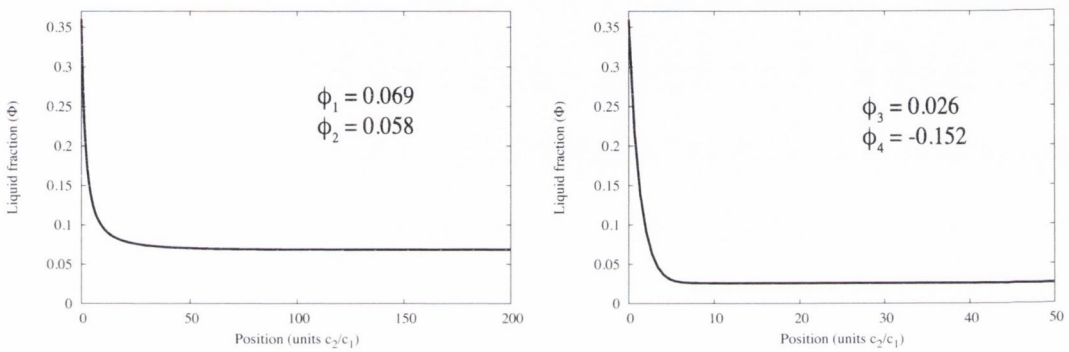

Figure B.1: Examples of solutions of Equation B.2 (left) and Equation B.5 (right) for real roots (values for the roots are shown). Note that the right leg tends to a constant value (ϕ_3) much more rapidly than the left leg (which tends to ϕ_1).

Appendix C

Finite size effects in the U-tube model

C.1 The effect of finite bend radius

The presented analytical theory for fractionation in a U-tube proceeded from assuming that the bend is short compared with the straight legs of the U-tube. The liquid fraction at the top of the two tubes was then equated and we showed that, in the limit of infinite leg length L, this value is $\phi_3 = \frac{(\sqrt{2}-1)}{2c_1}V$.

We now consider the effect of finite bend radius r in the same limit and obtain the derivative $\partial\phi_l/\partial x$ for the left leg:

$$\frac{\partial\phi_l}{\partial x} = -\frac{V^{3/2}}{4\sqrt{c_1}\,c_2\,c_L^{3/2}}. \tag{C.1}$$

For the right leg, we obtain:

$$\frac{\partial \phi_r}{\partial x} = 0. \tag{C.2}$$

Here, c_1 and c_2 are as defined in Section 2.2, and $c_L = \frac{(\sqrt{2}+1)}{2}$.

The change in liquid fraction across a finite bend of length πr may thus be estimated as

$$\phi_r - \phi_l = \Delta\phi_B \approx \frac{V^{3/2}}{4\sqrt{c_1}\, c_2\, c_L^{3/2}} \pi r, \tag{C.3}$$

which can be compared with the value $\phi_l = \phi_r = \left(\frac{\sqrt{2}-1}{2c_1}\right) V$ for $r = 0$ to predict the error in the liquid profile due to finite bend length:

$$\frac{\Delta\phi_B}{\phi_l(r=0)} = \frac{\pi}{\sqrt{c_L}} \frac{\sqrt{c_1}}{c_2} V^{1/2} r. \tag{C.4}$$

C.2 The effect of finite leg length

We start from an integral for L_l, following from Equation 3.4:

$$L_l = -\frac{c_2}{c_1} \int_{\phi_b}^{\phi_t} \frac{\sqrt{\phi_l} d\phi}{(\phi_l - \phi_1)(\phi_l - \phi_2)}, \tag{C.5}$$

where ϕ_t and ϕ_b are the top and bottom values for liquid fraction, respectively, and

$$\phi_{1,2} = \frac{V \pm \sqrt{V^2 - 4c_1 J}}{2c_1}. \tag{C.6}$$

We will evaluate this integral by making a drastic approximation, and then correcting it: we set the lower boundary value for ϕ_l to infinity and the upper bound to zero.

Substituting Equation 3.33 into Equation C.6 gives

$$\phi_{1,2} = \frac{V}{2c_1} \pm \frac{\epsilon}{\sqrt{c_1}} i. \tag{C.7}$$

Expressing these complex values of ϕ using Euler's notation gives

$$\phi_{1,2} = a e^{\pm ib}, \tag{C.8}$$

where a is the magnitude of the complex number and b is the argument (or phase). These quantities are given by

$$a = \frac{V}{2c_1} \sqrt{1 + \frac{4c_1\epsilon^2}{V^2}} \tag{C.9}$$

and

$$b = \arctan\left(\frac{2c_1^{1/2}\epsilon}{V}\right). \tag{C.10}$$

Substituting Equation C.8 into Equation C.5 results (after some straightforward manipulation) in

$$L_l = -\frac{c_2}{c_1} \int_0^\infty \frac{\sqrt{\phi_l}\, d\phi}{(\phi_l - \phi_\infty)^2 + \frac{\epsilon^2}{c_1}}, \tag{C.11}$$

where $\phi_\infty = \frac{V}{2c_1}$.

This integral may be evaluated using Mathematica, or it may be evaluated by contour integration. Integration using Mathematica yields

$$L_l = \pi \frac{c_2}{c_1} \left(2\sqrt{\phi_\infty^2 + \frac{\epsilon^2}{c_1}} - 2\phi_\infty \right)^{-\frac{1}{2}} \approx \frac{\pi}{\sqrt{2}} \frac{c_2}{c_1} \frac{\sqrt{V}}{\epsilon}. \tag{C.12}$$

Alternatively, we may evaluate the integral quite neatly by contour integration (the method of residues), using the contour illustrated in Figure C.1. The cut along the real axes is such that $\sqrt{\phi_l}$ has a positive real root on the upper side, and a negative real root on the lower side. The denominator of the integrand has two complex roots at

$$\phi_{1,2} = \phi_\infty \pm \frac{\epsilon i}{\sqrt{c_1}}. \tag{C.13}$$

The residues associated with each (taking into account the nature of square roots in a complex plane) are

$$R_1 = \frac{ic_2}{c_1 2\sqrt{2}\epsilon} \sqrt{\phi_\infty + \frac{\epsilon}{\sqrt{c_1}}} \tag{C.14}$$

$$R_2 = \frac{ic_2}{c_1 2\sqrt{2}\epsilon} \sqrt{\phi_\infty - \frac{\epsilon}{\sqrt{c_1}}}. \tag{C.15}$$

Our contour integral (from Cauchy's Residue Theorem, with the above caveats taken into account) is therefore (noting that such a contour results in twice the correct integral)

$$2 \oint_C \phi_l d\phi = 2\pi i \left(R_1 + R_2 \right). \tag{C.16}$$

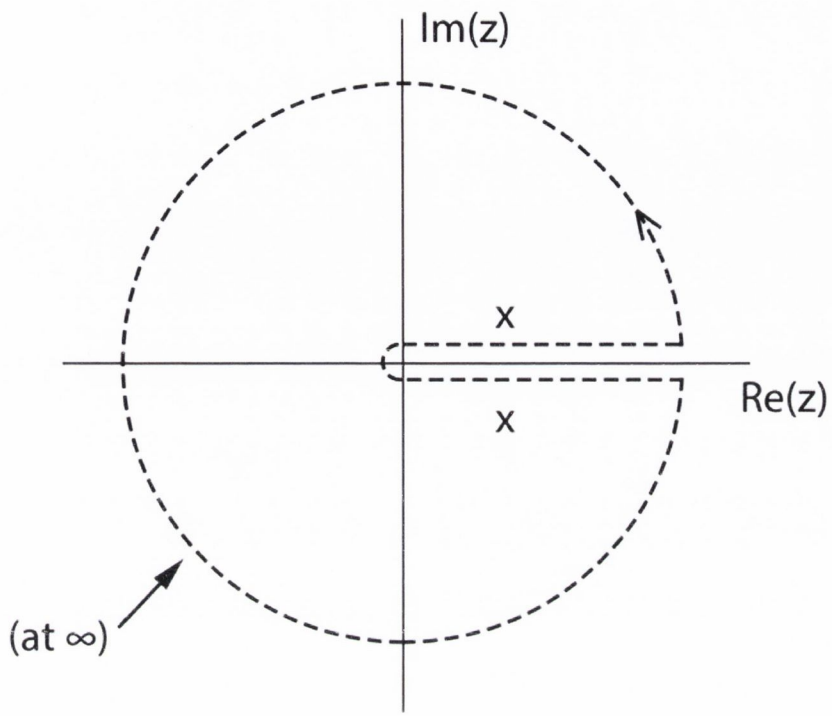

Figure C.1: Integration of Equation C.11 involves the contour indicated, with $z = \phi_l$. It includes a (zero) contribution from infinity and two equal contributions from above and below a cut on the real axis at ϕ_1 and ϕ_2 (Equation C.7).

Evaluating this expression leads to precisely the same result found by Mathematica (shown in Equation C.12). Gathering all the constants into a single μ_1, we obtain

$$L_l = \mu_1 V^{1/2} \epsilon^{-1}. \tag{C.17}$$

Note that, for some given V, the limit of infinite L_l corresponds to $\epsilon = 0$, in accord with the previous theory. We can now proceed to examine the lead-

ing approximation for the two end corrections that are required when the proper boundary conditions are reintroduced.

We correct Equation C.5 to take into account the bottom boundary condition — $\phi_L(0) = \phi_c$ — by adding

$$\Delta L_l^{(\text{bottom})} = \int_{\phi_c}^{\infty} \frac{c_2\sqrt{\phi_l}d\phi_l}{c_1(\phi_l - \phi_\infty)^2 + \epsilon^2} \tag{C.18}$$

to the integral of Equation C.5.

Neglecting terms of order ϵ^2, and assuming that $\phi_\infty \ll 1$ and $\phi_l > \phi_\infty$, we may approximate the correction as

$$\Delta L_l^{(\text{bottom})} = \frac{c_2}{c_1}\int_{\phi_c}^{\infty} \phi_l^{-3/2} d\phi_l \tag{C.19}$$

$$= -2\frac{c_2}{c_1}\phi_c^{-1/2}. \tag{C.20}$$

Finally, we add a further correction for the top boundary condition — $\phi_l = \phi_3$ — as follows (again neglecting terms of order ϵ^2):

$$\Delta L_l^{(\text{top})} = \frac{c_2}{c_1}\int_0^{\phi_3} \frac{\sqrt{\phi_l}}{(\phi_l - \phi_\infty)^2} d\phi_l. \tag{C.21}$$

In this case, $\phi_l > \phi_\infty$ in the range of integration, and hence

$$\Delta L_l^{(\text{top})} = -\frac{c_2}{c_1 \phi_\infty^2} \int_0^{\phi_3} \sqrt{\phi_l} d\phi_l \tag{C.22}$$

$$= -\frac{2}{3} \frac{c_2}{c_1} \frac{\phi_3^{3/2}}{\phi_\infty^2} \tag{C.23}$$

$$= -\frac{2\sqrt{2}}{3} \left(\sqrt{2} - 1\right)^{3/2} \frac{c_2}{{c_1}^{1/2}} \frac{1}{\sqrt{V}}. \tag{C.24}$$

Summarily, we have arrived at

$$L_l = \mu_1 V^{1/2} \epsilon^{-1} + \mu_2 + \mu_3 V^{-1/2}, \tag{C.25}$$

where

$$\mu_1 = \frac{\pi}{\sqrt{2}} \frac{c_2}{c_1}$$

$$\mu_2 = -\frac{2}{\sqrt{\phi_c}} \frac{c_2}{c_1}$$

$$\text{and } \mu_3 = -\frac{2\sqrt{2}}{3} \left(\sqrt{2} - 1\right)^{3/2} \frac{c_2}{{c_1}^{1/2}}.$$

This is a good approximation for the left-leg length, provided that the right-leg length $L_r \gg L_d$ — where L_d is given by Equation 3.31 (see Section 3.3.1) — and, hence, that the boundary condition used for the top correction is valid.

C.3 Generality of the limiting case

It is worth noting that the initial approximation (integrating from 0 to ∞) for L_l in the previous section results in an upper bound for L_l, given by $\hat{L} = \mu_1 V^{1/2} \epsilon^{-1}$. As the corrections for the top and bottom bounds of integration given by μ_2 and μ_3 are negative, $L_l < \hat{L}$. Therefore, if $L_l \to \infty$, $\hat{L} \to \infty$, irrespective of any boundary conditions chosen.

This implies that, for a wide range of boundary conditions, the steady state solution must have $J = J_0$ in the limit $L_l \to \infty$. Indeed, numerical simulations for the skimmer boundary conditions bear this out, recovering this relationship for sufficiently long columns. This limiting result was presented and derived for the specific boundary conditions of the U-tube, but appears to be far more general. Outside of the limiting case of infinite leg lengths, the boundary conditions are not equivalent and greater care must be taken. Numerical simulations have shown that the limiting case is approached relatively quickly (see, for example, Figure 3.2).

Top boundary correction for skimmer

In the case of a skimmer, the top boundary condition changes from $\phi_l(L) = \phi_3$ to $\phi_l(L) = \phi_t$:

$$\Delta L_l^{(\text{top})} = \frac{c_2}{c_1} \int_0^{\phi_3} \frac{\sqrt{\phi_l}}{(\phi_l - \phi_\infty)^2} d\phi_l, \tag{C.26}$$

where $\phi_\infty = \frac{V}{2c_1}$. As $\phi_l < \phi_\infty$ in the range of integration, we may calculate this correction:

$$\Delta L_l^{(\mathrm{top})} = -\frac{c_2}{c_1\phi_\infty^2}\int_0^{\phi_t}\sqrt{\phi_l}d\phi_l \tag{C.27}$$

$$= -\frac{2}{3}\frac{c_2}{c_1}\frac{\phi_t^{3/2}}{\phi_\infty^2} \tag{C.28}$$

$$= -\frac{8}{3}c_1c_2\left(\frac{V^2}{4c_1}\right)^{3/2} \tag{C.29}$$

$$= -\frac{1}{3}\frac{c_2}{c_1^{1/2}}V^3 \tag{C.30}$$

$$= -\mu_4 V^{-1/2}. \tag{C.31}$$

Appendix D

Overview of software used

D.1 The Surface Evolver

The Surface Evolver [103] is a program which, given a structure (defined by vertexes, edges, faces and bodies), will attempt to determine the minimum surface energy configuration. It is widely used in foam structure research [3, 104, 105].

Surface Evolver simulations consist of tessellations of the surfaces that make up the foam (as shown in Figure D.1). While tessellations of this type are almost always an approximation of the true surface (especially in foams), increasing the refinement of such tessellations (e.g., using more triangles to represent the surface) often improves the accuracy of the simulation.

The Surface Evolver uses gradient descent [51] to minimise the energy of the input structures. This technique moves points on the surface mesh in the direction negative to the gradient of the energy vector, i.e., in the direction of steepest descent. However, gradient descent is a first-order method and successive steps

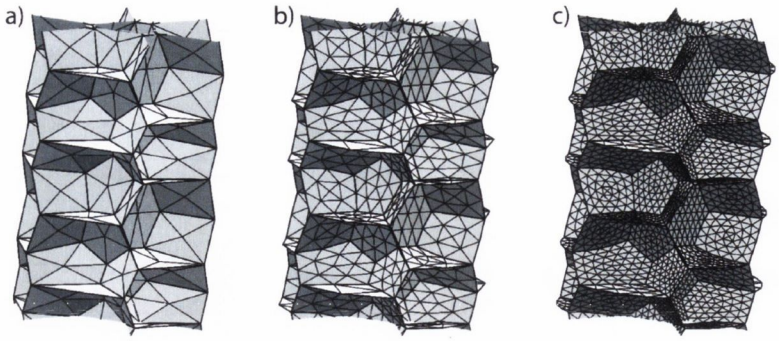

Figure D.1: Simulations of foams are usually carried out with K. Brakke's Surface Evolver [103]. This software approximates surfaces with a triangulated mesh or tessellation. This mesh can be refined (i.e., the number of triangles used can be increased) to improve the accuracy of the approximation. (a) to (c) show the same foam surfaces as the refinement of the tessellation is increased. Note how the curvature of the surfaces becomes smoother (and more representative of a real foam).

can be inefficient, as the solver 'zigzags' towards a (local) energy minimum. The Surface Evolver provides a higher-order (and much more efficient) method called conjugate gradient descent [51]. This method combines information from previous steps to find a more direct route to the energy minimum.

A robust minimisation technique therefore involves applying conjugate gradient descent to successive mesh refinements until the surface is deemed sufficiently close to equilibrium. At this point, the Hessian minimisation [106] may be used. The Hessian matrix is the square matrix of the second-order partial derivatives of the surface energy function, i.e., it describes the local curvature of surface energy. If the Hessian is positive-definite at some point x, then x is a local minimum of the function. The Surface Evolver's `hessian` command solves the Hessian matrix to jump directly to an energy minimum. Where the Hessian command can not be used successfully, extensive conjugate gradient minimisation must be carried out.

The internal representation of foams used by the Surface Evolver uses units of dimensionless area. Calculating surface energy requires scaling this area by some surface tension. We may simply choose this value such that surface energy is numerically equivalent to surface area.

D.2 Modelling wet foams using the Surface Evolver

In this section we will outline the techniques used to model wet foams using the Evolver. Starting from simulations of dry foams, Plateau borders were 'wrapped around' each edge and joined at vertices. This converted the idealised (perfectly dry) simulations into more realistic foams with a finite liquid fraction. We were able to generate foams with a desired liquid fraction by changing the size of these added borders.

Starting from such a wet foam, we increased the tessellation and minimised the foam as accurately as possible (within the limits of available computer resources). Provided the simulation remained internally consistent (i.e., the Evolver surfaces representing the foam are physically possible and do not contain singularities), we then recorded the surface energy of the foam.

Previous work on foam structure has often focused on confined ordered foams [3, 104, 107]. For such systems, the transition between different observed structures was approximated by the point at which the number of faces of the bubbles in the foam changed, most commonly by the area of a face going to zero. This process is shown graphically in Figure D.2.

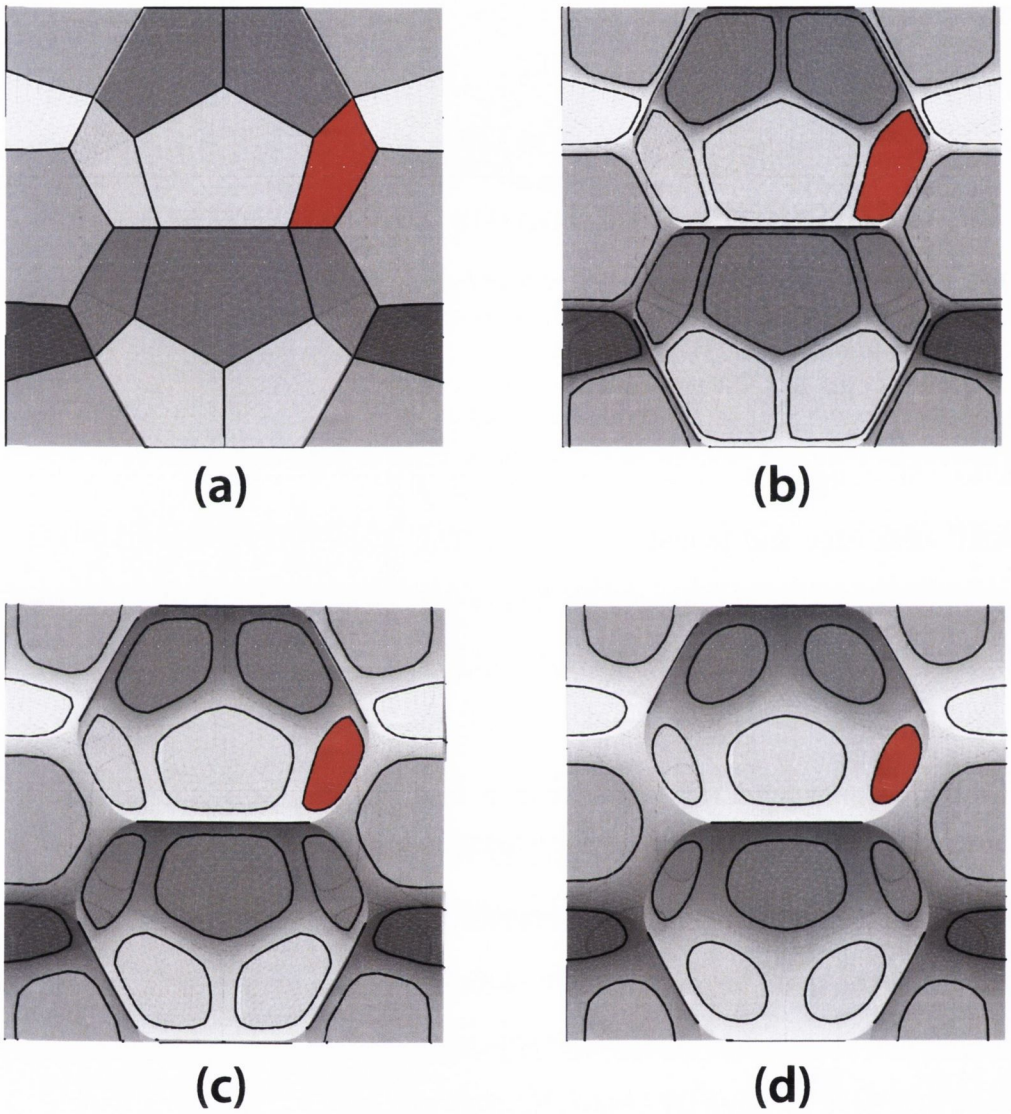

Figure D.2: Looking directly into the unit cell of the Weaire-Phelan foam as liquid fraction is increased (from 0% in (a) to 2.5% in (d)), it becomes apparent where bubbles will lose contact. Extrapolating the areas of the shrinking faces (one such face is marked in red) to zero gives us this limit.

While at first glance a similar approach may seem worthwhile, tracking face area has several disadvantages in our structures. It requires careful observation of the entire foam structure, including internal bubbles, to determine the face or faces that will reach zero area first. It may also be the case that several faces have to disappear before mechanical stability is lost — as discussed in Section 1.3.2, we need an average number of contacts per bubble of $n = 6$ for 3D foams to remain mechanically stable. As the area of faces tends towards zero, the Evolver surface is not guaranteed to remain in a physically correct configuration, reducing the accuracy of simulations. This means that, in many cases, we must extrapolate area measurements to zero, adding a further source of potential error.

For these reasons, we turn instead to the total surface energy of the foam as a function of liquid fraction. This method has the advantage of being independent of the local foam structure, instead taking the complete foam into account. By looking at the entire foam (or average energy per bubble in the foam), we do not need to carry out the painstaking examinations of every face in the structure, nor take into account different bubble types (e.g., in the Weaire-Phelan foam). We also remove the need for extrapolation or fitting of data, placing our results on much sounder ground.

By calculating the average energy of the bubbles in the foam E, we may define a stability threshold as

$$\frac{\partial E}{\partial \phi} = 0. \tag{D.1}$$

Below this threshold, increasing liquid fraction reduces the average energy of the bubbles in the foam, as reported by the Surface Evolver. Increasing ϕ past

this point increases the surface energy of the simulated foam. The real foam would resist such energy increases and would change structure (e.g., by losing contacts or by rearranging bubbles) to reduce energy again.

D.3 The MIGRAD minimiser

Throughout this work we have presented numerical solutions to various foam drainage models. Where fitting was required, we used the MIGRAD minimiser, part of the MINUIT program developed by F. James and M. Roos [50]. MINUIT is available as part of CERN's ROOT library[1].

MIGRAD uses the method of steepest descent to find minima. The gradient is evaluated by measuring function partial derivatives with respect to each parameter of the minimisation (the derivatives may be provided, or calculated numerically by the software). After the necessary gradients are calculated, the curvature at the working point can be used to estimate distance to the minimum. The step taken towards the minimum is set via inexact line search.

In standard Newton's method minimisation, computing this curvature requires inverting the Hessian matrix of second derivatives. MIGRAD uses variable metric methods in which the Hessian and its inverse may be estimated directly by analysis of gradient vectors. This can greatly reduce the computational cost of the minimisation. MIGRAD also includes checks for positive definiteness of the Hessian matrices. If the matrix is positive-definite at some point x, then that point is a local minimum of the function.

[1] See http://root.cern.ch/ for more information, including downloads.

The software is computationally efficient, allowing many fits to be carried out on standard, desktop-level computing resources.

Appendix E

Statistical analysis of lifetime data

Our analysis of statistical data was inspired by methods put forward by Clauset et al. [81]. While that work focused on correctly identifying power laws in experimental data, their methods are general in their approach and statistically rigorous.

- We estimated the parameters of our contender probability distributions using maximum likelihood estimation (described in Appendix E.1), based on best fits to the data.
- We then determined how likely it was that our data could have come from that best-fit distribution using the Kolmogorov-Smirnov (KS) test (described in greater detail in Appendix E.2).
- In the case that multiple candidate distributions passed the KS test, further statistical methods could be employed to pick the best model.

We applied this approach to lifetime data for soap films generated as part of a public exhibition, and determined that that data was best described by the Weibull

distribution (see Appendix E.3). This experiment, and the results, are presented in Chapter 5.

E.1 Maximum likelihood estimation

Maximum likelihood estimation is a method of estimating the parameters of a statistical model. Given some set of data and a statistical model, the method of maximum likelihood estimation (MLE) selects that set of values for the model parameters that maximises the likelihood function and, hence, the 'agreement' between the model and the data.

Consider a data set with ten points — x_1, x_2,... x_{10} — and two candidate probability distributions $p(x)$ and $q(x)$ for how the data set was generated (where all distributions are normalised to one).

The question is then: if the true distribution was $p(x)$, what would be the probability of obtaining these ten points? This probability is simply

$$\mathcal{L}_p = p(x_1) \times p(x_2) \times \ldots \times p(x_{10}), \tag{E.1}$$

and is called the likelihood $\mathcal{L}_p$ of those ten points given the model distribution $p(x)$. Next, we compare this result with that from another model distribution $q(x)$:

$$\mathcal{L}_q = q(x_1) \times q(x_2) \times \ldots \times q(x_{10}). \tag{E.2}$$

If it turns out that $\mathcal{L}_q < \mathcal{L}_p$, we can then say that $p(x)$ is the 'more likely' distribution. After all candidate distributions are checked, we simply choose the one that has the maximum likelihood.

In many cases, we will not have a discrete set of candidate model distributions, but rather a continuous range of distributions $p(x|a_1, a_2, \ldots, a_N)$ which are generated by varying the parameters $a_1, a_2, \ldots, a_N$. The process remains the same and we simply vary the parameters until we have maximised the likelihood.

Because $log(x) > log(y)$ implies that $x > y$, the distribution which maximises the likelihood $\mathcal{L}$ is the same as that which maximises the logarithm of the likelihood $log(\mathcal{L})$. Generally one considers the logarithm of the likelihood instead, as this turns what would have been an extremely large (or small) product into a smaller sum which is easier to handle analytically (since $log(ABC) = log(A) + log(B) + log(C) << ABC$).

In some cases, a closed-form solution for the parameters which maximise the log-likelihood may be found. This can be done, for example, by taking the derivative of $log(\mathcal{L})$ with respect to the parameter(s) and equating to zero.

It must be noted that the method of MLE cannot determine whether any particular model is correct, providing only the best fit of that model to the data. To solve this issue, other statistical tools — such as the Kolmogorov-Smirnov test — must be employed.

E.2 Two-sample Kolmogorov-Smirnov test

In our work, we use the two-sample Kolmogorov-Smirnov (KS) test. This is a non-parametric hypothesis test that evaluates the differences between the cumulative

distribution functions (CDFs) of two sample data sets, with a null hypothesis that the two data sets have the same underlying distribution [95].

We choose to use the two-sample test rather than comparing one data set to a statistical model directly, as the MATLAB numerical libraries used do not include every model of interest. We instead draw a large secondary data set from a distribution based on MLE best fits (as described in Appendix E.1).

The two-sample KS test cannot identify the underlying distribution of the samples but, as we generate one sample by drawing from a known distribution, this issue is not applicable.

The two-sample KS statistic is simply the maximum distance between the two CDFs,

$$D = \max_x |A(x) - B(x)|, \tag{E.3}$$

where A and B represent the CDFs of the experimental observations and the data drawn from the statistical model under consideration (with parameters set via MLE).

To ensure a proper test of the null hypothesis, we carried out the two-sample KS test with data sets containing 10^5 elements. As we had fewer experimental measurements than this, the data were bootstrapped by random sampling [51]. This process was repeated to rule out chance acceptance of some bootstrapped data.

E.3 The Weibull distribution

The Weibull distribution is commonly used to describe processes where the failure rate changes over time [108]. It originated in extreme value statistics where it is referred to as the type III extreme value distribution or third asymptotic distribution [109], and is named after Waloddi Weibull [110]. It is used to analyse systems that age, e.g., light bulbs breaking and engine component failures [94, 111]. The Weibull probability distribution function is given by

$$f(x;\lambda,k) = \begin{cases} \frac{k}{\lambda}\left(\frac{x}{\lambda}\right)^{k-1} e^{-(x/\lambda)^k} & (x \geq 0) \\ 0 & (x < 0) \end{cases} \tag{E.4}$$

with the cumulative distribution function

$$F(x;\lambda,k) = 1 - e^{-(x/\lambda)^k}, \tag{E.5}$$

where $k > 0$ is a dimensionless number known as the shape parameter and $\lambda > 0$ is the scale parameter of the distribution. x here is a 'time to failure', or lifetime. The value of k tells us the type of process we are dealing with: if $k < 1$, the failure rate decreases with time; if $k = 1$, the failure rate is constant (and the Weibull reduces to an exponential distribution); and if $k > 1$, the failure rate increases with time.

References

[1] D. Weaire, V. Langlois, M. Saadatfar, and S. Hutzler. Foam as granular matter. In T. Di Matteo, T. Aste, and A. Tordesillas, editors, *Granular and Complex Materials, World Scientific Lecture Notes in Complex Systems, volume 8*, pages 1–26, New Jersey, 2007. World Scientific Publishing.

[2] Y.J. Ng. Spacetime foam. *International Journal of Modern Physics D*, 11(10): 1585–1590, 2002.

[3] S.T. Tobin, J.D. Barry, A.J. Meagher, B. Bulfin, C. O'Rathaille, and S. Hutzler. Ordered polyhedral foams in tubes with circular, triangular, and square cross-section. *Colloids and Surfaces A: Physicochemical and Engineering Aspects*, 382 (13):24–31, 2011.

[4] A. Kraynik, D. Reinelt, and F. van Swol. Structure of random foam. *Physical Review Letters*, 93(20):208301–208301, 2004.

[5] D. Weaire and S. Hutzler. *The Physics of Foams*. Oxford University Press, Oxford, 1999.

[6] E.B. Matzke. The three-dimensional shape of bubbles in foam - an analysis of the role of surface forces in three-dimensional cell shape determination. *American Journal of Botany*, 33(1):58–80, 1946.

[7] A. Kraynik, D. Reinelt, and F. van Swol. Structure of random monodisperse foam. *Physical Review E*, 67(3):031403, 2003.

[8] J.A.F. Plateau. *Statique Expérimentale et Théorique des Liquides soumis aux seules Forces Moléculaires*. Gauthier-Villars, Paris, 1873.

[9] D.G.T. Barrett, S. Kelly, E.J. Daly, M.J. Dolan, W. Drenckhan, D. Weaire, and S. Hutzler. Taking Plateau into microgravity: The formation of an eightfold vertex in a system of soap films. *Microgravity-Science and Technology*, 20(1):17–22, 2008.

[10] J.E. Taylor. The structure of singularities in soap-bubble-like and soap-film-like minimal surfaces. *The Annals of Mathematics*, 103(3):489–539, 1976.

[11] M. van Hecke. Jamming of soft particles: geometry, mechanics, scaling and isostaticity. *Journal of Physics: Condensed Matter*, 22(3):033101, 2010.

[12] L. Bragg and J.F. Nye. A dynamical model of a crystal structure. *Proc. Royal Soc. London Series A*, 190:474–481, 1947.

[13] A. van der Net, W. Drenckhan, D. Weaire, and S. Hutzler. The crystal structure of bubbles in the wet foam limit. *Soft Matter*, 2(2):129–134, 2006.

[14] A.J. Meagher, M. Mukherjee, D. Weaire, S. Hutzler, J. Banhart, and F. Garcia-Moreno. Analysis of the internal structure of monodisperse liquid foams by x-ray tomography. *Soft Matter*, 7:9881–9885, 2011.

[15] A. Kraynik. The Structure of Random Foam. *Advanced Engineering Materials*, 8 (9):900–906, 2006.

[16] D. Weaire, editor. *The Kelvin problem*. Taylor and Francis, London, 1997.

[17] D. Weaire and R. Phelan. A Counter-example to Kelvin's Conjecture on Minimal-Surfaces. *Philosophical Magazine Letters*, 69(2):107–110, 1994.

[18] R. Gabbrielli, A.J. Meagher, D. Weaire, K.A. Brakke, and S. Hutzler. An experimental realization of the Weaire-Phelan structure in monodisperse liquid foam. *Philosophical Magazine Letters*, 92(1):1–6, 2012.

[19] R. Phelan, D. Weaire, and K.A. Brakke. Computation of equilibrium foam structures using the Surface Evolver. *Experimental Mathematics*, 4(3):181–192, 1995.

[20] J.J. Bikerman. Foams, theory and industrial application. *Reinhold, New York*, 1953.

[21] R.A. Leonard and R. Lemlich. A study of interstitial liquid flow in foam. Part I. Theoretical model and application to foam fractionation. *AIChE Journal*, 11(1): 18–25, 1965.

[22] I.I. Gol'dfarb, K.B. Kann, and I.R. Shreiber. Liquid flow in foams. *Fluid Dynamics*, 23:244–9, 1988.

[23] G. Verbist, D. Weaire, and A. Kraynik. The foam drainage equation. *Journal of Physics: Condensed Matter*, 8:3715–3732, 1996.

[24] S Koehler and S Hilgenfeldt. Liquid flow through aqueous foams: the node-dominated foam drainage equation. *Physical Review Letters*, 82(21):4232, 1999.

[25] S.J. Cox, D. Weaire, S. Hutzler, J. Murphy, R. Phelan, and G. Verbist. Applications and generalisations of the foam drainage equation. *Proceedings of the Royal Society A: Mathematical, Physical, and Engineering Sciences*, 456:2441–2464, 2000.

[26] A. Saint-Jalmes and D. Langevin. Time evolution of aqueous foams: drainage and coarsening. *Journal of Physics: Condensed Matter*, 14(40):9397–9412, 2002.

[27] S. Hutzler, G. Verbist, D. Weaire, and J.A. van der Steen. Measurement of foam density profiles using AC capacitance. *Europhysics Letters*, 31:497–502, 1995.

[28] D. Weaire, S. Hutzler, G. Verbist, and E. Peters. A review of foam drainage. *Advances in Chemical Physics*, 102:315–374, 1997.

[29] S. Hutzler, D. Lösch, E. Carey, D. Weaire, M. Hloucha, and C. Stubenrauch. Evaluation of a steady-state test of foam stability. *Philosophical Magazine*, 91: 537–552, 2011.

[30] S Koehler, S Hilgenfeldt, and H Stone. A generalized view of foam drainage: experiment and theory. *Langmuir*, 2000.

[31] A.M. Kraynik. Foam drainage. (SAND-83-0844), 1983.

[32] E. Carey and C. Stubenrauch. Free drainage of aqueous foams stabilized by mixtures of a non-ionic (C_{12}DMPO) and an ionic (C_{12}TAB) surfactant. *Colloids and Surfaces A: Physicochemical and Engineering Aspects*, 419:7–14, 2013.

[33] S Hutzler, D Lösch, E Carey, D Weaire, M Hloucha, and C Stubenrauch. Evaluation of a steady-state test of foam stability. *Philosophical Magazine*, pages 1–17, 2010.

[34] P. Stevenson, editor. *Foam Engineering: Fundamentals and Applications*. John Wiley & Sons, Ltd, 2012.

[35] D. Linke, H. Zorn, B. Gerken, H. Parlar, and R.G. Berger. Laccase isolation by foam fractionationnew prospects of an old process. *Enzyme and Microbial Technology*, 40(2):273 – 277, 2007. ISSN 0141-0229.

[36] P. Sarkar, P. Bhattacharya, R.N. Mukherjea, and M. Mukherjea. Isolation and purification of protease from human placenta by foam fractionation. *Biotechnology and Bioengineering*, 29(8):934–940, 1987.

[37] Nakabayashi T, Y. Takakusagi, K. Iwabata, and K. Sakaguchi. Foam fractionation of protein: Correlation of protein adsorption onto bubbles with a pH-induced conformational transition. *Analytical Biochemistry*, 419(2):173 – 179, 2011.

[38] R. Lemlich. *Adsorptive bubble separation methods—foam fractionation and allied techniques*. Industrial & Engineering Chemistry, 1968.

[39] P.M. Ireland and G.J. Jameson. Liquid transport in a multi-layer froth. *Journal of Colloid and Interface Science*, 314(1):207–213, 2007.

[40] P. Stevenson. Dimensional analysis of foam drainage. *Chemical Engineering Science*, 61(14):4503–4510, 2006.

[41] P. Stevenson. The Wetness of a Rising Foam. *Industrial & Engineering Chemistry Research*, 45(2):803–807, 2006.

[42] P. Stevenson. Hydrodynamic theory of rising foam. *Minerals Engineering*, 20(3): 282–289, 2007.

[43] X. Li and P. Stevenson. Foam Fractionation. In P. Stevenson, editor, *Foam Engineering: Fundamentals and Applications*, pages 307–330. John Wiley & Sons, Ltd, 2012.

[44] S.J. Neethling, H.T. Lee, and J.J. Cilliers. The recovery of liquid from flowing foams. *Journal of Physics: Condensed Matter*, 15:1563–1576, 2003.

[45] P.J. Martin, H.M. Dutton, J.B. Winterburn, S. Baker, and A.B. Russell. Foam fractionation with reflux. *Chemical Engineering Science*, 65:3825–3835, 2010.

[46] F.S. Shih and R. Lemlich. A study of interstitial liquid flow in foam Part III. Test of Theory. *AIChE Journal*, 13:751–754, 1967.

[47] D. Desai and R. Kumar. Liquid overflow from vertical co-current foam columns. *Chemical Engineering Science*, 39(11):1559–1570, 1984.

[48] P. Stevenson, M.D. Mantle, A.B. Tayler, and A.J. Sederman. Quantitative NMRI studies of transient washwater addition to rising foam. *Chemical Engineering Science*, 64(5):1001–1008, 2009.

[49] M. Durand, G. Martinoty, and D. Langevin. Liquid flow through aqueous foams: From the Plateau border-dominated to the node-dominated regime. *Physical Review E*, 60(6):R6307–R6308, 1999.

[50] F. James and M. Roos. Minuit - a system for function minimization and analysis of the parameter errors and correlations. *Computer Physics Communications*, 10: 343–367, 1975.

[51] W.H. Press, S.A. Teukolsky, W.T. Vetterling, and B.P. Flannery. *Numerical Recipes 3rd Edition: The Art of Scientific Computing.* Cambridge University Press, New York, NY, USA, 2007.

[52] S.A. Koehler, S. Hilgenfeldt, E.R. Weeks, , and H.A. Stone. Drainage of single plateau borders: direct observation of rigid and mobile interfaces. *Physical Review E*, 66:040601, 2002.

[53] J. Banhart and D. Weaire. On the road again: metal foams find favor. *Physics Today*, 55(7):37–42, 2002.

[54] V. Gergely and T.W. Clyne. Drainage in standing liquid metal foams: modelling and experimental observations. *Acta Materialia*, 52:3047–3058, 2004.

[55] C. Körner and M. Arnold and R.F. Singer. Metal foam stabilization by oxide network particles. *Materials Science and Engineering A*, 396:28–40, 2005.

[56] A. Haibel and A. Rack and J. Banhart. Why are metal foams stable? *Applied Physics Letters*, 89:154102–1–3, 2006.

[57] G. Kaptay. Interfacial criteria for stabilization of liquid foams by solid particles. *Colloids and Surfaces A: Physicochemical and Engineering Aspects*, 230:67–80, 2004.

[58] T. Wübben and S. Odenbach. Stabilisation of liquid metallic foams by solid particles. *Colloids and Surfaces A: Physicochemical and Engineering Aspects*, 266: 207–213, 2005.

[59] O. Brunke and S. Odenbach. In-situ observation and numerical calculations of the evolution of metallic foams. *Journal of Physics: Condensed Matter*, 18:6493–6506, 2006.

[60] F. Garcia-Moreno, C. Jiménez, M. Mukherjee, P. Holm, J. Weise, and J. Banhart. Experiments on metallic foams under gravity and microgravity. *Colloids and Surfaces A: Physicochemical and Engineering Aspects*, 344:101–106, 2009.

[61] J. Weise, H. Stanzick, and J. Banhart. Semi-solid processing of complex-shaped foamable material. In J. Banhart and A. Mortensen, editors, *Cellular Metals: Manufacture,Properties,Applications*. MIT Press, Berlin, 2003.

[62] V. Gergely and B. Clyne. The FORMGRIP process: Foaming of reinforced metals by gas release in precursors. *Advanced Engineering Materials*, 2:175–178, 2000.

[63] F. Garcia-Moreno and M. Fromme and J. Banhart. X-ray radioscopy on metallic foams using a compact micor-focus source. *Advanced Engineering Materials*, 6: 416–420, 2004.

[64] F. Garcia-Moreno, E. Solorzano, and J. Banhart. Kinetics of coalescence in liquid aluminium foams. *Soft Matter*, 7:9216–9223, 2011.

[65] G. Bradley. *Simulations of foams and liquid surfaces.* PhD thesis, Trinity College Dublin, 2000.

[66] C.J. Smithells. *Smithells Metals Reference Book.* Elsevier Butterworth-Heinemann, 2004.

[67] J. Goicoechea, C. Garcia-Cordovilla, E. Louis, and A. Pamies. Surface tension of binary and ternary aluminium alloys of the systems Al-Si-Mg and Al-Zn-Mg. *Journal of Materials Science*, 27(19):5247–5252, 1992.

[68] M.J. Assael, K. Kakosimos, R.M. Banish, J. Brillo, I. Egry, R. Brooks, P.N. Quested, K.C. Mills, A. Nagashima, and Y. Sato. Reference data for the density and viscosity of liquid aluminum and liquid iron. *Journal of Physical and Chemical Reference Data*, 35(1):285–300, 2006.

[69] E. Gebhardt and K. Detering. Properties of metallic melts. xvi. the internal friction of eutectic aluminum alloys. *Zeitschrift Fur Metallkunde*, 50:379, 1959.

[70] O. Brunke, A. Hamann, S.J. Cox, and S. Odenbach. Experimental and numerical analysis of the drainage of aluminium foams. *Journal of Physics: Condensed Matter*, 17:6353–6362, 2005.

[71] W.R.D. Jones and W.L. Bartlett. The viscosity of aluminium and binary aluminium alloys. *Journal of the Institute of Metals*, 81:145, 1952.

[72] R. Brooks, A.T. Dinsdale, and P.N. Quested. The measurement of viscosity of alloys. *Measurement Science and Technology*, 2005.

[73] M.C. Flemings. Behavior of metal alloys in the semisolid state. *Metallurgical and Materials Transactions B*, 22:269–293, 1991.

[74] J. Banhart. Aluminium foams for lighter vehicles. *International Journal of Vehicle Design*, 37(2):114–125, 2005.

[75] E. Solórzano, J. Pinto, S. Pardo, F. Garcia-Moreno, and M.A. Rodriguez-Perez. Application of a microfocus x-ray imaging apparatus to the study of cellular polymers. *Polymer Testing*, 32:321–329, 2012.

[76] E. Solórzano, S. Pardo-Alonso, J.A. de Saja, and M.A. Rodríguez-Pérez. Study of aqueous foams evolution by means of x-ray radioscopy. *Colloids and Surfaces A: Physicochemical and Engineering Aspects (online)*, 2013. doi: http://dx.doi.org/10.1016/j.colsurfa.2013.01.052.

[77] Sir J. Dewar. Soap bubbles of long duration. *Journal of the Franklin Institute*, 188(6):713 – 749, 1919.

[78] J.E. Coons, P.J. Halley, S.A. McGlashan, and T. Tran-Cong. A review of drainage and spontaneous rupture in free standing thin films with tangentially immobile interfaces. *Advances in Colloid and Interface Science*, 105(1-3):3–62, 2003.

[79] G. D'Agostini. Teaching statistics in the physics curriculum: Unifying and clarifying role of subjective probability. *American Journal of Physics*, 67(12):1260–1268, 1999.

[80] R. Streater. *Lost Causes in and Beyond Physics*. Springer, Berlin, 2007.

[81] A. Clauset, C.R. Shalizi, and M.E.J. Newman. Power-law distributions in empirical data. *SIAM Review*, 51(4):661–703, 2009.

[82] J. Ioannidis. Why most published research findings are false. *PLoS Medicine*, 2 (8):696–701, 2005.

[83] T. Hey and A. Trefethen. The data deluge: An e-science perspective. In F. Berman, G. Fox, and T. Hey, editors, *Grid Computing: Making the Global Infrastructure a Reality*. John Wiley & Sons, Hoboken, 2003.

[84] B.Q. Wu and P.L. Leath. Similarity of growing cracks in breakdown of heterogeneous planar interfaces. *Physical Review B*, 62(14):9338–9348, 2000.

[85] G. Rämme. A method to determine the average lifetime of soap bubbles. *IPS Physics Update*, 7(1):3–8, 2001.

[86] V. Carrier, S. Hutzler, and D. Weaire. Drainage of foams with regularly spaced parallel soap films. *Colloids and Surfaces A: Physicochemical and Engineering Aspects*, 309:13–19, 2007.

[87] V. Carrier, S. Hutzler, and D. Weaire. Observations of a variety of drainage patterns in bamboo foams. *Europhysics Letters*, 83:54005, 2008.

[88] D. Weaire, S. Hutzler, and N. Pittet. Cylindrical packings of foam cells. *Forma*, 7 (3):259–263, 1992.

[89] N. Pittet, D. Weaire, and S. Hutzler. Cylindrical packings of foam cells. *Forma*, 10:65–73, 1995.

[90] N. Pittet, P. Boltenhagen, N. Rivier, and D. Weaire. Structural transitions in ordered, cylindrical foams. *Europhysics Letters*, 35(7):547–552, 1996.

[91] D. Tritton and C. Egdell. Chaotic bubbling. *Physics of Fluids A: Fluid Dynamics*, 5(2):503, 1993.

[92] F. Elias, S. Hutzler, and M.S. Ferreira. Visualization of sound waves using regularly spaced soap films. *European Journal of Physics*, 28:755, 2007.

[93] V Carrier, S Destouesse, and A Colin. Foam drainage: A film contribution? *Physical Review E*, 65:061404–061401, 2002.

[94] W. Nelson. *Applied Life Data Analysis*. John Wiley & Sons, New York, 1982.

[95] F. Massey Jr. The Kolmogorov-Smirnov test for goodness of fit. *Journal of the Americal Statistical Association*, 46(253):68–78, 1951.

[96] D.J. Durian and D.A. Weitz. Foams. *Kirk-Othmer Encyclopedia of Chemical Technology, 4th Edition*, 11:783–805, 1994.

[97] A. Sharma and E. Ruckenstein. Stability, critical thickness, and the time of rupture of thinning foam and emulsion films. *Langmuir*, 3:760–768, 1987.

[98] I. Vakarelski, R. Manica, and X. Tang. Dynamic interactions between microbubbles in water. *PNAS*, 107(25):11177–11182, 2010.

[99] X. Li, R. Shaw, and P. Stevenson. Effect of humidity on dynamic foam stability. *International Journal of Mineral Processing*, 94(1-2):14–19, 2010.

[100] X. Li, S.I. Karakashev, G.M. Evans, and P. Stevenson. Effect of environmental humidity on static foam stability. *Langmuir*, 28(9):4060–4068, 2012.

[101] G. Verbist and D. Weaire. A soluble model for foam drainage. *Europhysics Letters*, 26(8):631–634, 1994.

[102] G. Petit Bois. *Tables of indefinite integrals*. Dover Publications, 1961.

[103] K.A. Brakke. The Surface Evolver. *Experimental Mathematics*, 1(2):141–165, 1992.

[104] S. Hutzler, J.D. Barry, P. Grasland-Mongrain, D. Smyth, and D. Weaire. Ordered packings of bubbles in columns of square cross-section. *Colloids and Surfaces A: Physicochemical and Engineering Aspects*, 344:37–41, 2008.

[105] W. Drenckhan and D. Langevin. Monodisperse foams in one to three dimensions. *Current Opinion in Colloid and Interface Science*, 15(5):341–358, 2010.

[106] K.A. Brakke. The Surface Evolver and the stability of liquid surfaces. *Philosophical Transactions of the Royal Society A*, pages 2143–2157, 1996.

[107] M. Saadatfar, J.D. Barry, D. Weaire, and S. Hutzler. Ordered cylindrical foam structures with internal bubbles. *Philosophical Magazine Letters*, 88(9):661–668, 2008.

[108] D.N.P. Murthy, M. Xie, and R. Jiang. *Weibull Models*. Wiley Interscience, 2003.

[109] E. Gumbel. *Statistics of Extremes*. Dover, Chichester, 2004.

[110] W. Weibull. A Statistical Distribution Function of Wide Applicability. *Journal of Applied Mechanics*, 18(3):293–297, 1951.

[111] M. Ohring. *Reliability and Failure of Electronic Materials and Devices*. Academic Press, San Diego, 1998.